EFFECT OF POST-PROCESSING HEAT TREATMENT ON THE MECHANICAL PROPERTIES OF INCONEL 718 FABRICATED BY SELECTIVE LASER MELTING

A THESIS SUBMITTED TO
THE GRADUATE SCHOOL OF NATURAL AND APPLIED SCIENCES
OF
MIDDLE EAST TECHNICAL UNIVERSITY

BY

SEREN ÖZER

IN PARTIAL FULFILLMENT OF THE REQUIREMENTS
FOR
THE DEGREE OF MASTER OF SCIENCE
IN
METALLURGICAL AND MATERIALS ENGINEERING

JANUARY 2020

Approval of the thesis:

EFFECT OF POST-PROCESSING HEAT TREATMENT ON THE MECHANICAL PROPERTIES OF INCONEL 718 FABRICATED BY SELECTIVE LASER MELTING

submitted by **SEREN ÖZER** in partial fulfillment of the requirements for the degree of **Master of Science** i**n Metallurgical and Materials Engineering, Middle East Technical University** by,

Prof. Dr. Halil Kalıpçılar
Dean, Graduate School of **Natural and Applied Sciences** _____

Prof. Dr. C. Hakan Gür
Head of the Department, **Met. and Mat. Eng., METU** _____

Prof. Dr. Arcan Fehmi Dericioğlu
Supervisor, **Met. and Mat. Eng., METU** _____

Examining Committee Members:

Prof. Dr. Kadri Aydınol
Metallurgical and Materials Eng, METU _____

Prof. Dr. Arcan Fehmi Dericioğlu
Metallurgical and Materials Eng, METU _____

Prof. Dr. Caner Durucan
Metallurgical and Materials Eng, METU _____

Prof. Dr. Hüsnü Emrah Ünalan
Metallurgical and Materials Eng, METU _____

Assoc. Prof. Dr. Ziya Esen
Materials Science and Eng, Çankaya University _____

Date: 31.01.2020

I hereby declare that all information in this document has been obtained and presented in accordance with academic rules and ethical conduct. I also declare that, as required by these rules and conduct, I have fully cited and referenced all material and results that are not original to this work.

Name, Last name : Seren Özer

Signature :

ABSTRACT

EFFECT OF POST-PROCESSING HEAT TREATMENT ON THE MECHANICAL PROPERTIES OF INCONEL 718 FABRICATED BY SELECTIVE LASER MELTING

Özer, Seren
Master of Science, Metallurgical and Materials Engineering
Supervisor: Prof. Dr. Arcan Fehmi Dericioğlu

January 2020, 110 pages

In this study, effect of the building direction and post-processing heat treatments on the microstructure and high temperature mechanical properties of as-fabricated Inconel 718 alloys have been investigated. Inconel 718 samples were fabricated in two different building directions such that their longitudinal axes were either parallel (horizontally built) or perpendicular (vertically built) to the building plate. During the selective laser melting (SLM) process, some undesired features can appear in the microstructure of the as-fabricated parts due to high temperature gradient and rapid solidification resulting from the nature of this additive manufacturing method. Therefore, possible post-processing heat treatments, including solutionizing and aging, were studied to eliminate these aspects in the as-fabricated parts to enhance the high temperature mechanical properties of the Inconel 718 alloy to be able to satisfy the requirements of the demanding working conditions. For both as-fabricated and peak heat treated (PHT) samples, the texture of the horizontally built samples was commonly concentrated in (001) plane, which represents the maximum heat flow, and hence easy grain growth direction. Additionally, the columnar grains had a slight tendency to also align along the

(111) and (101) planes. Otherwise, the texture of the vertically built samples had an intense texture on (001) plane. After all heat treatment conditions, the average microhardness of the Inconel 718 alloy significantly increased, and the maximum microhardness of ~462 HV was achieved for PHT-8h condition (solutionizing at 1040 ºC for 2 h, subsequently aging at 700 ºC for 8 h followed by air cooling). A slight decrease in hardness was observed in aging heat treatments applied for more than 8 hours, since the formation of δ phase hindered the precipitation of the strengthening γ″ phase by consuming Nb element in the system. Among the applied heat treatment processes, PHT-8h condition, resulting in optimum hardness, was selected for the samples to be tensile tested. The tensile test results performed at room temperature revealed that post-processing heat treatment can significantly increase the yield strength (YS) and ultimate tensile strength (UTS) while reducing the elongation at failure for both horizontally and vertically built samples. Aging treatment promoted the formation of the finely distributed strengthening γ″ and/or γ′ precipitates in the matrix, which serve as a barrier to dislocation movement, and therefore improve the mechanical properties. However, both the YS and UTS of the age hardened Inconel 718 alloy decreased when the tensile test was performed at high temperatures mainly because of the dissolution of the strengthening γ″ precipitates and the formation of the δ phase in the matrix.

Keywords: Nickel-Based Superalloys, Inconel 718 Alloy, Additive Manufacturing, Selective Laser Melting, High Temperature Mechanical Properties

ÖZ

İKİNCİL ISIL İŞLEMLERİN SEÇMELİ LAZER ERİTME YÖNTEMİ İLE ÜRETİLEN INCONEL 718 ALAŞIMININ MEKANİK ÖZELLİKLERİ ÜZERİNDEKİ ETKİSİ

Özer, Seren
Yüksek Lisans, Metalurji ve Malzeme Mühendisliği
Tez Yöneticisi: Prof. Dr. Arcan Fehmi Dericioğlu

Ocak 2020, 110 sayfa

Bu tezde, seçici lazer eritme yönteminde üretim yönünün ve üretim sonrası uygulanan ikincil ısıl işlemlerin Inconel 718 alaşımın mikroyapı ve yüksek sıcaklık mekanik özellikleri üzerindeki etkisi incelenmiştir. Inconel 718 alaşımları üretim tablasına göre 0° ve 90° açılarda üretilmiştir. Üretim sırasında kullanılan yüksek enerjili lazer ve parçanın hızlı soğuması nedeniyle katılaşma esnasında gelişen yüksek ısıl gradyanlar, parçanın içerisinde bazı kusurlar oluşmaktadır. Bu nedenle, SLM ile üretilen parçaların içerisinde oluşan kusurları gidermek ve alaşımın özelliklerini çalışma koşullarının gereksinimlerini sağlayacak şekilde geliştirmek amacıyla üretim sonrası ısıl işlem uygulanması (çökeltiye alma ve yaşlandırma) gerekmektedir. Farklı sürelerde uygulanan ısıl işlemler sonucunda, alaşımın doku oluşumu üzerinde herhangi bir değişiklik olmadığı gözlemlenmiştir. Dikey olarak üretilen tüm numunelerin dokulaması maksimum ısı akışının ve büyümenin kolay gerçekleştiği (001) düzleminde yoğunlaşmıştır. Yatay olarak üretilen tüm numunelerin dokulaması çoğunlukla (001) düzleminde yoğunlaşmış ve buna ek olarak, (111) ve (101) düzlemlerinde bir eğilime sahip olduğu gözlenmiştir. Uygulanan tüm ısıl işlemler sonucunda, Inconel 718 alaşımlarının sertlik değerlerinin önemli ölçüde arttığı gözlemlenmiştir. Uygulanan ısıl işlemler

arasında, en yüksek sertlik değeri PHT-8h ısıl işleminden sonra elde edildiğinden, çekme testleri öncesinde tüm numunelere PHT-8h ısıl işlem uygulaması yapılmıştır. Isıl işlem süresinin artmasıyla alaşımın mikroyapısında oluşan δ fazı, matris içerisinde bulunan ve alaşımın güçlendirilmesinde önemli rol oynayan Nb elementini tükettiğinden alaşımın sertliğinin az miktarda düşmesine neden olmuştur. Oda sıcaklığında yapılan çekme testi sonuçları, uygulanan ısıl işlemin hem yatay olarak hem de dikey olarak üretilen numunelerde akma ve çekme dayancının önemli ölçüde arttırırken, sünekliğinin azalmasına neden olduğu gözlemlenmiştir. Yaşlandırma işlemi sırasında matriste çökelen γ″ ve/veya γ′ fazları, alaşımda dislokasyon hareketlerini engellediğinden dolayı alaşımın mekanik özelliklerinin geliştirilmesinde katkıda bulunmaktadır. Yüksek sıcaklıklarda yapılan çekme testi sonuçları, alaşımın mukavemetinin sıcaklık artışıyla beraber azaldığını göstermektedir. Bunun nedenin alaşımın matrisinde çökmüş γ″ fazının çözülmesinden ve δ fazının oluşmasından kaynaklandığı gözlemlenmiştir.

Anahtar Kelimeler: Nikel-Bazlı Süperalaşımlar, Inconel 718 Alaşımı, Eklemeli İmalat, Seçici Lazer Eritme, Yüksek Sıcaklık Mekanik Özellikleri

To my beloved family

ACKNOWLEDGMENTS

I would like to express my greatest thanks to my supervisor Prof. Dr. Arcan Dericioğlu for his guidance, support, constructive feedback, endless tolerances, and patience from the beginning to the end of this thesis. I am indebted to him for leading me to the field of research and shaping my academic vision and background with his endless academic experience.

I would additionally like to express sincere gratitude to Assoc. Prof. Dr. Ziya Esen and Dr. Elif Tarhan Bor for their kind attitude, support and guidance.

I would like to thank Material and Process Development Manager Rabia Günay for her support and assistance.

I wish to state my deepest appreciation to Ezgi Bütev Öcal for her never ending support and for everything what she has taught so far. I am also grateful to my laboratory mates and friends Güney Mert Bilgin, Simge Tülbez and Tuğçe Altuntop for their endless support and wise suggestions.

I specially thank to my lovely friends Merve Nur Doğu, Pelin Gündoğmuş and Emel Erdal who give me strength and endure me throughout the entire period of the study. I would like to specially thank to my friends Anıl Erdal, İbrahim Aydın, Elif Yeşilay, Berk Aytuna and Esra Karakaya for their endless support.

I am also grateful to my friends Umutcan Ertürk, M. Tarık Boyraz and Doğuhan Sarıtürk for their friendship.

I would like to specially thank to all the technical staff of the Metallurgical and Materials Engineering Department for their suggestions, help and comments during this study.

Finally, I owe gratefulness to every individual of my beloved family for their warm and endless support during this study as in the entire of my lifetime.

TABLE OF CONTENTS

LIST OF TABLES

TABLES

LIST OF FIGURES

FIGURES

CHAPTER 1

INTRODUCTION

Inconel 718 was developed by International Nickel Corporation to achieve better weldability characteristics and has been extensively used for various industrial applications including aerospace, automotive, nuclear energy systems and petrochemical industries over the five decades. Inconel 718 is one of the most preferred superalloys as high pressure compressor discs, blades, casing and other components due to good combinations of mechanical properties combined with oxidation and corrosion resistance, as well as excellent creep resistance at elevated temperatures up to 700 ºC.

In order to produce only one piece of Inconel 718 alloy component, several conventional manufacturing methods such as casting, machining, joining are generally utilized together. Furthermore, the machinability of the Inconel 718 alloy is difficult owing to its low material removal rate. In contrast to conventional manufacturing methods, additive manufacturing (AM) methods have received significant interest due to the manufacturing capabilities of highly complex functional components. The most important advantage of AM is that it enables the production of very complicated geometric shapes in a single production stage, thus eliminating the number of assembly processes. While conventional manufacturing methods require many steps to produce the entire component that reduces the product quality and component life-time due to the defects that occurred during the assembly processes. In addition, AM technology allows manufacturers to replace or revise the product in a cost-effective manner. Instead of changing the production equipment, it is enough to change the computer-aided design (CAD) model of the part to be produced. In contrast, modifying a design during production can result in

significant cost increases or time delays, as it often requires a change of equipment on the production line for conventional manufacturing methods.

AM technology is basically divided into two groups based on the feeding of starting materials, which are directed energy deposition (DED) and powder bed fusion (PBF). Among these methods, selective laser melting (SLM) method has been widely utilized to produce complex shaped Inconel 718 alloy components with near fully density (>99%) and dimensional accuracy. During the SLM process, the components are fabricated layer-by-layer directly with controlled melting of Inconel 718 alloy powders with a focused laser beam. Then, Inconel 718 alloy powders are uniformly spread on a building platform of a certain layer thickness and then, the powders are melted according to the cross-sectional geometry of the part. After the solidification of the melted powders, the platform is lowered, and these operations are repeated until the component is completed as designed. Optimization of process parameters (i.e. laser power, powder properties, scanning orientation, etc.) is necessary to achieve good mechanical and physical properties of fabricated components.

Although the SLM method provides several advantages over conventional manufacturing methods such as eliminating assembly processes, reducing lead-time, minimizing material consumption and lowering investment cost, some undesired features can appear in the microstructure. Problems encountered during SLM processing can be described as high residual stresses, creation of non-equilibrium phases, directional grain growth, segregation of refractory elements or formation of defects such as cracks, pores, etc. The residual stress can significantly affect the components' dimensional and geometry accuracy as well as mechanical properties. Additionally, the microstructures of as-processed Inconel 718 alloy have been shown to differ from that of wrought and casting material. Therefore, post-treatment heat treatments are required to prevent the occurrence of these defects in the manufactured parts to improve mechanical properties and meet the requirements of harsh operating conditions.

The microstructure of the Inconel 718 alloy comprises of the stable γ matrix with strengthening phases γ′ ($Ni_3(Al,Ti)$) and γ″ (Ni_3Nb) as well as other secondary phases. The main objective is to optimize precisely the characteristics of the phases formed in the alloy by adjusting the post-processing heat treatment parameters to obtain the best mechanical performance. The typical heat treatment procedure of the Inconel 718 alloy includes solutionizing followed by aging treatment. The solution process is carried out above the γ' solvus temperature to dissolve the second phases to achieve a homogeneous alloying element concentration in the solid solution. Aging is then carried out in the range of 425-870 ºC with various soaking times to allow the formation of finely dispersed strengthening precipitates of γ′ and γ″ phases.

This study focuses on the effect of building direction and post-treatment heat treatments on the mechanical properties of Inconel 718 alloy components produced by the SLM method. Firstly, Inconel 718 alloys were produced in two different building directions (i.e. 0° and 90° to the laser beam, defined as horizontally and vertically built, respectively). Gas atomized Inconel 718 powders with a size approximately 26 μm were used as starting materials for the process. Then, the optimization of the post-processing heat treatment was performed by changing the aging parameters while keeping the solution heat treatment parameters constant. In this scope, all horizontally and vertically built samples were solutionized at 1040 ºC for 2 h and then air cooled. The aging heat treatment was then carried out at 700 ºC for various holding times. In addition, a pair of the horizontally and vertically built samples were subjected to standard aging treatment process defined by the standard AMS 5664 for comparison. Furthermore, the building direction strongly influences the texture formation of the as-fabricated component and thus leads to anisotropic mechanical properties. Therefore, tensile tests were performed both at room temperature and elevated temperatures up to 900 ºC according to ASTM E21 standard to investigate the mechanical behavior of the alloy.

This thesis consists of five main chapters which give information about the topics covered in the current study. Chapter 2 is divided into three sections to give detailed information about the main components of the study. Firstly, the properties of the nickel-based superalloys and their strengthening mechanisms are explained. Then, the AM technology and post-processing heat treatment performed to the manufactured components are presented. Chapter 3 consists of the experimental procedure utilized for the manufacturing of the parts by SLM method, their post-processing heat treatment and high temperature mechanical testing. In addition, the characterization methods used in this study are described in this section. Chapter 4 covers the experimental results of the microstructural examination and mechanical behavior of the Inconel 718 alloy parts. Finally, Chapter 5 presents the critical conclusions obtained at the end of the study.

CHAPTER 2

LITERATURE REVIEW

2.1 Superalloys

Superalloys have been defined as alloys developed for use in gas turbine engine (GTEs) technology that requires high performance characteristics under prolonged exposure without deterioration at high temperatures. Additionally, they have been successfully employed in other engineering applications including, chemical and petroleum plants, nuclear reactors, power generation, space vehicles, etc. [1]. These materials based on Group VIII B elements with the addition of multiplicity of alloying elements [2,3]. They are usually composed of various combinations of Ni, Fe and Cr with lesser amounts of some elements such as Co, Mo, Ti, Al, Ta, Nb, W and Hf [4].

There are many material groups that can be utilized at elevated temperatures such as superalloys, refractory metals and ceramics. Although refractory metals possess good mechanical properties, their poor oxidation resistance limits their application at high temperatures. Similarly, the low fracture toughness of ceramic materials restricts their usage in mechanical applications. On the other hand, superalloys have been mostly preferred due to their great combination of high-temperature mechanical characteristics (i.e. fracture toughness, yield and ultimate tensile strength) and good resistance to environmental attack. In addition, compositional control of superalloys allows the development of a broad array of metallic alloys which can be optimized through manufacturing or heat treatment processing [5]. Additionally, the excellent creep behavior of the superalloys makes them attractive metallic materials for many high-temperature engineering applications [6-8].

2.1.1 History of Superalloys

Development of the superalloys from the 1940s to these days can be characterized by optimization of the microstructure and the manufacturing processes. Firstly, both vacuum induction melting (VIM) and investment casting were introduced in the 1950s to increase the alloy performance by controlling the chemical composition and removing of some volatile trace. They allowed much higher levels of aluminum and titanium to be added to the superalloys, leading to the formation of the strengthening phases [5]. Subsequently, the manufacturing of directional-solidified and single-crystal alloys enabled significant developments to be made in the 1960s. These techniques have been used specifically to produce certain engine components to minimize or eliminate the grain boundaries that aligned in the load direction. Nowadays, single crystal superalloys are used in increasing amounts in gas turbine engine parts, especially where fatigue and creep properties are important [9].

Indeed, the superalloys were subjected to both chemical and mechanical degradations under such extreme operating conditions and resulting in loss of mechanical properties. Some compositional modifications were applied to superalloys in order to alter their mechanical properties. However, these changes caused to decrease in the other characteristics of superalloys such as oxidation/corrosion resistance or thermal expansion properties. Therefore, high temperature protective coatings were also developed to protect the superalloys from environmental attacks in the 1960s. Protective coatings were obtained by enrichment of alloy surfaces with metallic elements (i.e. Al, Cr, Si etc.) to the formation of a dense metallic oxides layer at the coating surface at elevated temperatures [5,10,11]. Advances in manufacturing technology and the development of protective coatings promote an increase in engine performance by raising the maximum operating temperature from 800 to 1300 ºC (Figure 2.1) [12].

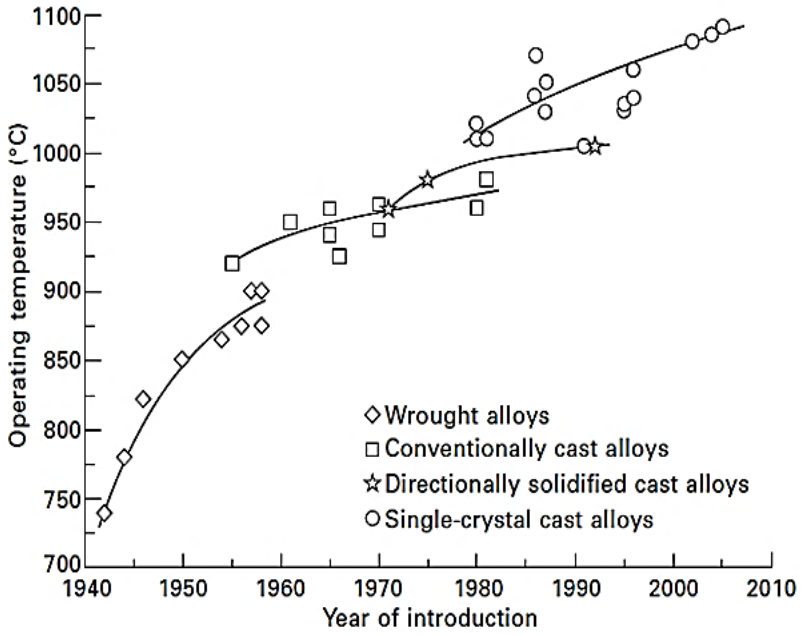

Figure 2.1. Development in the temperature limit of superalloys for aircraft turbine engines [12].

2.1.2 Classification of Superalloys

Superalloys are categorized according to the predominant alloying elements in the composition; nickel-, iron-nickel- and cobalt- based which are used at temperatures above 540 ºC. These superalloys are formed by combining a stable face-centered cubic (FCC) matrix with various secondary strengthening phases [5,7].

Iron-nickel based superalloys developed from austenitic stainless steels which undergoes a transformation from body-centered cubic (BCC) to FCC phase at 912 ºC. These alloys contain 15-60% iron with at least 25% nickel to stabilization of the matrix. Most of these alloys are primarily strengthened by precipitation hardening where intermetallic compounds are formed in the matrix. These types of alloys are less expensive compared with nickel-based and cobalt superalloys [5,13].

Cobalt-based superalloys are generally strengthened by a combination of solid-solution strengthening and carbide formation. Cobalt is hexagonally close-packed

(HCP) at room temperature but undergoes an allotropic transformation to the FCC phase at 417 ºC. The stabilization of the matrix phase is achieved by the addition of certain alloying elements. These alloys have better hot corrosion and sulfidation resistance than other types of superalloys owing to their high amount of chromium content (20-30%) and low diffusion of sulfur in the matrix [3,4].

Nickel-based superalloys achieve the highest temperature/strength combination of all groups of superalloys, making them remarkable materials for many high-temperature applications. Only these alloys have a stable austenitic FCC crystal structure at room temperature. The most outstanding characteristics of these alloys are their excellent stress rupture and creep resistance at elevated temperatures above 70% of their melting temperature (Tm = 1280 ºC). These alloys can be either strengthened by precipitation hardening or solid solution strengthening [5,14,15]. The comparison of mechanical properties and service conditions for superalloys are given in Figure 2.2 and Table 2.1, respectively.

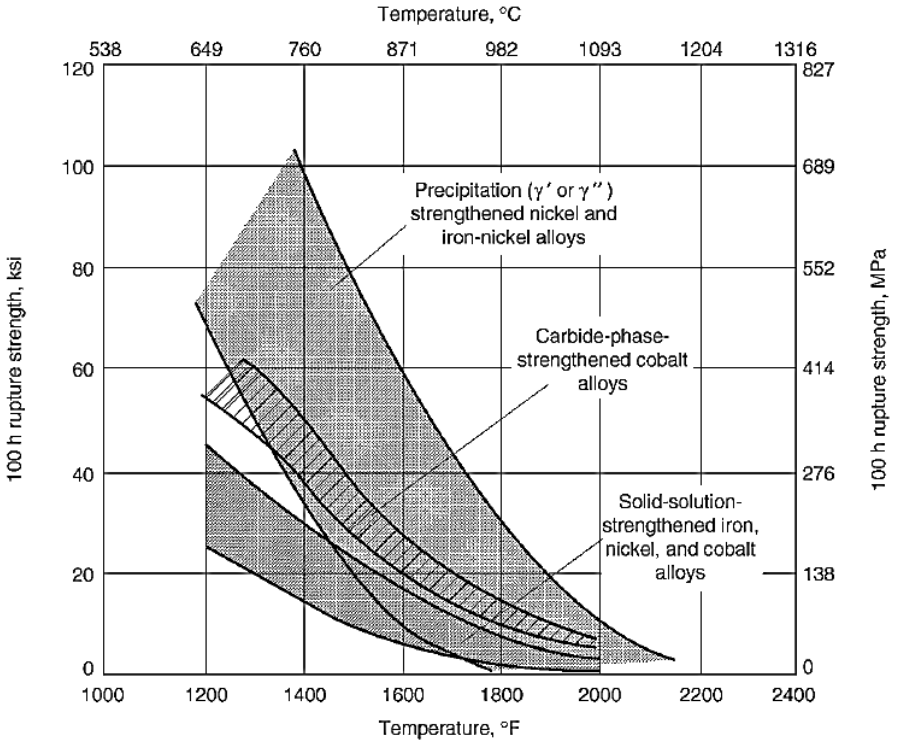

Figure 2.2. Stress-rupture strengths for strengthened superalloys as function of temperature [14].

Table 2.1. Some of the application areas and operating conditions of superalloys [4,16].

	Stress	**Temperature**	**Application Areas**
Cobalt-based superalloys	low	moderate - high	Vanes and other stationary components in GTEs
Iron-based superalloys	low	high	Blades, discs and casing in jet engines
Nickel-based superalloys	high	high	Turbine blades and discs in GTEs

2.2 Nickel-Based Superalloys

Nickel-based superalloys first designed in the 1940s as a simple nickel-chromium matrix alloys. They were then altered to a multi-phase system with the addition of alloying/refractory elements. It has been claimed that ferritic steels, aluminum and titanium alloys are generally used as components of GTEs. However, the low corrosion resistance and mechanical instability restrain their service temperatures below about 700 ºC [6]. It was found that the efficiency and performance of GTEs can be significantly improved by increasing the turbine entry temperature (TET) where the hot gases entering the turbine section (Figure 2.3). Therefore, new material types have been developed for extreme conditions, including high temperatures and corrosive environments [5,6,12].

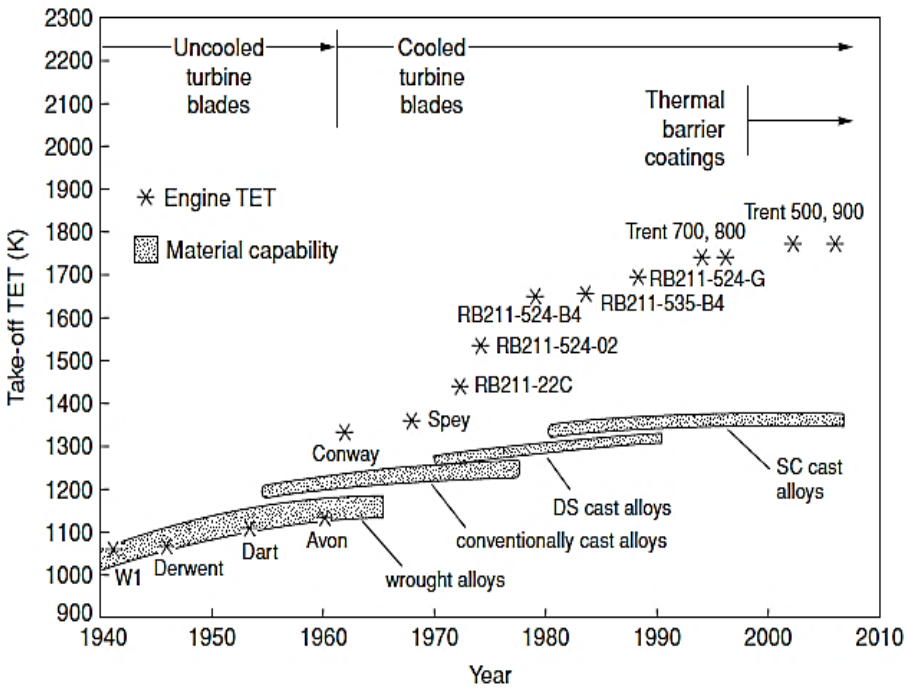

Figure 2.3. Evolution of production technology and turbine entry temperature (TET) capability of Rolls-Royce's civil aeroengines [6].

These alloys typically comprise 40-50% of the total weight of an aircraft engine, especially in the turbine and combustion sections of the engine. The use of nickel-based superalloys is also increasing in the aerospace, nuclear power systems, petrochemical and automotive industries. Due to their high creep and fatigue resistance combined with superior corrosion resistance, these alloys possess high performance under prolonged exposure to high temperatures, thus maintaining their stability throughout the service [14,17-21].

These alloys have a complex system with many alloying elements, including high amounts of chromium (10-20%), titanium and aluminum (combined up to 8%), cobalt (5-15%) and small quantities of molybdenum, tungsten and carbon elements. Other elements such as niobium, boron, tantalum and rhenium also play an important role in the strengthening mechanism [3].

The desired microstructural and mechanical characteristics of these alloys are highly dependent on alloying elements embedded in the matrix in terms of their composition, morphology, size and volume distribution [7]. These elements should be modified in a certain range as they play an important role in achieving optimum alloy properties. Table 2.3 summarizes the alloying elements that widely used in nickel-based superalloys and the subsequent effect on their properties.

Table 2.2. Role of alloying element effects on the nickel-based superalloys [7,14].

Effect	Element
Solid solution strengtheners	Cr, Fe, Mo, Co, W, Ta, Al, Ti, Re
High temperature strength	Ni, Nb, C, Co, Mo, W
Carbide formation	W, Ta, Ti, Mo, Nb, Hf
MC	W, Ta, Ti, Mo, Nb, Hf
$M_{23}C_6$	Cr, Mo, W
M_6C	Mo, W, Nb, Ta
γ′ precipitation	Al, Ti
γ″ precipitation	Nb
Raises solvus temperature of γ′	Co
Hardening precipitates and/or intermetallics	Al, Ti, Nb, Ta
Oxidation resistance	Al, Cr, Y, La, Ce
Improves hot corrosion resistance	La, Th
Sulfidation resistance	Cr, Co, Si
Increases rupture strength	B
Grain boundary refiners	B, C, Zr, Hf
Retards coarsening	Re

2.2.1 Phases in Nickel-Based Superalloys

The microstructure of these alloys typically consists of the gamma (γ) matrix phase along with other secondary phases. These secondary phases can be described as gamma prime (γ′) and gamma double prime (γ″) phases, intermetallic compounds, metal carbides or borides [7,14]. A brief description of each phase presented in nickel-based superalloys will be discussed in the following sections.

2.2.1.1 Gamma (γ) Matrix Phase

The FCC γ-matrix phase consists of mainly nickel and high concentration of solid solution elements like cobalt, chromium, molybdenum and iron. The matrix phase is suitable for high temperature structural alloys because of its high modulus and multiple slip systems, providing optimum mechanical properties (i.e. tensile, rupture, creep, thermo-mechanical fatigue). For example, some of them may be employed at > 0.85 Tm and for times up to 100000 h at relatively lower temperatures. In addition, the tendency to form a protective film of chromium oxide (Cr_2O_3) or aluminum oxide (Al_2O_3) on the substrate surface prevents the diffusion of oxygen or sulfur inward, which promotes resistance to oxidation [5,7].

2.2.1.2 Geometrically Close-Packed Phases

Geometrically close-packed (GCP) phases are intermetallic with the formula A_3B. They consist of the strengthening phases γ′ (FCC - Ni_3Al, Ni_3Ti) and γ″ (body centered tetragonal (BCT) - Ni_3Nb) and the closely related η (HCP - Ni_3Ti) and δ (orthorhombic - Ni_3Nb) phases. Mostly, the strengthening mechanism of the nickel-based superalloys is based on the formation of the γ′ phase. In some cases, the strengthening of the material is achieved by precipitation of the γ″ phase such as of Inconel 718 [5].

2.2.1.2.1 Gamma Prime (γ′) Phase

The γ′ phase is the most stable of the GCP phases with a nominal composition $Ni_3(Al,Ti)$ and possesses the FCC-$L1_2$ type structure which means the crystal lattice varies slightly (0-0.5%) from that of austenite FCC matrix [7,22]. The strengthening mechanism of most nickel- and nickel-iron- based superalloys is provided by the formation of the γ′ phase [23]. This phase usually forms as a coherent precipitate in the matrix just below the γ' solvus temperature (900 ºC)

[24]. The morphology of the phase (Figure 2.4) depends on the mismatch between the matrix and γ' precipitate which can be controlled by either heat treatment or compositional alterations. An increase in the mismatch and size of the precipitates lead to the transformation of spheroidal to cuboidal, then cuboidal to plate-like morphology [7]. In addition, the volume fraction and the size of the phase phase also affect alloy properties, especially creep and fatigue strength [15]. Today, the most advanced nickel-based superalloys display bimodal or trimodal γ′ size distribution with a higher volume fraction (~50 vol.%). Typically, the intergranular primary γ′ phase is in the range of 1-3 μm, while the intragranular secondary and tertiary γ′ phases have a diameter about 50-250 nm and 5-50 nm, respectively [17].

Some of the most representative morphologies of the γ′ phase are illustrated in Figure 2.4. The disadvantage of the γ′ precipitation-hardened alloys is that life of the component is ultimately restricted by the dissolution of the γ′ precipitates since it can undergo some undesirable phases during prolonged operation at elevated temperature. [5,7].

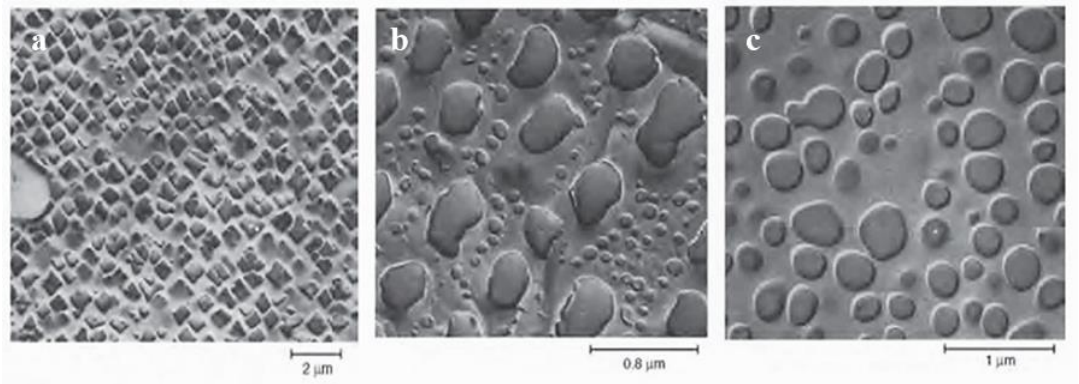

Figure 2.4. Selected morphologies of the γ′ phase in Inconel 738 alloy a) cubic-shaped, b) irregular-shaped and c) spherical-like [5].

2.2.1.2.2 Gamma Double Prime (γ″) Phase

The γ″ phase is a coherent Ni_3Nb intermetallic compound with an ordered BCT-$D0_{22}$ crystal structure which assumes a disc-shaped morphology as shown in Figure

2.5 [25,26]. This phase precipitates with an average diameter of around 600 Å, and thickness between 50-90 Å [7]. Although γ″ phase is not as widely used as the γ′ precipitate, it is the primary strengthening phase in some superalloys as Inconel 718 and 706 [7,27]. After prolonged exposure to temperatures above 650 °C, the metastable γ″ phase converts to the δ phase, leading to a slight degradation of mechanical properties [6,28].

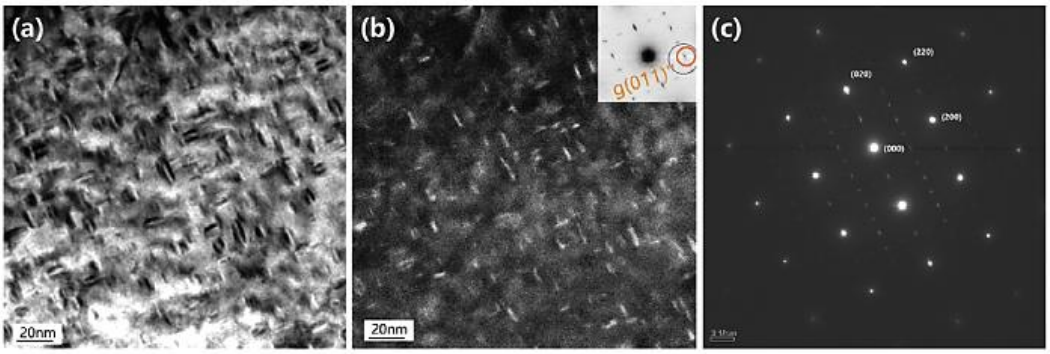

Figure 2.5. TEM images of Inconel 718 samples aged for 0.5 h showing γ″ phase: (a) BF image, (b) DF image and (c) corresponding SAED pattern [29].

As mentioned earlier, the properties of superalloys largely depend on the morphology, volume reaction, size and quantities of the precipitates formed in the matrix. In this respect, homogeneously dispersed γ′ and γ″ particles in the matrix serve as a barrier to dislocation movements, thereby increasing the mechanical properties and oxidation resistance of superalloys [14].

2.2.1.2.3 Delta (δ) Phase

The incoherent δ phase has an orthorhombic crystal structure with Ni_3Nb formula. This phase forms as an acicular-shaped precipitate in the over-aging state of Nb-containing nickel-based superalloys as given in Figure 2.6 [22,25]. The formation of the δ phase is highly influenced by temperature and mostly formed in the temperature range from 650 to 980 °C [30]. At temperatures between 650 °C and 885 °C, the δ phase initiates to precipitate at grain boundaries and then the formation of this phase is accompanied by rapid coarsening of the γ″ phase. In the

range of 840 °C to 950 °C, the plate-shaped δ phase occurs rapidly in less than 24 h [7]. Although a small amount of δ phase alters the tensile or fatigue properties of the alloy by limiting the grain growth, it is not preferred in the structure since it does not contribute any strength even in significant quantities [6,24]. The properties of these alloys have been reported to be adversely affected by the formation of large quantities of the plate-shaped δ phases. The formation of this phase consumes the niobium elements, causing the depletion of γ″ precipitates [31].

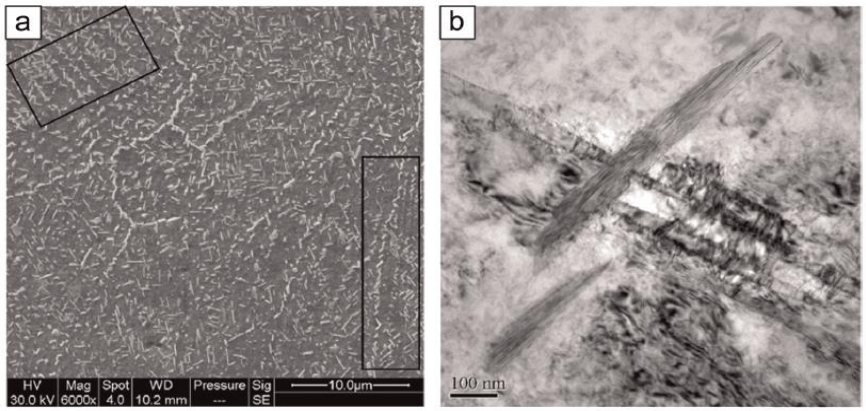

Figure 2.6. (a) SEM image showing precipitates after heat treatment and (b) magnified TEM bright field showing the acicular morphology of δ phase in (a) [32].

2.2.1.3 Carbides & Borides

Various carbide types may be present in nickel-based superalloys depending on the alloy composition, operating conditions, manufacturing process, etc. Some of the significant types are MC, M_6C and $M_{23}C_6$; wherein M represents one or more types of a metal atom (i.e. Cr, Ti, Hf, Ta or Mo) [5,6]. Such secondary phases provide beneficial or adverse effects on the properties of superalloys, which depend primarily on the morphology and distribution of the carbides. For instance, fine blocky-type carbides formed at the grain boundaries contribute to improving creep resistance and tensile strength by preventing the grain boundary sliding. However, carbides formed as continuous films along the grain boundaries can seriously degrade the properties, in particular, the ductility and impact resistance [33,34].

Because these types of carbides provide easy paths for crack initiation and propagation, which can lead to catastrophic failure of the alloys [35]. Therefore, the distribution and morphology of the carbides should be precisely controlled to improve the mechanical properties of the superalloys. Figure 2.7 demonstrates the common morphologies of carbides formed in nickel-based superalloys [33].

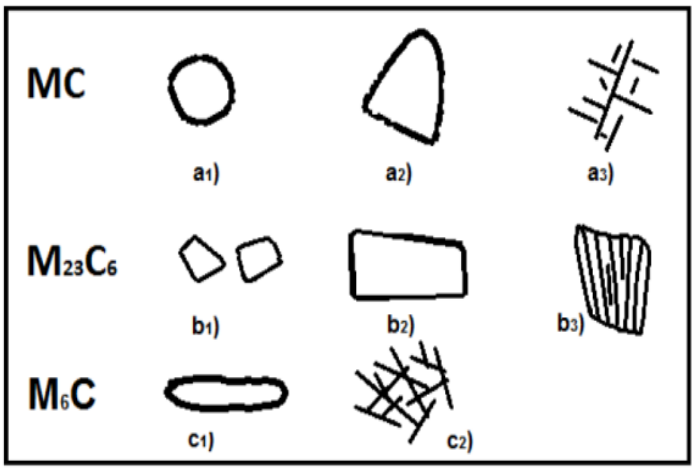

Figure 2.7. Morphologies of carbides formed in nickel-based superalloys, (a_1) globular, (a_2) blocky, (a_3) script, (b_1) discontinuous blocky particles, (b_2) plate, (b_3) cellular, (c_1) blocky and (c_2) Widmanstätten morphology [33].

MC type carbides, which are usually rich in Nb, Ti, Hf or Ta, can be formed with various morphologies such as globular-, blocky- and script-shaped during solidification. These carbides are generally heterogeneously distributed throughout the alloy in both the intragranular and intergranular regions. SEM micrographs of the carbides having various morphologies are shown in Figure 2.8. These secondary phases, which are stable at low temperatures, serve as the main carbon source for superalloys. However, they transform into more stable compounds $M_{23}C_6$ and M_6C type carbides at higher temperatures (i.e. 760-980 ºC for $M_{23}C_6$ type carbides and 815-980 ºC for M_6C type carbides) [7,36,37]. In some alloys containing a high amount of niobium or tantalum, the transformation of the MC type carbides can be delayed to temperatures between 1200 and 1260 ºC [7]. The transformation can be defined as:

$$MC + \gamma \rightarrow M_{23}C_6 + \gamma' \text{ and/or } M_6C + \gamma' \qquad \text{(Eq.2.1)}$$

$M_{23}C_6$ type carbides are usually formed on the grain boundaries as irregular and discontinuous particles during the relatively low temperature heat treatment processes or operating conditions, especially in alloys which are rich in Cr [33]. They can also found along twin boundaries, stacking faults or at twin ends [7]. These carbides may play an important role in the strengthening mechanism by restricting the dislocation movement and/or the grain boundary sliding [38]. However, the formation of $M_{23}C_6$ carbides may weaken the hot corrosion resistance of superalloys due to the reduction of chromium in the matrix. [35,39].

M_6C type carbides are generally formed by the decomposition of primary MC carbides at temperatures slightly higher than the formation of $M_{23}C_6$ carbides when the amount of tungsten and molybdenum is between 6 to 8 wt.% [7,40]. These carbides are more thermodynamically stable than $M_{23}C_6$ carbides and can be formed as block-type particles at grain boundaries or as Widmanstätten morphology in the matrix [33]. They can turn into $M_{23}C_6$ with a long-time exposure to heat treatment as defined below:

$$M_6C + \gamma \rightarrow M_{23}C_6 \qquad \text{(Eq.2.2)}$$

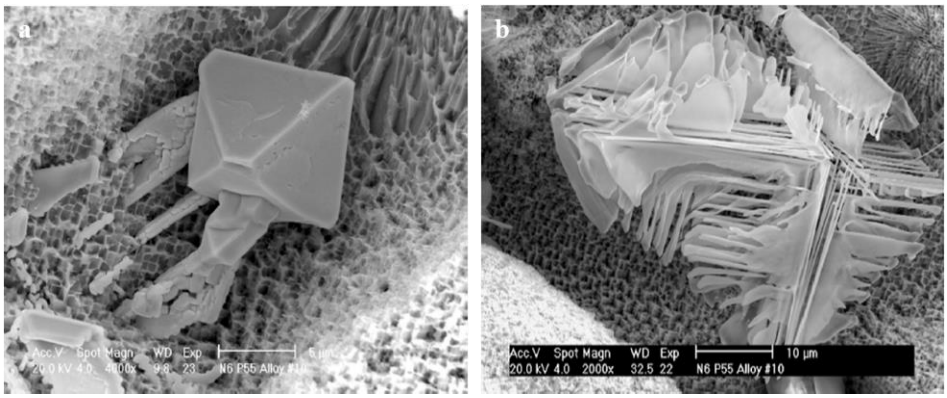

Figure 2.8. SEM micrographs of MC carbides contained within the interdendritic regions (a) blocky and (b) script [20].

M_3B_2 and M_5B_3 type borides can be also encountered at the grain boundaries of the alloys because of the low solubility in the matrix phase. These compounds are hard refractory particles with morphology varying from blocky- to half-moon-shaped. Similar to carbides, they promote an increase of the rupture strength and creep resistance of the alloys by limiting the movement of the dislocations [7].

2.2.1.4 Topologically Close Packed Phases (TCP)

Topologically close-packed (TCP) phases are unfavorable and occur during heat treatment or more commonly in operating conditions where the composition of the alloy is not carefully controlled. In addition, the presence of high amounts of BCC transition metals such as Cr, Wi Ta, Mo, and Nb leads to the formation of such phases. The TCP phases are commonly observed in nickel-based superalloys; μ-$(Fe,Co)_7(Mo,W)_6$, σ-$(Fe, Mo)_x(Ni,Co)_y$ and Laves-$(Fe,Cr,Mn,Si)_2(Mo,Ti,Nb)$ [7]. These phases tend to precipitate as a plate- or needle-like particles, acting as crack initiation and propagation sites (Figure 2.9) [41].

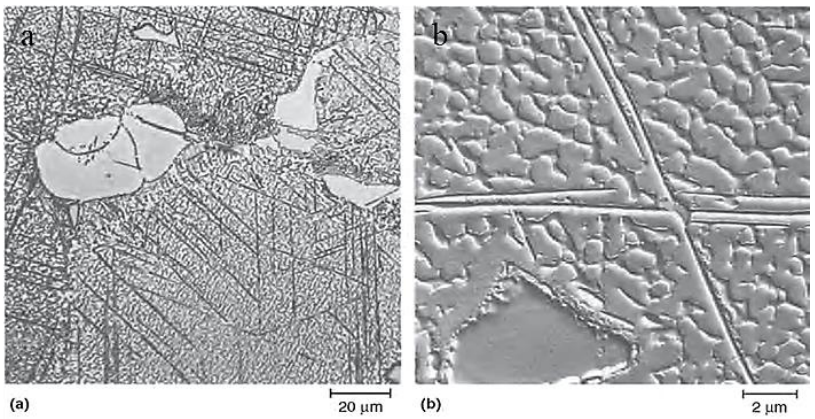

Figure 2.9. Scanning electron micrograph showing σ phase precipitated in Inconel 100 alloy (a) platelet-like and (b) Widmanstätten morphology [5].

2.2.2 Strengthening Mechanisms of Nickel-Based Superalloys

Superalloys must be capable of withstanding high stress at elevated temperatures without plastic deformation. The strengthening mechanisms of metals are usually accomplished by inhibiting the dislocation movement. There are various strengthening mechanisms leading to obtain the desired mechanical properties of superalloys, Table 2.4. Among these mechanisms, the most effective strengthening methods for nickel-based superalloys will be discussed in the following section.

Table 2.3. Strengthening mechanisms for superalloys [15].

Mechanism	**Effective Temperature**
Solid-solution strengthening	High temperature
Precipitation hardening	High temperature
ODS	Moderate temperature
Grain size control	Moderate temperature
Work hardening	Low temperature
Martensitic transformasion strengthening	Low temperature (For specific metals)

2.2.2.1 Solid-Solution Strengthening

Solid solution strengthening is achieved by adding a different soluble element to the matrix at certain concentrations. Distortion of the crystal structure caused by the mismatch of the atomic radius limits the dislocation movement and thus increases the alloy strength. Such elements having a high melting point ensure stronger lattice cohesion and decreases diffusion, especially at high temperatures [5].

2.2.2.2 Precipitation Hardening

The process is described as precipitation hardening or age hardening since small particles of the new phase are referred to as "precipitates". These precipitates strengthen the heat treated alloys depending on the interaction between the precipitates and dislocations in the matrix [42]. Strengthening mechanisms of precipitation hardening are substantially based on the two situations which are associated with the critical size of particles [43]. If the size of precipitates is smaller than the critical size, the dislocations may cross the obstacles. On the other hand, if the size of precipitates is larger than the critical size, the dislocations can pass the obstacles leaving dislocation loops around the particle [14]. In these two cases, the mechanical properties of the alloy are affected adversely in which yield strength is decreased. Therefore, the size of the precipitates should not be small or large enough to prevent the pass of the dislocation by either cutting or bowing through the obstacle as illustrated in Figure 2.10.

For nickel-based superalloys, the strengthening mechanism essentially obtained by the formation of extremely small uniformly dispersed γ' and/or γ'' precipitates in the matrix. The characteristics of the precipitates (i.e. morphology, distribution and volume fraction) and the degree of consistency between the precipitates and the matrix strongly influence the strengthening mechanism of the heat treated alloys. [17]. In fact, the strength of superalloys typically increases with increasing temperature until it reaches a temperature of about 800 ºC. At temperatures above 800 ºC, the strength decreases rapidly as the particles become coarse and initiate to transform into the detrimental phases [6].

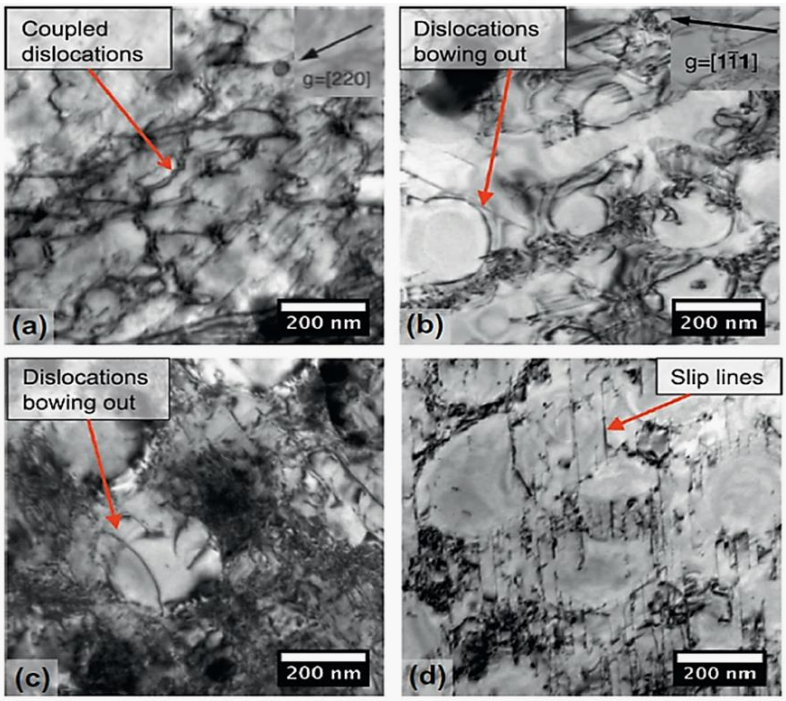

Figure 2.10. TEM micrographs of the model microstructures deformed at 500 ^{o}C (a) fine γ′ phase, (b) medium γ′ phase, (c) and (d) coarse γ′ phase [17].

2.3 Inconel 718 Superalloy

Inconel 718 alloy was firstly designed by the International Nickel Corporation in the 1950s to overcome the poor weldability of nickel-based superalloys. It is an age-hardening nickel-based superalloy with Cr and Fe as major alloying elements and relative Nb and Mo content. [28,44]. Chemical compositions of Inconel 718 alloy defined by AMS 5383 standard are given in Table 2.5.

Table 2.4. Elemental compositions determined by AMS 5383 standard Inconel 718 alloy [45].

Element	Chemical Composition (wt%)
Ni (plus Co)	50.00 – 55.00
Cr	17.00 – 21.00
Nb (plus Ta)	4.75 - 5.50
Mo	2.80 - 3.30
Ti	0.65 - 1.15
Al	0.20 - 0.80
Co	1.00 max
C	0.08 max
Mg	0.35 max
Si	0.35 max
P	0.015 max
Si	0.015 max
B	0.006 max
Cu	0.30 max
Fe	Bal.

Inconel 718 alloy has been extensively utilized to manufacture the high-pressure compressor blades, discs, casing and other high temperature parts for many industrial applications including aerospace, nuclear energy and petroleum industry [46,47]. Inconel 718 alloy possesses remarkable properties such as high temperature strength, excellent fatigue and creep resistance as well as good hot corrosion and oxidation resistance in aggressive environments [48-50]. In addition, welding characteristics of Inconel 718 alloy, especially its resistance to post-weld cracking and mechanical stability at high temperatures are outstanding [51,52]. Depending on these properties mentioned above, the alloy is commonly used in many fields that require long operation periods at operating temperatures up to 700 °C [53-55]. Some properties of Inconel 718 alloy are tabulated in Table 2.6 and Table 2.7.

Table 2.5. Material properties of Inconel 718 alloy [14].

Physical Properties	Density	8.192 g/cm^3 (0.296 lb/in^3)
	Melting range	1260 - 1336 °C
Thermal Properties	Thermal conductivity	11.4 W/m · K
	Specific Heat Capacity	0.435 J/g-°C
Electrical Properties	Electrical resistivity	1218 nΩ · m

Table 2.6. Effect of temperature on the mechanical properties of wrought Inconel 718 alloy [14].

Temprature (°C)	**Yield strength - 0.2% (MPa)**	**Tensile strength (MPa)**	**Elongation 2" (%)**
21	1185	1435	21
540	1065	1275	18
760	740	950	25

As given in Figure 2.11, the microstructure of Inconel 718 commonly composed of γ matrix as well as other intermetallic phases such as coherent γ″ (Ni_3Nb) and γ′ ($Ni_3(Al,Ti)$) precipitates, Laves ($(Ni,Cr,Fe)_2(Nb,Mo,Ti)$) phase, incoherent δ (Ni_3Nb) phase and MC (Nb,Ti(C)) type carbides, Table 2.8.

Table 2.7. Phases commonly observed in Inconel 718 [56].

Phase	**Crystal Structure**	**Chemical Formula**
γ	FCC	Ni
γ″	BCT (ordered $D0_{22}$)	Ni_3Nb
γ′	FCC (ordered $L1_2$)	$Ni_3(Al,Ti)$
δ	orthorhombic (ordered $D0_\alpha$)	Ni_3Nb
MC	cubic B_1	(Nb,Ti)C
Laves	hexagonal C_{14}	$(Ni,Fe,Cr)_2(Nb,Mo,Ti)$

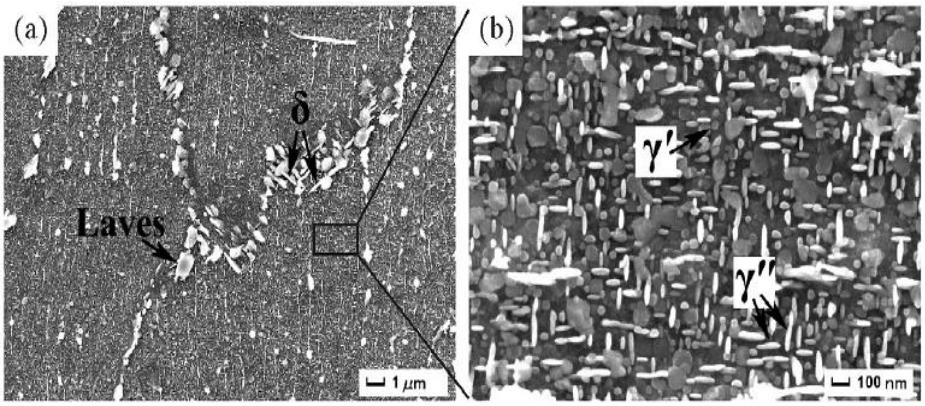

Figure 2.11. SEM images of the heat treated sample produced by SLM method, (a) the precipitates at the grain boundaries and in the matrix, and (b) magnified disc-like γ″ and circular γ′ phases [22].

The main strengthening mechanism of Inconel 718 alloy is accomplished by heat treatment processes consisting of solution heat treatment and double aging treatments [53]. Solution treatment promotes the diffusion of segregate elements and the dissolution of the brittle phases in the matrix like Laves and carbides. Aging treatment offers the formation of strengthening primarily $D0_{22}$-ordered γ″ and slightly $L1_2$-ordered γ′ precipitates by adjusting the cooling rate and exposure time [32].

It is already known that the formation of strengthening phases is strongly influenced by manufacturing or heat treatment processes [29,57,58]. According to the time-temperature-transformation (TTT) diagram for Inconel 718 (Figure 2.12), the γ″ phase can be converted to the δ phase when exposed to prolonged aging or service conditions. It has been found that the formation of the acicular-shaped δ phase consumes Nb from the matrix and impedes the precipitation of the strengthening γ″ phase, resulting in loss of strength and creep life of the superalloy. However, it was also reported that the appropriate amount of δ phase with globular morphology can prevent grain boundary sliding and thus alter the tensile or fatigue properties and creep fracture [45]. In addition, the relatively high Nb content can lead to the precipitation of Nb-rich MC type carbide and/or Laves phase [29].

Therefore, it is important to understand the precipitation behavior of the Inconel 718 alloy and the corresponding mechanical properties.

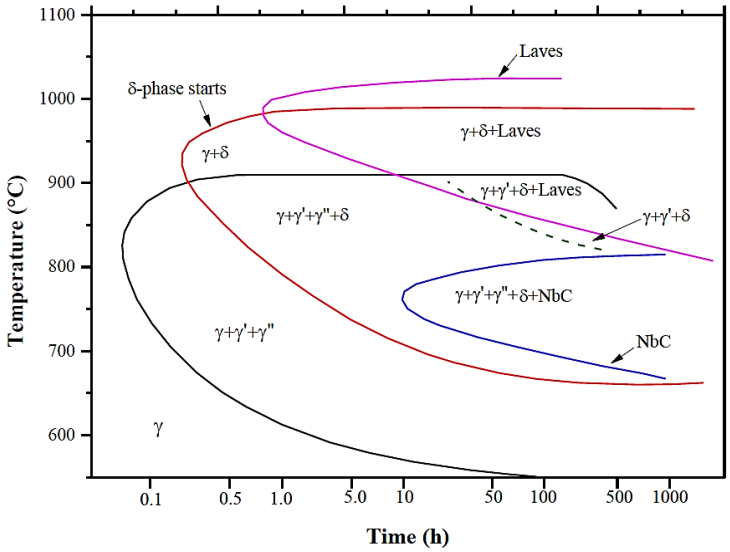

Figure 2.12.Time-temperature-transformation (TTT) diagram for Inconel 718 [59].

2.4 Additive Manufacturing Technology

Additive manufacturing (AM), also known as rapid prototyping is the process of joining materials to make objects from three dimensional (3D) computer-aided design (CAD) model data. It is a growing new industry sector to manufacture more complex functional components with lower energy costs and shorter manufacturing time that cannot be manufactured by conventional manufacturing techniques. In 1986, the first additive manufacturing technique was utilized by researchers at the University of Texas [60]. From the beginning of these days, many new AM processes have been evolved and successfully implemented in numerous fields including aerospace, defense, automotive, healthcare and industrial products according to the ASTM F42 Committee formed in 2009 [60].

In this technology, the components are manufactured in a layer-by-layer format without the need for machining operation or final installation. This process consists of the following steps [61];

- Design of the component to be manufactured by CAD program,
- Transferring of the drawing to the 3D printer by converting it to STL (STereoLithography) format which is a file that changes the surface of the scanned model with a mesh of triangulated surface segments,
- Determination of the most suitable prototyping method for manufacturing.

The most significant benefit of AM lies in the fabrication of extremely complex geometric shapes in a single production stage which means that the number of assembly operations is removed. In addition, the use of today's AM technology allows manufacturers to manufacture all components with extremely precise tolerances, including nuts and screws. Therefore, AM technology improves product quality and extends component life by reducing the number of component defects. On the contrary, conventional manufacturing methods require multiple steps to produce complex components. Another important advantage of the AM process is the opportunity for design freedom. Using CAD software enables manufacturers to make changes considerably faster. It only needs change to design a file rather than changing the manufacturing equipment. Other advantages of AM processes can be also summarized as follows [62-64];

- Reducing the material waste that accrues in conventional manufacturing, up to 25 times less versus machining,
- Elimination of some of the time-consuming operations including machining, joining, injection molding, etc.
- Manufacturing of lightweight structures which allows manufacturing the lattice structure or combines porous with solid materials into one component,
- Elimination of the required tooling or molding parts which results in a reduction of the cost and time by accelerating prototyping,
- Reducing energy consumption by using less material and eliminating steps in the manufacturing process.

2.4.1 Metal Additive Manufacturing Processes

Metal AM processes use wire or powder as the starting material, laser or electron beam as the energy source. This technique can be categorized as directed energy deposition and powder bed fusion in terms of metallic feedstock, energy source, build volume, etc. [60]. Some of the metallic materials including nickel-based superalloys (e.g. Inconel 718 [65] and Hastelloy X [66]), cobalt-based superalloys [67], titanium alloys [68] and aluminum alloys [69] have been already produced with using AM processes. Some of the metal AM methods and their manufacturers are tabulated in Table 2.9.

Table 2.8. Categorization of metal additive manufacturing techniques [62,70].

Technique	Process	Manufacturer
Directed energy deposition	LENS	Optomec
	DMLS	Insstek
	LD	Irepa laser, Huffman, Trumpf
Powder bed fusion	SLS	3D Systems, MC Machinary Systems, Farsoon Technologies
	EBM	Arcam
	SLM	SLM Solutions, EOS, 3D Systems,Renishaw, Concept Laser

2.4.1.1 Directed Energy Deposition (DED) Processes

DED method can be categorized as wire feedstock developed from the traditional welding process and powder flow feedstock developed by Sandia National Laboratory in 1996 according to material feedstock type [71,72]. In DED processes, the starting material is deposited and melted simultaneously with an electron beam or laser, thereby forming a molten pool on the substrate. With the

DED process, metal powders or metal wire filaments are sprayed through a single or multiple nozzles onto the substrate surface to form an additional metal layer. Manufacturing efficiency may be enhanced by adjusting the process parameters such as characteristics of starting material (i.e. material feedstock type and feeding rate), laser power, scanning strategy, etc. [73]. A schematic illustration of the laser-based DED process is given in Figure 2.13.

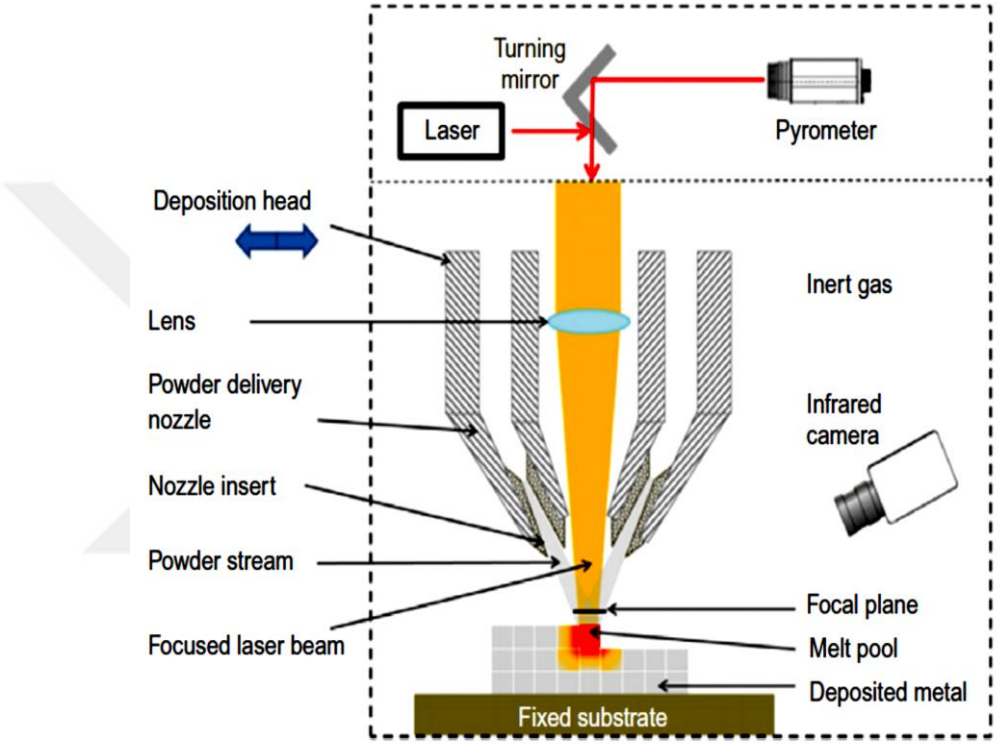

Figure 2.13. Schematic illustration of direct energy deposition (DED) technique [74].

2.4.1.2 Powder Bed Fusion (PBF) Processes

In PBF processes, the components are fabricated to the desired shape by controlled melting or sintering of the subsequent metallic powders by an energy source. Basically, the production process initiates by spreading a thin layer of powder onto the building platform, and then melting the powder according to the geometry model. The platform is then lowered in the z-direction and the processes are repeated until the component is completed. Among the PBF methods, Selective

laser melting (SLM) and electron beam melting (EBM) techniques are the most commonly utilized processes for the production of various metal components. The working principle of the process is similar for both SLM and EBM methods with slight differences [60]. A schematic illustration of the laser-based PBF method is shown in Figure 2.14.

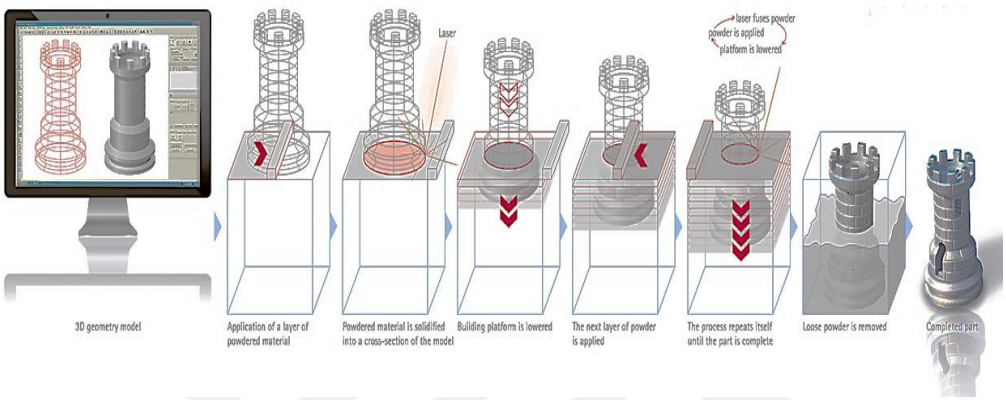

Figure 2.14. Schematic illustration of laser-based powder-bed fusion (PBF) additive manufacturing technologies [56].

2.4.1.2.1 Selective Laser Melting Method

Selective laser melting (SLM) is an AM technique that offers complex-shaped metallic components to be printed from 3D-CAD data with almost full density (> 99%) and dimensional accuracy in a single step. The principle of the process is the fabrication of the components layer-by-layer directly with the controlled melting of metal powders with a focused laser beam [32]. In the SLM process, metal powders are spread uniformly on a platform at a certain layer thickness according to the cross-sectional geometry of the part to be formed. After that, the powders are melted with lasers and then the melted powders are solidified to form the layer. The platform is then shifted down to layer thickness and filled with a new layer of powder. These cycles are repeated until the part is completed as designed, then the part is removed from the platform [75,76]. The properties of the printed parts are highly influenced by the processes parameters (i.e. initial powder composition,

layer thickness, laser power, scanning strategy, etc.) [44,77]. A schematic illustration of the SLM technology is given in Figure 2.15.

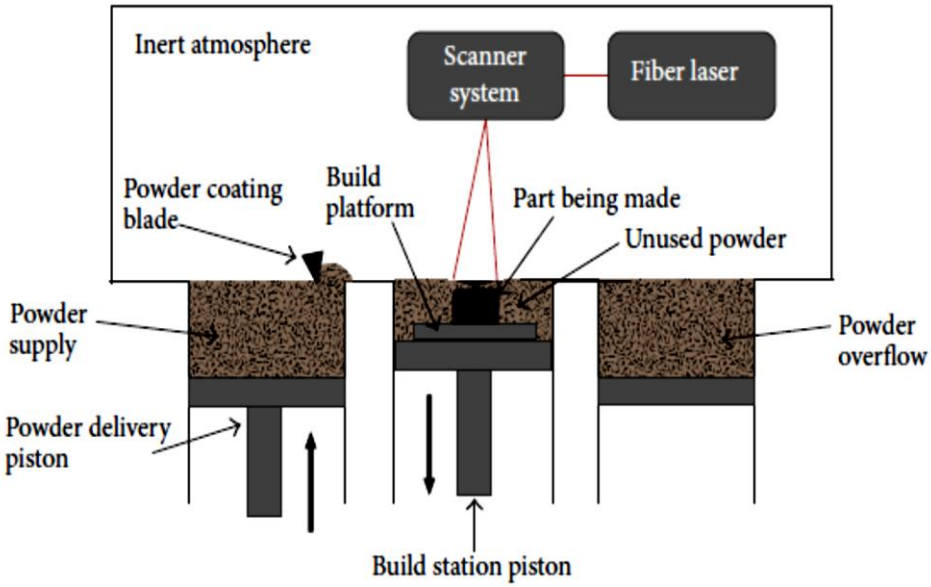

Figure 2.15. Schematic illustration of selective laser melting (SLM) technology [78].

SLM method provides several advantages, such as reducing lead-time, high material consumption efficiency and reducing investment cost for the tooling or mold. Furthermore, this technology can greatly reduce the production steps which eliminates the joining operations like welding or brazing and their detrimental effects on microstructure, resulting in prolonging the service life of the materials produced [79-81].

However, some undesired features can appear in the microstructure of fabricated parts due to the high temperature gradient and rapid solidification rate resulted from the SLM process. Problems encountered during the SLM processing can be specified as high residual stresses, formation of non-equilibrium phases, directional grain growth, segregation of refractory elements or formation of defects such as cracks, pores, etc. [80,81]. The residual stress can significantly affect the components' dimensional and geometry accuracy as well as mechanical properties. Therefore, post-processing heat treatments are critical for eliminating these defects in fabricated parts to enhance the properties of materials and meet the requirements

of demanding operating conditions. In addition, preheating of the powder bed or optimization of the process parameter can efficiently reduce the unfavorable conditions during the SLM process.

2.4.1.2.2 Electron Beam Melting (EBM) Method

Electron beam melting (EBM) method, Figure 2.16, was developed mainly from scanning electron microscopy (SEM) technique and was patented in 2001 by Arcam AB, Sweden [82]. This method uses a high-power electron beam to melt the powder to form a layer and simultaneously fuses with the pre-solidified layers in a powder bed. Unlike the SLM process, a high vacuum is utilized throughout the manufacturing steps which make this process particularly suitable for the fabrication of highly reactive materials e.g., titanium. Additionally, the base platform is first preheated slightly above the operation temperature (> 870 K), before applying the first layer of powder. Controlling the process parameters of the EBM method is more difficult than the SLM method. This technique involves more variables including laser power, beam diameter, scanning strategy and speed, preheating temperature, etc. [77].

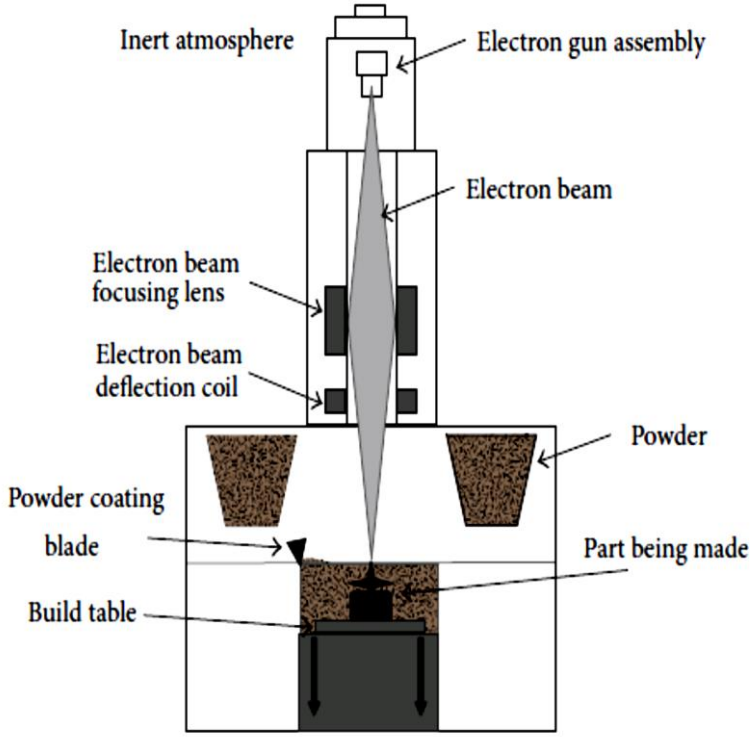

Figure 2.16. Schematic representation of electron beam melting (EBM) technology [78].

Recently, the use of both additive manufacturing methods has increased in many application areas. Due to the advantages listed below (Table 2.10), they are particularly preferred in the production of functional components with complex geometries.

Table 2.9. Some advantages of the both SLM and EBM processes [62,63].

SLM	EBM
Geometric freedom for engineering product designers	
Production of near-net-shaped components	
Comparable mechanical properties with the convetional production technology	
Production of lightweight materials	
Minimum material waste	
Less tooling and set up costs	
Short production cycle time for parts in small series	
Use of a large range of materials	Reduction of oxidation due to vacuum environment
Better surface finish	Reduction of residual stress due to preheating step

2.5 Heat Treatment of Inconel 718 alloy

The properties of superalloys can be improved by manufacturing process optimization and/or heat treatment applications. Heat treatment is applied to achieve optimum material performance depending on the change in the solubility of elements by heating and cooling processes. It is known that these processes affect the microstructure of the Inconel 718 alloy, including the separation of alloying elements and grain growth. Xiao et al. found that the formation of TCP phases (i.e. Laves and δ phases) and segregation of alloying elements along the grain boundaries of the Inconel 718 alloy were reduced by heat treatment at 1066 ºC [83]. One of the series of processes applied to the Inconel 718 alloy typically includes solution treatment followed by a single or double aging step.

2.5.1 Solution Heat Treatment

Solution treatment is performed at relatively high temperatures, over γ' solvus temperature to achieve an almost homogeneous concentration of elements in the solid solution by dissolving the second phases. Various studies have been performed regarding the solution treatment process of Inconel 718 between 980-1200 ºC for 1 to 2 hours with different cooling rates [53]. Although the standard process for casting and wrought alloys was carried out at 980 ºC, the solution temperature was fixed to 1032 ºC according to the results obtained. It was observed that carbides and brittle Laves phases remain undissolved at 980 ºC. Increasing the solutionizing temperature leads to improve the dissolution rate of these phases, which results in the niobium and titanium elements solved back into the matrix. As mentioned earlier, these elements have a strong effect on improving the mechanical properties of Inconel 718 alloys due to the formation of the γ″ and γ′ precipitates, respectively [28].

Tucho et al. performed a solution process for different soaking times at 1100 ºC and 1250 ºC to examine the effect of high solution temperature on the microstructure of Inconel 718 alloys fabricated by the SLM method. They found that the increasing of soaking time resulted in the growth of the grains and carbides within the matrix for both 1100 ºC and 1250 ºC temperatures. Additionally, the Laves phase with a size of approximately 100 nm remained as undissolved in the matrix even at 1250 ºC [53].

M. Ni et al. also found that the transformation of the columnar to equiaxed grains was increased by increasing solution temperature from 980 to 1100 ºC, resulting in decreasing of the fraction of the low angle grain boundaries. Increasing solution temperature caused grain growth which leads to lower yield and tensile strength [84].

2.5.2 Aging

Aging is carried out at an intermediate temperature, normally in the range of 425-870 ºC with various soaking time to allow the precipitation of the strengthening phases in the matrix. The resulting phases provide an increase in the mechanical properties of the Inconel 718 alloy by blocking the dislocation movement. For the fully heat treated Inconel 718 alloy, the volume fractions of strengthening γ' and γ″ phases are 5% and 20%, respectively. Some authors stated that these phases precipitate between 700 and 900 ºC for short soaking times while others said that they form at a relatively lower temperatures, i.e. between 550 and 660 ºC for long aging times. Also, some authors explained that the γ″ phase generally forms at higher temperatures (720 ºC) while γ' phase occurs at lower temperatures (620 ºC) [51,85]. Moreover, the secondary carbides precipitate in the temperature ranges of 730 to 1040 ºC, which influence the mechanical properties of the alloy. Additionally, some undesirable δ phase can be formed with acicular-shaped morphologies. Therefore, it is significant to optimize precisely the size, shape and volume fraction of γ' and/or γ″ phases as well as aging temperature and soaking time to determine the microstructure and mechanical behavior [29].

S. Raghavan et al. found that the aging treatment caused the formation of nano-sized γ″ and γ' phases and needle-shaped δ phase as well as a large amount of carbides in the SLM-produced Inconel 718 alloys. They reported that the mechanical properties of the alloy were enhanced significantly compared to the as-produced alloy due to the presence of strengthening phases [79].

W. Huang et al. studied the effect of different aging temperatures on the mechanical behavior of the SLM-produced Inconel 718 alloy. The microhardness results demonstrated that complete precipitation of the strengthening phases was obtained when the aging treatment was performed ranges from 680 to 720 ºC [47].

CHAPTER 3

EXPERIMENTAL PROCEDURE

3.1 Starting Materials

The gas atomized Inconel 718 powders were used as starting materials for the SLM process. The chemical composition of the powder particles (Table 3.1) was found to be in accordance with the AMS 5383 standard. Malvern Mastersizer 2000 with Hydro 2000S module was employed to determine the particle size distribution of the powders as demonstrated in Figure 3.1. The average particle size of the Inconel 718 powders was approximately 26.3 μm, and the particle size range was observed to change between 18.5 and 37.3 μm.

Table 3.1. Elemental composition analysis of the gas atomized alloy powders compared with AMS 5383 Standard Specification designed for wrought Inconel 718 alloy.

	Powders Used in the Present Study	**AMS 5383 Standard for Wrought Alloy**
Element	**wt.%**	
Ni	52.82	50-55
Cr	18.91	17-21
Nb	5.39	4.75-5.5
Mo	3.27	2.8-3.3
Ti	1.06	0.65-1.15
Al	0.75	0.2-0.8
Fe	17.80	Balance

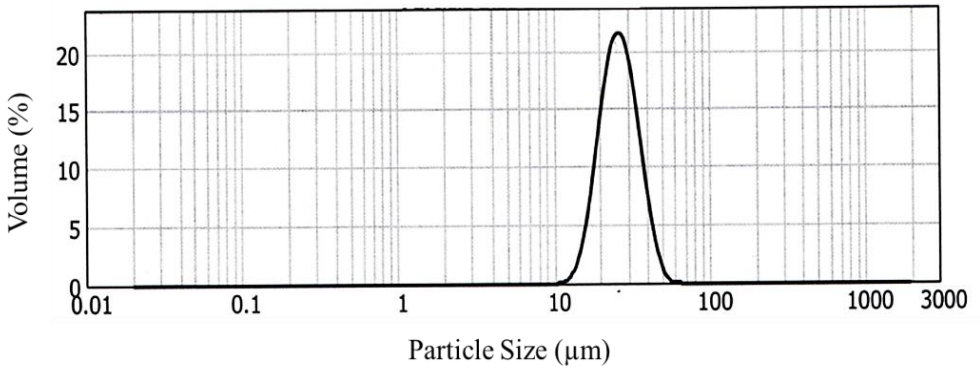

Figure 3.1. Particle size distribution of the used Inconel 718 alloy powders.

The morphology of the particles plays an important role in determining the mechanical properties of the fabricated Inconel 718 alloy to obtain fully dense parts during SLM process. As shown in Figure 3.2, the powder particles have perfectly spherical-shaped morphology with a fine dendritic network resulting from the rapid solidification during gas atomization.

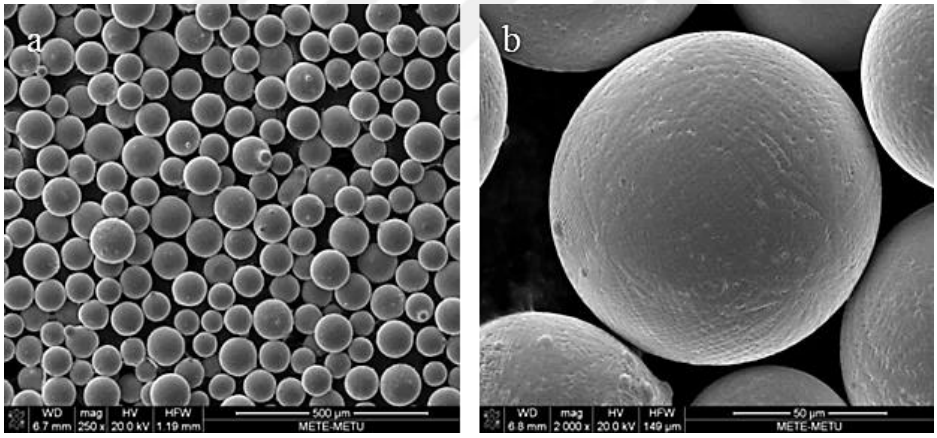

Figure 3.2. SEM micrographs of (a) spherical Inconel 718 powders and (b) magnified particles showing the fine dendritic network.

3.2 Manufacturing of SLM-Produced Inconel 718 Alloy

The production of the Inconel 718 alloy was carried out using EOS M290 machine equipped with a 400 W Yb-fiber laser. SLM processing parameters including scan velocity, hatch spacing and the thickness between powder layers were utilized as

decribed by EOS Company. Standard process parameters include layer thickness of 40 µm, hatch spacing of 110 µm, laser power of 285 W, laser speed of 960 mm/s and hatch rotation of 67° [38,86]. Controlled argon atmosphere was used in the building chamber of the SLM machine to minimize the possibility of oxidation. In addition, the building platform was heated to 80 ºC to diminish the thermal gradient between the platform and the manufactured components. The samples' longitudinal axes were either parallel or perpendicular to the building platform, designating as horizontally and vertically built, respectively. The schematic representation of as-fabricated specimens is as demonstrated in Figure 3.3.

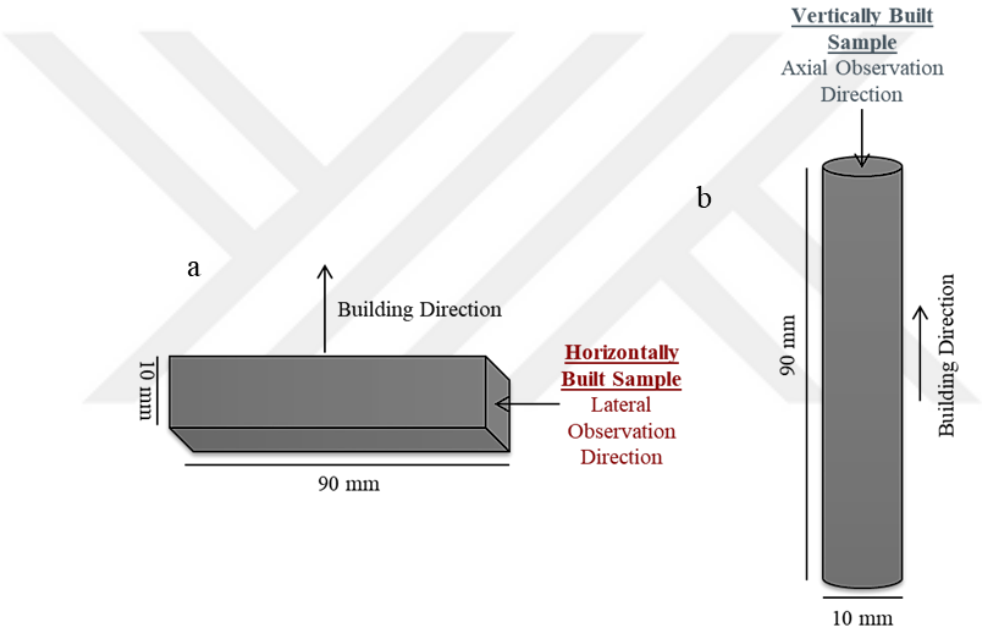

Figure 3.3. Schematic representation of the geometry of as-fabricated specimens in regard to the building direction (a) horizontally and (b) vertically built samples.

3.3 Heat Treatment Procedure

Various heat treatment conditions have been applied to investigate the effect of microstructure and building direction on the mechanical behavior of the as-fabricated samples. In the present study, optimization of the alloy properties was achieved by changing the aging parameters while keeping the solution treatment

parameters constant. Before the heat treatment processes, the samples were cleaned in an ultrasonic bath by soaking in acetone for 15 minutes and then cleaned with ethanol. All horizontally and vertically built samples were solutionized at 1040 ºC for 2 hours and then air-cooled. Subsequently, aging treatments were performed at 700 ºC for different soaking times (5 to 34 hours) denoted as PHT-soaking time. Moreover, a pair of the horizontally and vertically built samples were subjected to standard aging treatment process defined by the standard AMS 5664 (denoted as SHT) for comparison. The main purpose of these processes was to dissolve the brittle Laves phase and carbides in the matrix to ensure the formation of the strengthening phases by aging. The details of the post-processing heat treatments are listed in Table 3.2.

Table 3.2. Heat treatment parameters used for post-processing of SLM processed Inconel 718 alloy.

Heat Treatment Condition	Solutionizing	Aging	Phases Present
SHT - (AMS 5664)	1040 °C/2 h AC	720 °C/8 h FC - 620 °C/8 h AC	γ, γ′, γ″ and δ
PHT-5h		700 °C/5 h AC	γ, γ′ and γ″
PHT-8h		700 °C/8 h AC	γ, γ′ and γ″
PHT-16h		700 °C/16 h AC	γ, γ′, γ″ and δ
PHT-28h		700 °C/28 h AC	γ, γ′, γ″ and δ
PHT-34h		700 °C/34 h AC	γ, γ′, γ″ and δ

SHT - Standard Heat Treatment / PHT - Peak Heat Treatment

3.4 Characterization Studies

3.4.1 Metallographic Sample Preparation and Examination

For microstructural analysis, the samples were sectioned by a precision abrasive cutter (Buehler IsoMet 5000). The surfaces of the samples were then ground using SiC papers up to 3000 grit size and then polished with diamond suspension from 6

to 1 μm. After cleaning with deionized water and ethanol, the samples were etched using Kalling's reagent for 30-50 seconds (Table 3.3).

Table 3.3. Composition of Kalling's Reagent.

Etchant	Composition	Method
Kalling's Reagent	40 ml HCl, 2 g $CuCl_2$ and 40 ml ethanol	Immersion

3.4.1.1 Scanning Electron Microscopy (SEM)

Microstructural observations of both as-fabricated and heat treated samples were conducted using a Scanning Electron Microscope (SEM) (Nova NanoSEM 430, FEI Company, Eindhoven, the Netherlands) operated at 20kV accelerating voltage. The size of the present phases and the average grain size of the heat treated samples were measured from SEM images. In addition, the chemical composition of the samples was determined by energy dispersive spectroscopy (EDS) detector of the SEM.

3.4.1.2 Electron Backscatter Diffraction (EBSD)

Electron backscatter diffraction (EBSD) mapping was performed to observe the grain direction and texture in detail for all samples. Prior to the EBSD analysis, the samples were prepared by grinding up to 3000 grit SiC paper and then electro-polished with the A2 electrolyte (Table 3.4) using a Struers LectroPol5 machine with a 30 V voltage for a few seconds. After the electropolishing step, the samples were cleaned with ethanol and deionized water and subsequently dried with air.

Table 3.4. Composition of the A2 Electrolyte used for electropolishing.

Electrolyte	Composition
A2	90 ml distilled water, 730 ml ethanol, 100 ml butoxyethanol and 78 ml perchloric acid

3.4.2 X-Ray Diffraction (XRD) Analysis

X-ray diffraction (XRD) analysis was conducted to determine the phases present in the as-fabricated samples as well as the phases formed after heat treatment processes. Rigaku DMAX 2200 X-Ray Diffractometer was employed using Cu-Kα radiation (λ = 1.5406) with a fixed scan speed of 1°/min and X-ray generator power set at 30 mA and 40 kV. A representative sample was analyzed at varying scanning rates (i.e. 0.1°/min, 0.5°/min, 1°/min and 2°/min) to determine the most convenient scanning rate. In all four cases, same phases were determined in the test sample, and thus all XRD analyses were carried out at 1°/min scanning rate.

3.5 Mechanical Tests

3.5.1 Hardness Measurement

Vickers microhardness measurements were performed using a standard microhardness tester (HMV-2, Shimadzu Scientific Instruments, Kyoto, Japan) on the polished sections of samples with a load of 2 kg (further denoted as HV2) and holding-time of 10 seconds. The microhardness measurements were taken from at least 7 different points to obtain the average hardness values of each sample.

3.5.2 Tensile Test

Tensile test samples with gage length of 30.0 mm were processed from both horizontally and vertically built samples according to ASTM E21 standard. The drawing of the tensile test samples is given in Figure 3.4. Before the tests, all the tensile testing samples were heat treated according to the PHT-8h condition. This process was selected as the best option among all of the heat treatment conditions according to the hardness values obtained by varying conditions the details of which will be discussed in the Results and Discussion chapter.

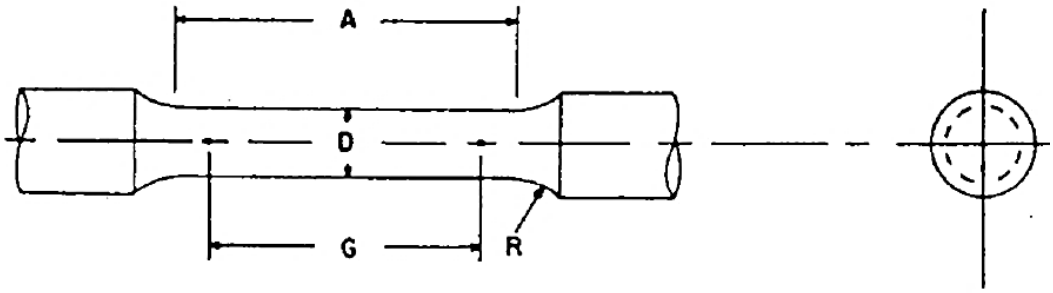

Dimensions, mm [in.]	
G- Gauge length	30.0 + 0.1 [1.250 + 0.005]
D- Diameter	6.0 +0.1 [0.250 + 0.005]
R- Radius of fillet, min	6 [0.188]
A- Length of Reduced section, min	30 [1.4]

Figure 3.4. Drawing of round tension test specimen according to ASTM E21 standard [87].

Tensile tests were performed using an Instron 5582 universal testing machine with a load cell capacity of 100 kN at a constant crosshead speed of 0.5 mm/min at both room temperature and elevated temperatures (at 600, 700, 800 and 900 ºC). The yield strength (YS) of the samples was measured by the 0.2% offset method. Two series of tensile testing samples were prepared for each of the test conditions to ensure the accuracy of the results.

High temperature tensile tests were performed at a constant crosshead-speed of 0.5 mm/min using essentially identical samples and procedures as room temperature tensile tests. Unlike the room temperature tests, the samples were heated and cooled in a furnace, and the temperature of the process was monitored by thermocouples attached at the center of the gage length of samples. In addition, strain measurement was made by using extensometer attached directly to the samples.

3.6 Density Measurement

Archimedes' method was carried out to measure the density and porosity values of the as-fabricated parts by PRECISA XB220A balance equipped with density determination kit. The samples were firstly weighed in air, and then immersed into xylol solution ($CH_3C_6H_4CH_3$) for 2 hours to allow impregnation of xylol into the pores. Subsequently, the samples were weighed in xylol solution, and then they were removed from the solution and weighed again in the air.

Calculations of the density and porosity values of the samples were conducted using equations 3.1-3.4. During determination of total porosity percentages of as-fabricated samples, P_{total} (%), by Eq. (3.3), volumes of the samples, V_{sample}, were initially calculated according to Eq. (3.1). Then, the densities of the samples, ρ_{sample}, were calculated using Eq. (3.2).

$$V_{Sample} = \frac{m_{a,x} - m_{x,x}}{\rho_{xylol}} \qquad \text{(Eq. 3.1)}$$

$$\rho_{sample} = \frac{m_a}{V_{sample}} \qquad \text{(Eq. 3.2)}$$

$$P_{total(\%)} = 100 - (\frac{\rho_{sample}}{\rho_{alloy}} \times 100) \qquad \text{(Eq. 3.3)}$$

$$\text{Relative density} = 100 - P_{total(\%)} \qquad \text{(Eq. 3.4)}$$

Where,

ρ_{xylol}: density of xylol (0.861 g/cm^3),

ρ_{alloy}: density of the wrought Inconel 718 alloy (8.22 g/cm^3),

m_a: mass of the sample in air,

$m_{a,x}$: mass of xylol impregnated sample in air,

$m_{x,x}$: mass of xylol impregnated sample in xylol solution,

$P_{total\ (\%)}$: percentage of total porosity.

CHAPTER 4

RESULTS AND DISCUSSION

4.1 Microstructural Examinations

4.1.1 As-Fabricated Inconel 718 Alloy

Selective laser melting (SLM) method is capable of producing samples with more than 99.5% relative densities. Results indicated that the average relative density of SLM-produced Inconel 718 alloy components is ca. 99.85% of the bulk density, which is accepted in the standard. This can be attributed mostly to the spherical-shaped morphology of the powders used playing an important role in obtaining fully dense parts during the SLM process.

Optical microscope images of the as-fabricated Inconel 718 samples in as-polished condition are presented in Figure 4.1. The blocky-shaped particles of ca. 5 μm size distributed heterogeneously throughout the alloy matrix during the SLM process. These particles are thought to be primary MC-type carbides which were found to be rich in Ti element according to the EDS analysis. The chemical composition of these particles for both horizontal and vertical building directions are given in Table 4.1 and Table 4.2, respectively.

These types of carbides generally do not dissolve during the manufacturing or heat treatment processes due to their high stability even at high temperatures. It was observed that the primary TiC carbides formed in both intragranular and intergranular regions with a relatively low volume fraction. As mentioned previously, the characteristics of the primary carbides may affect the properties of the superalloys positively or negatively by either preventing dislocation movement or acting as a crack nucleation site [85].

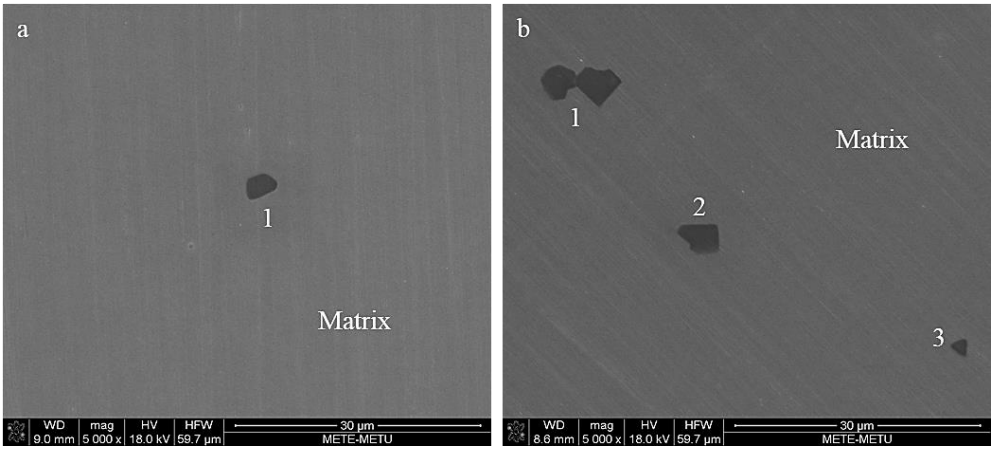

Figure 4.1. SEM images of the as-polished SLM Inconel 718 samples in as-fabricated condition (a) horizontally built and (b) vertically built.

Table 4.1. EDS analysis of the TiC carbides formed in horizontally built Inconel 718 samples.

	Elements (in wt. %)								
Points	**Ni**	**Cr**	**Fe**	**Nb**	**Mo**	**Ti**	**Al**	**Co**	**C**
1	6.49	3.27	2.59	9.53	1.68	75.3	0.27	0.24	0.63
Matrix	51.7	18.54	17.71	5.51	4.24	0.92	0.7	0.56	0.10

Table 4.2. EDS analysis of the primary MC type carbide formed in vertically built Inconel 718 samples.

	Elements (in wt. %)								
Points	**Ni**	**Cr**	**Fe**	**Nb**	**Mo**	**Ti**	**Al**	**Co**	**C**
1	4.72	2.54	1.87	8.85	1.61	79.12	0.5	0.24	0.54
2	8.14	4.24	3.43	8.17	2.18	72.65	0.36	0.27	0.56
3	2.91	1.87	1.27	10.72	2.17	79.73	0.54	0.25	0.54
Matrix	51.48	18.61	17.83	5.6	4.04	1.07	0.56	0.62	0.11

The microstructures of the as-fabricated Inconel 718 alloys for both building directions are given in Figure 4.2 and Figure 4.3. At lower magnifications, the melt pool morphology with typical arc-shaped features can clearly be observed in the lateral direction (Figure 4.2(a), (c) and Figure 4.3(a), (c)). The melt pool depth and width were measured to be approximately 50 and 100 μm, respectively. The melt pool morphology is the common feature of SLM-fabricated components which was also observed by Amato et al. on Inconel 718 [88], D. Tomus et al. on Hastelloy X [66] and Bi et al. on Inconel 100 [89]. It was already reported that the microstructure is in the form of an arc-shaped curve developed according to the Gaussian energy distribution of the laser beam [30,32,45] .Furthermore, the laser beam scanning paths were detected in the axial observation direction (Figure 4.2(b) and Figure 4.3(b)). The width of the scanning paths was measured to be ~100 μm which was close to the hatch distance implemented in the fabrication method.

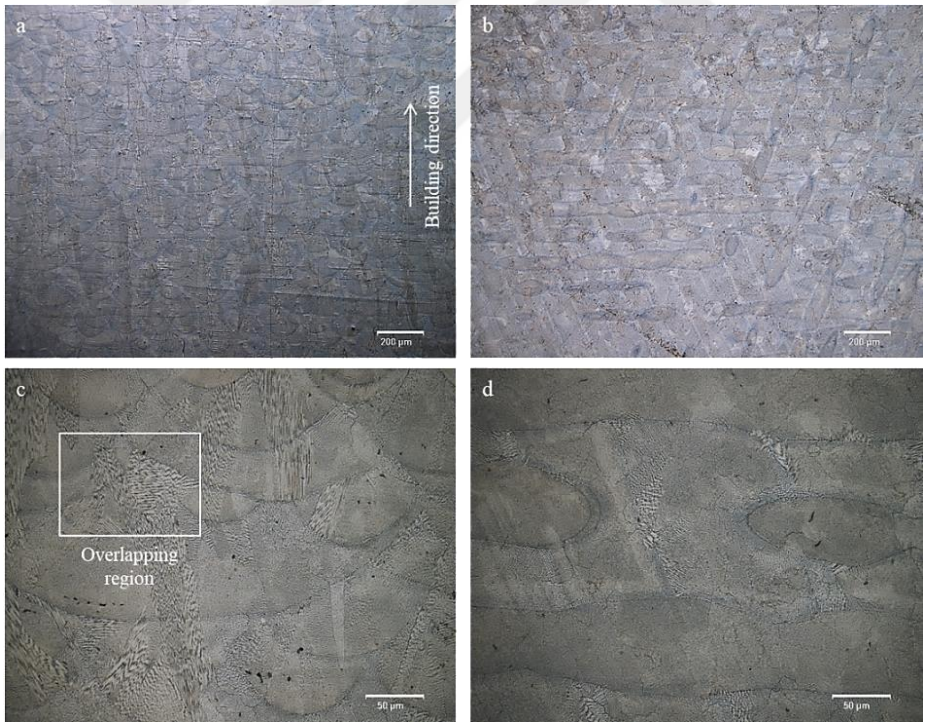

Figure 4.2. Microstructure of the as-etched SLM Inconel 718 samples in as-fabricated condition (a) the melt pool morphology showing typical arc-shaped features (lateral view), (b) the laser beam scanning paths (axial view), (c) magnified image of the zone pointed by white rectangles in (a) and (d) magnified image of the laser scanning paths shown in (b).

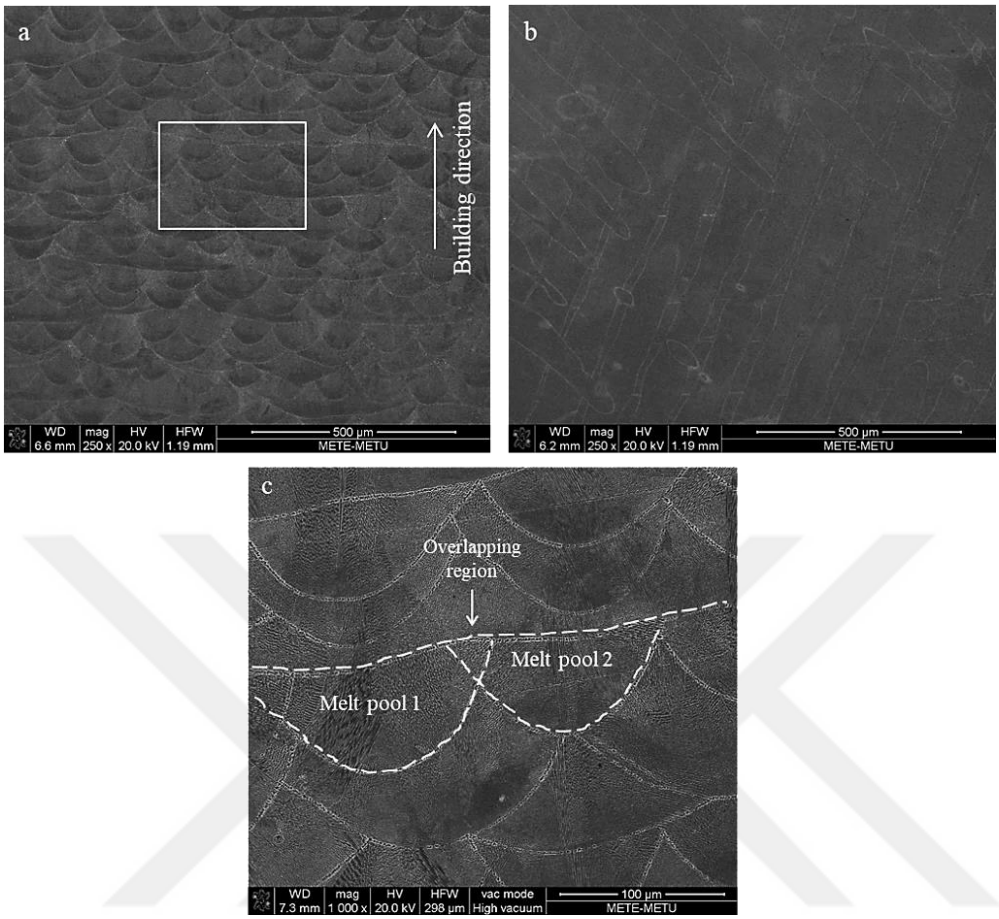

Figure 4.3. SEM images of SLM processed Inconel 718 samples in as-fabricated condition (a) horizontally built, lateral view, (b) vertically built, axial view and (c) magnified image of the zone pointed out by the white rectangle in (a).

The microstructure of the melt pools is highly influenced by the process parameters and scanning strategy. During the SLM process, some overlapping regions can occur both in horizontal and vertical planes with respect to the building direction (Figure 4.2(c-d) and Figure 4.3(c)). This can be explained by the re-melting of the previously solidified layers due to the high laser beam energy. The steep thermal gradient generated in the overlapping regions provides strong bonding interaction between the deposited layers, resulting in formation of more dense structure [59,81]. Mostafa et al. found that the shape of the melt pools in the produced sample was different in the upper (i.e. flat boundaries in a layered fashion) and lower sections of the part [59]. The schematic illustrations of overlapping for both

building directions are also given in Figure 4.4. Horizontal overlapping observed in the as-fabricated samples in the present study are emphasized in Figure 4.3(c).

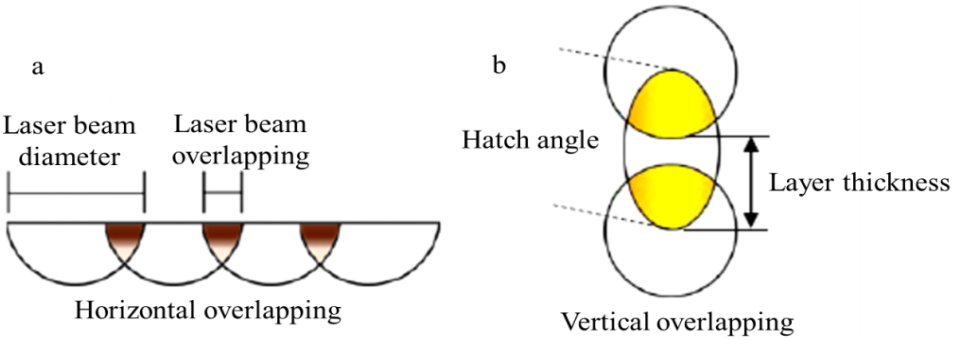

Figure 4.4. Illustration of overlapping regions (a) horizontal and (b) vertical [59].

SEM images in Figure 4.5 represent the detailed microstructure of the as-fabricated sample. A very fine cellular/columnar microstructure was formed within the melt pool morphology. The magnified view in Figure 4.5(b) demonstrates the columnar dendrites with an average dendrite arm spacing of ~1.0 μm in the horizontally built sample. Some cellular structures appeared to be equiaxed grains (Figure 4.5(c)) were also observed at the overlapping regions with sizes of approximately 0.8 μm. X. Li et al. reported that the difference between these two types of microstructure is caused by the high cooling rate during the SLM process [22]. These sizes are smaller when compared to other Inconel 718 alloys fabricated by conventional manufacturing methods. D. Zhang et al. showed that the dendritic microstructure of as-fabricated Inconel 718 is relatively finer than that of the casting alloy in which its dendrite arm spacing was measured to be about 45 μm [90].

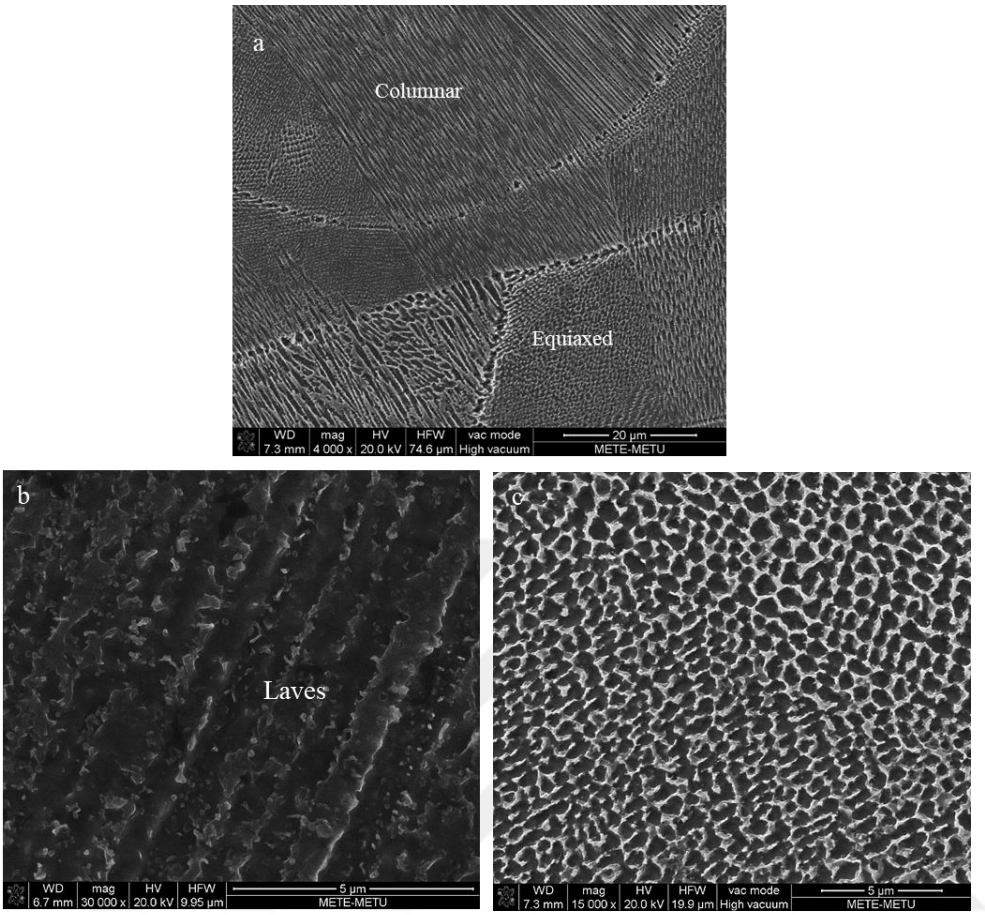

Figure 4.5. SEM micrographs of SLM Inconel 718 samples in as-fabricated condition (a) showing columnar and equiaxed grains within the melt pools, (b) the Laves phase which is embedded in the columnar dendrite and (c) the equiaxed sub-grain which is formed in the overlapping region.

Further details of the as-fabricated samples reveal that irregularly-shaped small particles with a few microns in size are embedded along the interdendritic regions (Figure 4.5(b)). As mentioned earlier, the rapid solidification during SLM process causes segregation of some elements (Nb, Mo and Ti) and leads to the formation of non-equilibrium phases such as Laves phase and MC-type carbides. The white particles seen in Figure 4.5(b, c) were identified as the Nb-rich Laves phase (~1-2µm) according to the EDS analysis given in Table 4.3. It is generally accepted that the Laves phase adversely affects the mechanical properties of the alloy, in particular fracture toughness as well as fatigue and creep properties. This phase

serves as nucleation sites for crack initiation and propagation as well as the formation of microvoids. Additionally, it consumes the available Nb from the matrix which restrains the formation of the strengthening γ″ phases [58,91]. W. Huang, et al. observed that brittle Laves phases are formed in the interdendritic region with a chain-like morphology that must be dissolved in the following heat treatment processes [47].

Table 4.3. EDS analysis of the Laves phase formed in the Inconel 718 alloy matrix.

	Elements (in wt. %)							
	Ni	**Cr**	**Fe**	**Nb**	**Mo**	**Ti**	**Al**	**Co**
Laves	14.20	4.72	4.91	60.56	5.61	8.53	0.35	0.11
Matrix	51.74	19.00	17.71	5.35	4.00	1.06	0.84	0.44

Figure 4.6 represents the XRD pattern of the starting Inconel 718 powders as well as as-fabricated samples built both in horizontal and vertical directions. The XRD patterns revealed the presence of γ″, γ′ and FCC-γ phases for all conditions based on the information about the peaks identified in previous studies in the literature [22,92]. However, it is difficult to differentiate the peaks of γ″ and γ′ phases from that of the matrix phase, since their peaks are overlapping. No other peaks including MC-type carbides or δ phase were observed in the results. For the as-fabricated samples, it can be seen that the dendritic structures illustrate a dominant texture along the (200) plane whereas the powder exhibited strong (111) peaks. This may be related to the formation of strengthening phases which may promote variation in the grain orientation during the fabrication process.

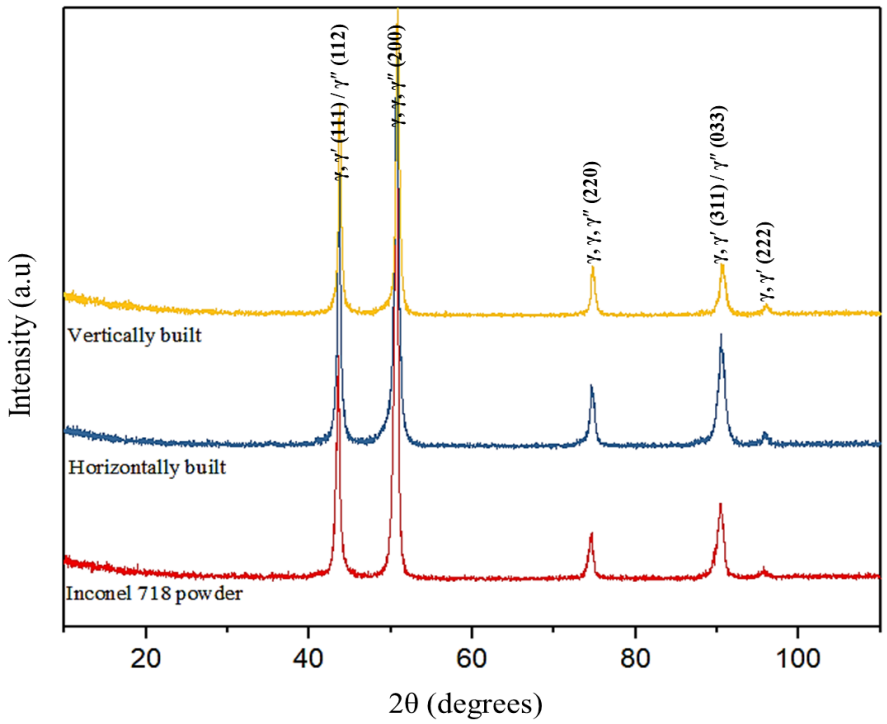

Figure 4.6. XRD pattern of the starting Inconel 718 powder as well as horizontally and vertically built samples.

4.1.2 Heat Treated Inconel 718 Alloy Produced by SLM

Manufacturing of the Inconel 718 alloy using conventional production techniques is very challenging because of its low plasticity and high strain hardening rate, especially for components with complicated geometries. Selective laser melting (SLM) method enables the production of any complex shape of functional parts with high dimensional accuracy. Over the past few years, near full dense and homogeneous Inconel 718 materials have been successfully manufactured using SLM technology. Many researchers have studied on the optimization of the process parameters and the properties of the alloy [44,93]. However, SLM process causes the development of undesired microstructure in as-fabricated components owing to the rapid solidification rate and steep temperature gradient. As mentioned before, related negative aspects encountered during SLM processing can be described as the formation of non-equilibrium phases, segregation of refractory elements,

directional grain growth, high residual stresses or formation of defects such as cracks, pores, etc. [80,81]. Additionally, microstructure of the SLM-processed Inconel 718 different from those of wrought and casting materials significantly influences the components' dimensional and geometrical accuracy as well as their mechanical properties. For this reason, post-processing heat treatments are essential to minimize these negative aspects in the as-fabricated components and to alter their mechanical performance.

Inconel 718 alloys are mainly designed to overcome the extreme service conditions including corrosive environment at high stress and/or temperature. Therefore, their favorable microstructure consists of the stable γ matrix strengthened by coherent and dispersive particles of the γ″ or γ′ phases and other secondary phases. Therefore, the main purpose is to optimize precisely the morphology, size and volume fractions of these phases as well as aging treatment parameters to achieve optimal mechanical performance.

In this study, two types of Inconel 718 alloys (i.e. horizontally and vertically built as illustrated in Figure 3.3) were fabricated by SLM method. After the manufacturing procedure, all samples were first solutionized at 1040 ºC for 2 hours followed by air cooling to increase the dissolution of the Laves phase and carbides in the matrix. Subsequently, one step aging treatment was carried out at 700 ºC for different soaking times to form finely distributed strengthening precipitates. Various heat treatment conditions (as summarized in Table 3.2) have been applied to investigate the microstructure and mechanical behavior of the samples. Although the standard solution treatment is carried out at 980 ºC for wrought and cast alloys, many studies were performed to determine the most convenient solutionizing temperature for SLM-produced alloys. It was reported that carbides and brittle Laves phases remain undissolved at 980 ºC. Increasing the solution treatment temperature promotes the dissolution of these undesirable phases. Therefore, the aim of this study is to optimize heat treatment processes for the Inconel 718 alloy

produced by SLM method to obtain mechanical properties close to those of wrought materials.

SEM images of the grain structures of the samples built in horizontal and vertical directions and subsequently heat treated under different conditions are given in Figure 4.7 and Figure 4.8, respectively. Compared to the grain structures of as-fabricated samples in Figure 4.2 and Figure 4.3, arc-shaped structure seem to have disappeared and converted into a mixture of columnar and/or equiaxed grains for all heat treatment conditions. In the literature, the reason for this type of modification has been attributed to the presence of primary carbides and secondary phases dispersed in the matrix, which may lead to limitation in grain boundary motion [55].

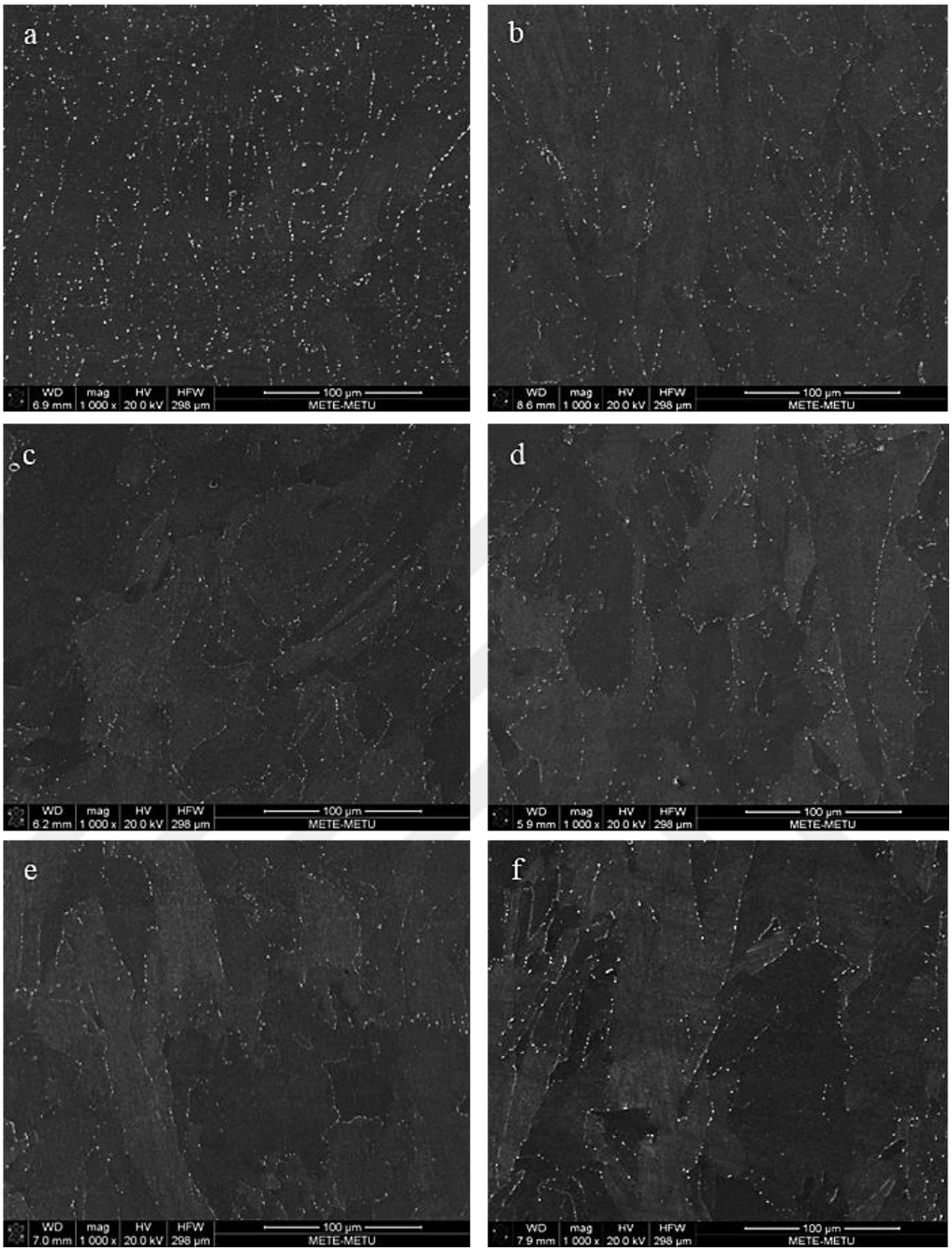

Figure 4.7. Lateral microstructures of horizontally built SLM Inconel 718 samples in different heat treated conditions (a) PHT-5h, (b) PHT-8h, (c) SHT, (d) PHT-16h, (e) PHT-28h and (f) PHT-34h.

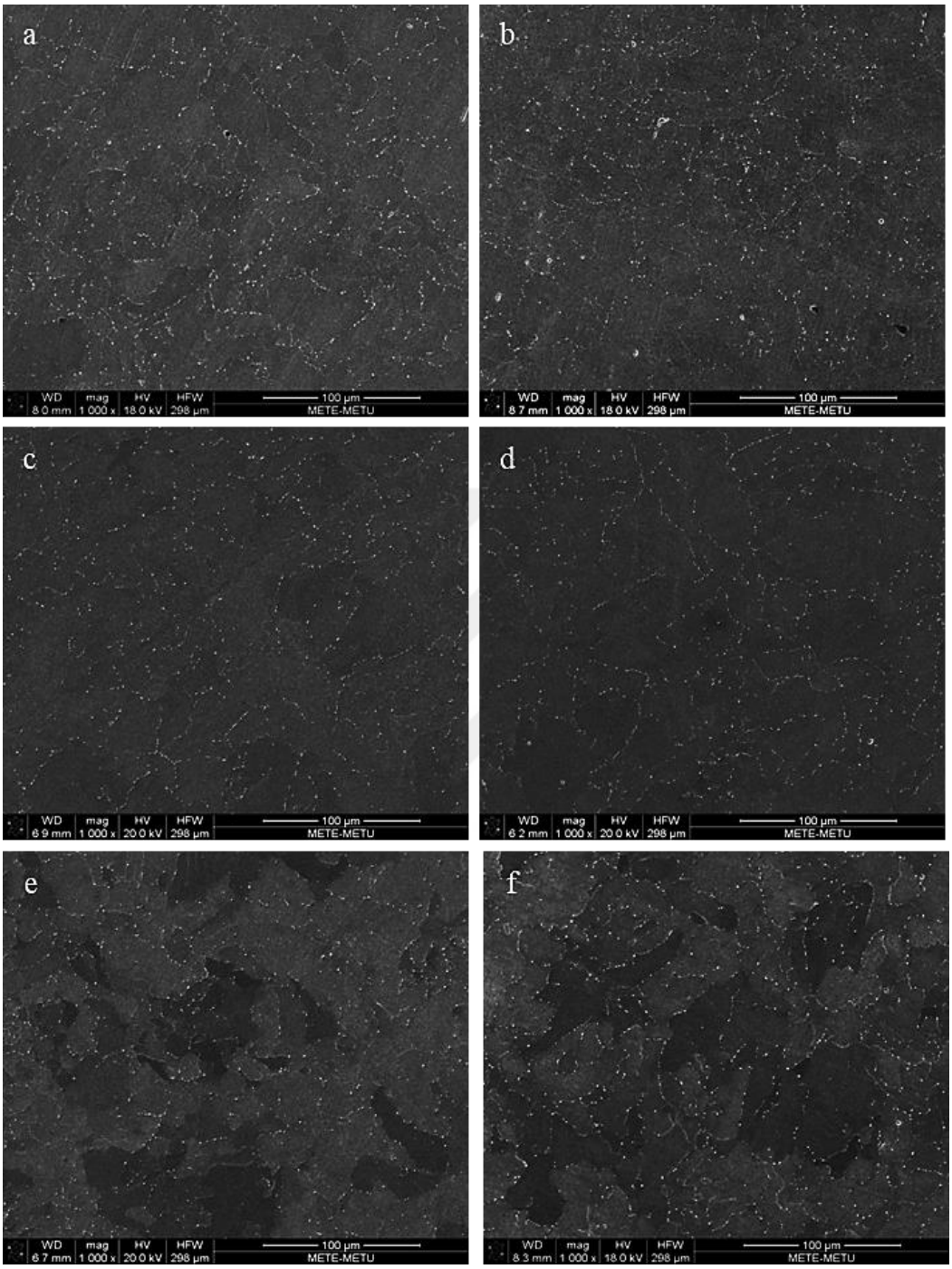

Figure 4.8. Axial microstructures of vertically built SLM Inconel 718 samples in different heat treated conditions (a) PHT-5h, (b) PHT-8h, (c) SHT, (d) PHT-16h, (e) PHT-28h and (f) PHT-34h.

For all heat treatment conditions, Laves particles 0.2 and 1 μm in size were observed to disperse in the grain interiors and along the grain boundaries. The corresponding elemental mapping analysis demonstrated that the Laves phase is enriched in Nb, Mo and Ti elements, while the dendritic regions are enriched in Ni, Fe and Cr elements as shown in Figure 4.9. It should be noted that the dissolution of the Laves phase by heat treatment processes is an important consideration to release the Nb element which promotes the formation of the γ″ phase in the alloy matrix. However, it is also known that it is difficult to dissolve the Laves phase due to the low solubility of the large Nb and Mo atoms [57]. Similar to the results obtained in the literature, large amount of undissolved Laves particles were observed after all heat treatment conditions in the present study.

S. Raghavan et al. examined the effect of different heat treatments on the properties of the Inconel 718 alloy produced by SLM by varying the solution treatment temperature from 1040 to 1200 ºC. They found that the dissolution of the Laves phase increased by increasing the process temperature. However, some Laves phase remained along the grain boundaries even at the highest solutionizing temperature [79].

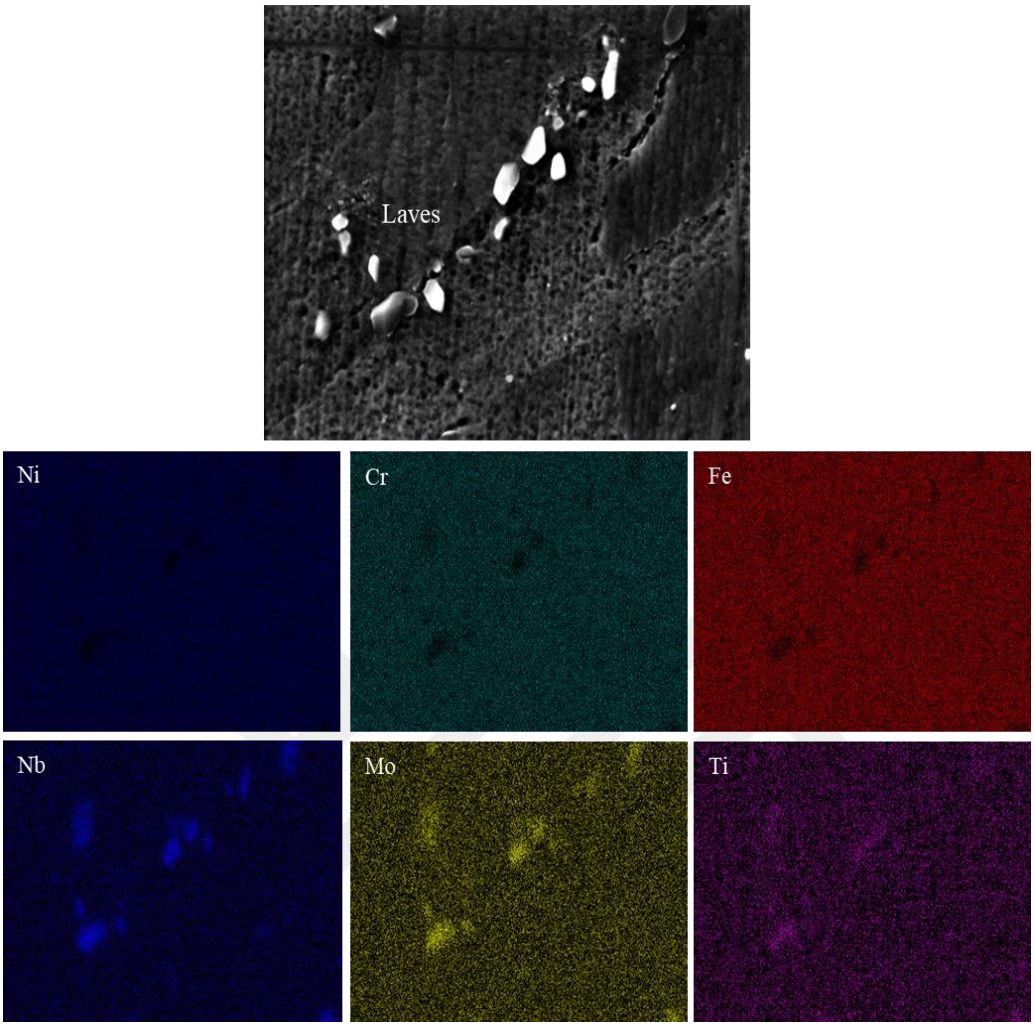

Figure 4.9. EDS elemental mapping of the heat treated Inconel 718 in SHT condition; the elemental maps of Ni, Fe, Nb, Mo and Ti, respectively.

Figure 4.10 reveals the detailed morphologies of the phases formed in the heat treated Inconel 718 samples. It is seen that nano-sized precipitates which correspond to γ″ or γ′ phases are homogeneously distributed in the matrix, except for the sample heat treated using PHT-5h condition (Figure 4.10(a)). Microstructural observations revealed that the aging process at 700 ºC for 5 h was not sufficient for complete formation of the strengthening phases. Thus, some γ″ and/or γ′ phases ~20 nm in size were randomly distributed within the matrix for the PTH-5h condition. It has been observed that increase in soaking time during the aging treatment causes an increase in the average size of the precipitates. The size

of the strengthening phases was measured between 20 and 30 nm for PHT-8h, SHT and PTH-16h conditions. Moreover, the γ″ and/or γ′ phases, approximately 50 nm in size, are uniformly distributed in the matrix for PHT-28h and PTH-34h conditions. Also, coalescence of the phases was observed when the alloys were treated using the PHT-28h and PHT-34h conditions shown in Figures 4.10(e) and (f), respectively.

According to the transformation-time-temperature (TTT) diagram of the Inconel 718 alloy system [14], the metastable γ″ phase can transform to δ phase during aging treatment within 650-980 ºC in durations more than 10 h. Under these conditions, some disc-like γ″ precipitates dissolved and acicular-shaped δ phase particles (~30 nm thick and ~200 nm length) formed along the grain boundaries for SHT and PHT-16 h conditions. As time increases at a given temperature, the size and amount of the δ phase increased. For the PHT-28 h and PHT-34 h conditions, δ phase with a length of about 450 nm also appeared in the matrix.

It has been reported that precipitation of large amounts of the δ phase consumes Nb element, which results in the depletion of the γ″ particles. In addition, the morphology of the δ phase (i.e. sharp edges of the acicular-shaped particles) can act as crack initiation and propagation sites at elevated temperatures. Therefore, this phase is not preferred in the microstructure, as it causes a reduction in the mechanical properties of the Inconel 718 alloy. However, some researchers agreed on the fact that appropriate amount of δ phase with globular morphology can limit the grain boundary sliding, refine the grain size, and thus alter the tensile or fatigue properties and creep resistance. D. Zhang et al. reported that the needle-like δ particles formed incoherently along the grain boundaries as well as in the grain interior when the standard heat treatment procedure was applied to wrought Inconel 718 [32]. D. Deng et al. studied the effect of heat treatment on the microstructural evolution and mechanical behavior of the Inconel 718 alloy, where they observed that large δ particles lead to formation of voids in the matrix providing easy crack propagation sites [45].

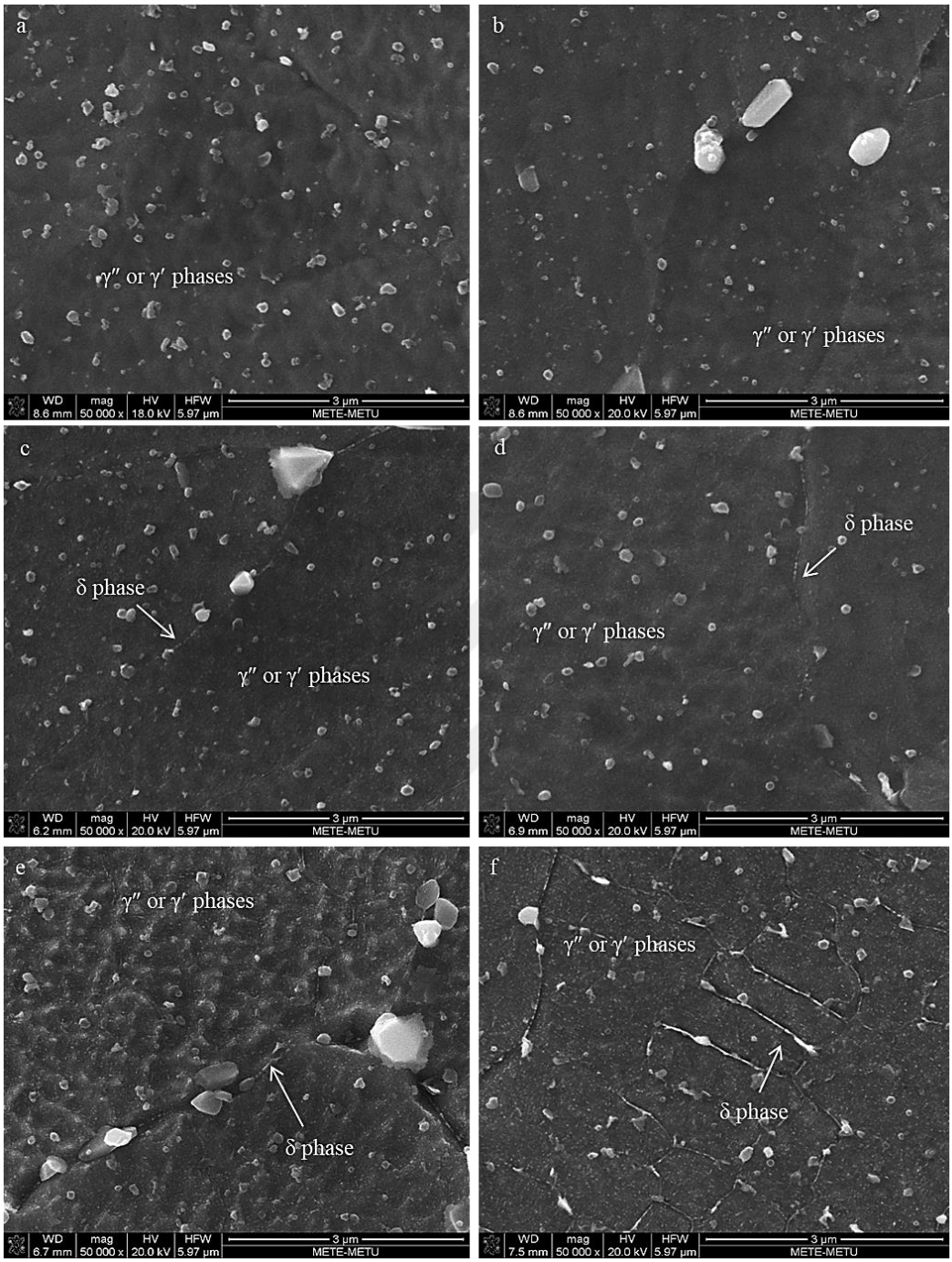

Figure 4.10. SEM images of the strengthening γ″ and/or γ′ phases together with δ phases (a) PHT-5h, (b) PHT-8h, (c) SHT, (d) PHT-16h, (e) PHT-28h and (f) PHT-34h.

A few irregular-shaped primary MC type carbides of size ~5 μm were also detected for all heat treatment conditions, which were TiC carbides as verified by EDS and XRD analyses. As mentioned previously, this can be associated with the high stability of the primary MC type carbides even at high temperatures. Therefore, the primary carbides formed during SLM process remained undissolved during the heat treatment processes. The points numbered in Figure 4.11(b) correspond to those in Table 4.4, which gives the results of the EDS analysis of the different phases formed in the matrix. EDS results revealed that the white particles (point 1) which correspond to the Laves phase are enriched in Nb (29.99 wt.%), Mo (4.55 wt.%) and Ti (3.53 wt.%) elements, and the primary MC carbide formed in the matrix (point 2) is enriched in Ti (74.73 wt.%) and Nb (17.54 wt.%). The chemical composition of the matrix (point 3) is close to that of Inconel 718 powder's (Table 3.1) used in the production of the alloy. Additionally, some block-shaped secondary MC type carbides enriched in Nb were detected along the grain boundaries (Table 4.5). It is known that the error of EDS analysis raises when small particles are observed depending on the volumetric interaction between the phases and the surrounding matrix. Therefore, EDS analysis was unable to detect the elements present in the γ′, γ″ and δ phases much smaller in size compared to the above mentioned ones.

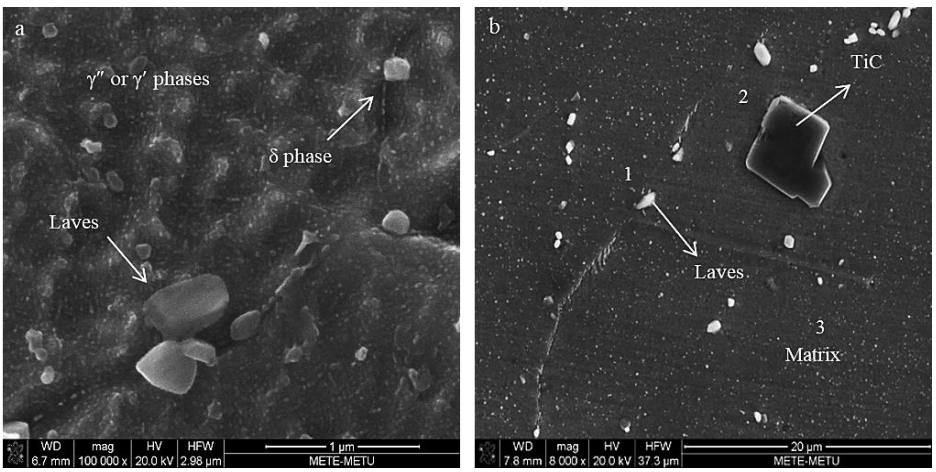

Figure 4.11. SEM images of (a) γ′, γ″ and δ phases and (b) Laves phase and primary TiC particles formed within the matrix in PHT-28h condition.

Table 4.4. EDS analysis of the Laves phase, the primary MC type carbide and the matrix of the Inconel 718 alloy shown as points 1, 2 and 3 in Figure 4.11(b), respectively.

	Elements (in wt.%)						
Points	**Ni**	**Cr**	**Fe**	**Nb**	**Mo**	**Ti**	**Al**
1. Laves	34.97	13.62	12.56	29.99	4.55	3.53	0.28
2. P. Carbides	3.04	1.91	1.05	17.54	1.42	74.73	0.31
3. Matrix	51.06	19.01	17.71	6.21	4.01	1.06	0.84

Table 4.5. EDS analysis of the secondary MC type carbides precipitated on the grain boundaries in heat treated Inconel 718 alloy.

	Elements (in wt.%)							
Points	**Ni**	**Cr**	**Fe**	**Nb**	**Mo**	**Ti**	**Al**	**C**
S. Carbides	12.55	5.72	4.91	59.56	4.11	7.03	0.35	5.74

XRD patterns of the samples built in horizontal and vertical directions heat treated under different conditions are given in Figure 4.12 and Figure 4.13, respectively. Three main peaks were determined in the heat treated samples as FCC-γ matrix and strengthening γ″ and γ′ phases for all conditions. Depending on the building direction, the intensities of the peaks changed, yet the dominant texture was the same for both conditions. All heat treated samples exhibited a dominant texture in the (200) direction similar to as-fabricated samples, while the sample heat treated using PHT-34 h condition showed a strong texture in the (111) direction.

A new peak at around 45-46° corresponding to the orthorhombic δ phase was attributed to the (201) plane in samples heat treated using SHT, PHT-16h, PHT-28h and PHT-34h conditions, which is also in good correlation with the SEM analysis . It was mentioned that the γ″ phase converts to the δ phase during aging treatment within 650-980 ºC when the soaking time exceeds 10 h. Additionally, a small peak present at around 35° corresponds to the (111) plane of the primary MC

type carbide [38]. XRD method generally fails to identify the phases with an amount less than 5 vol.% of the sample, thus these to peaks possess very small intensities. For this reason, another XRD analysis was performed for PHT-34h condition with a fixed scan speed of 0.1°/min to determine the secondary MC type carbides and δ phase formed as a result of heat treatments (Figure 4.12). However, the peaks of the phases still did not appear clearly according to the results obtained from the XRD analysis at slower scanning rate (inset of Figure 4.12).

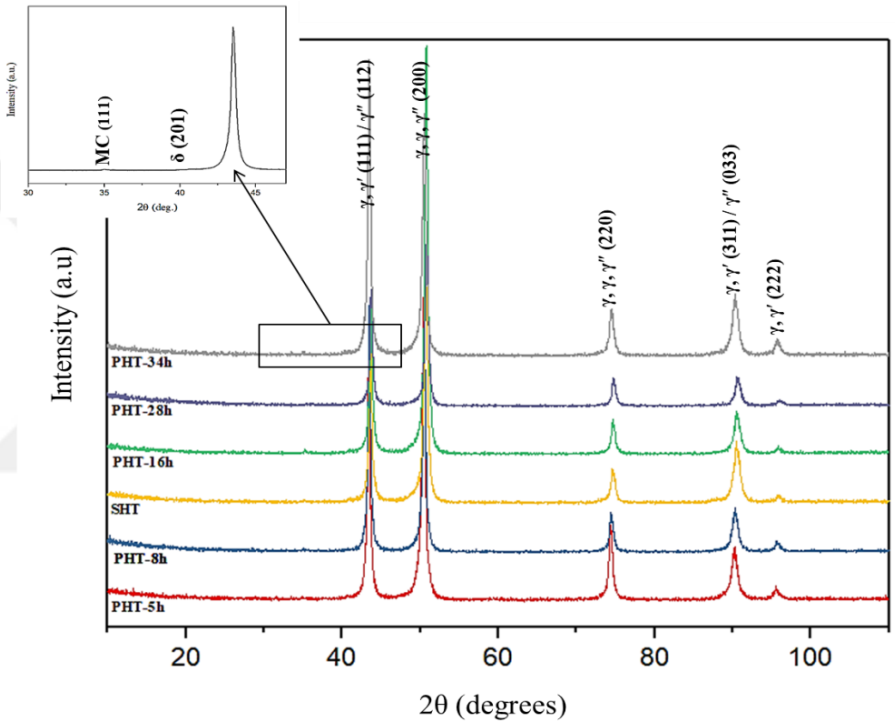

Figure 4.12. XRD pattern of horizontally built SLM Inconel 718 samples in different heat treated conditions.

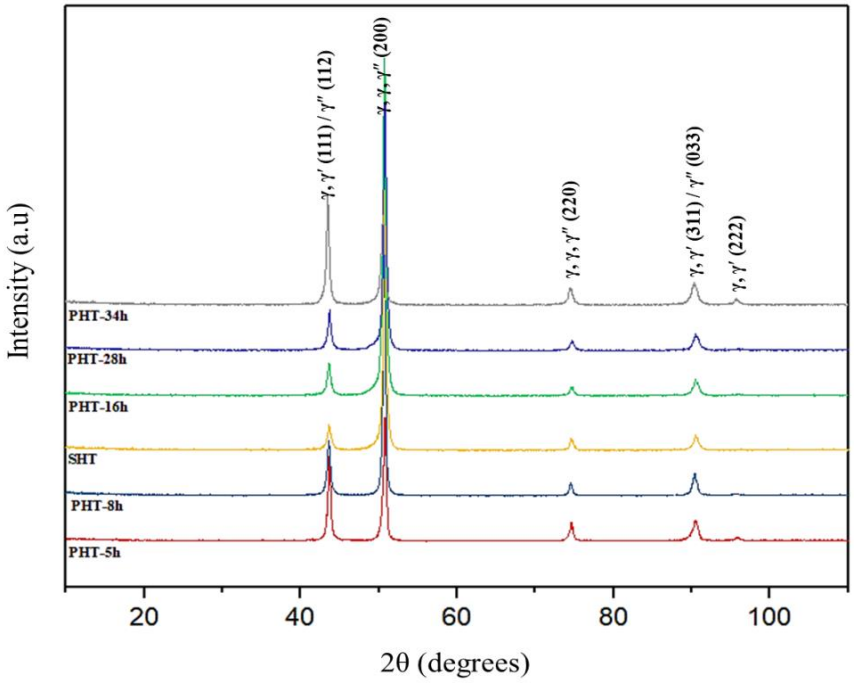

Figure 4.13. XRD pattern of vertically built SLM Inconel 718 samples in different heat treated conditions.

4.2 Texture Evolution in As-Fabricated and Heat Treated Inconel 718 Alloys

4.2.1 As-Fabricated Inconel 718 Alloy

Figure 4.14 and Figure 4.15 illustrate the EBSD analysis results of the as-fabricated SLM Inconel 718 samples built in horizontal and vertical directions, respectively. The inverse pole figure (IPF) color mappings were conducted on the corresponding EBSD data to determine the crystallographic orientations. The colors in the IPF maps show the crystal orientations of the grains in the alloy, where the normal planes represented by red, green and blue colors correspond to (001), (101) and (111) planes which are parallel to the building direction.

The structure in the horizontally built sample illustrated columnar grains elongated along the building direction which corresponds to the direction of the dominant heat flux during the SLM process, Figure 4.14(a) [81]. In contrast, the equiaxed grains with sizes of approximately 9.6 ± 8.8 μm were observed in the vertically built sample along the axial direction as illustrated Figure 4.15(a). The inverse pole figures (Figure 4.14(b) and Figure 4.15(b)) demonstrated that the horizontally built sample had a nearly random orientation with the maximum intensity value of 4.713 while the texture of the vertically built sample concentrated with the maximum intensity value of 3.160 in (001) plane. However, the grains in the horizontally built sample in the lateral direction seem to possess a vague tendency to align along to (001) and (111) planes. It should be noted that this texture along the building direction (i.e. (001) plane) is coinciding with the maximum heat flow, and hence easy grain growth direction at the melt pool boundary.

Low angle grain boundaries (LAGBs) were predominant at both horizontally and vertically built samples, especially, having misorientation angles in the of range 0-5°. The number fraction of LAGBs misorientation angles of the horizontally and vertically built samples were 0.73 and 0.69, respectively. On the other hand, the number fraction of the HAGBs showed a slight increase for vertically built samples. For the SLM process, these LAGBs consist of a large number of dislocations to accommodate the large residual thermal strains [52].

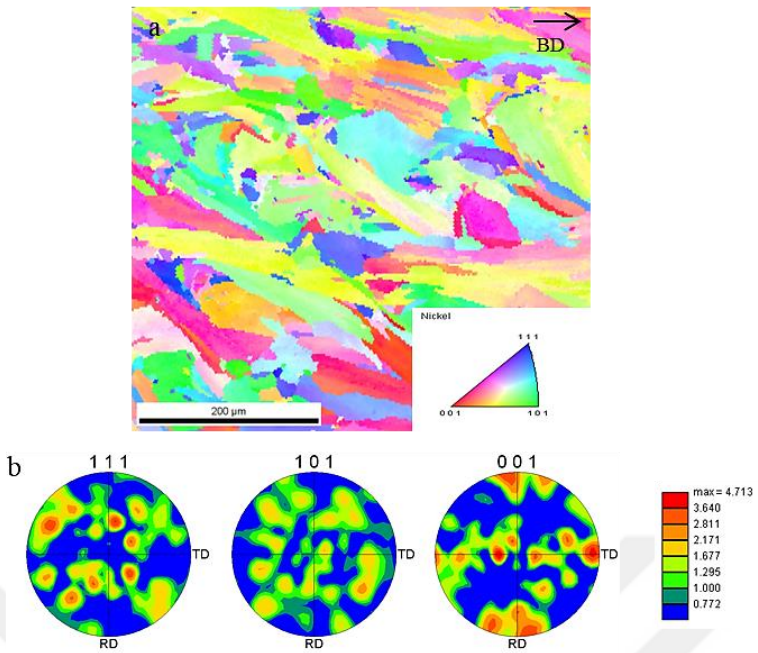

Figure 4.14. EBSD map of the horizontally built as-fabricated Inconel 718 alloy (a) IPF color mapping of columnar grains and (b) pole figures demonstrating alloy texture.

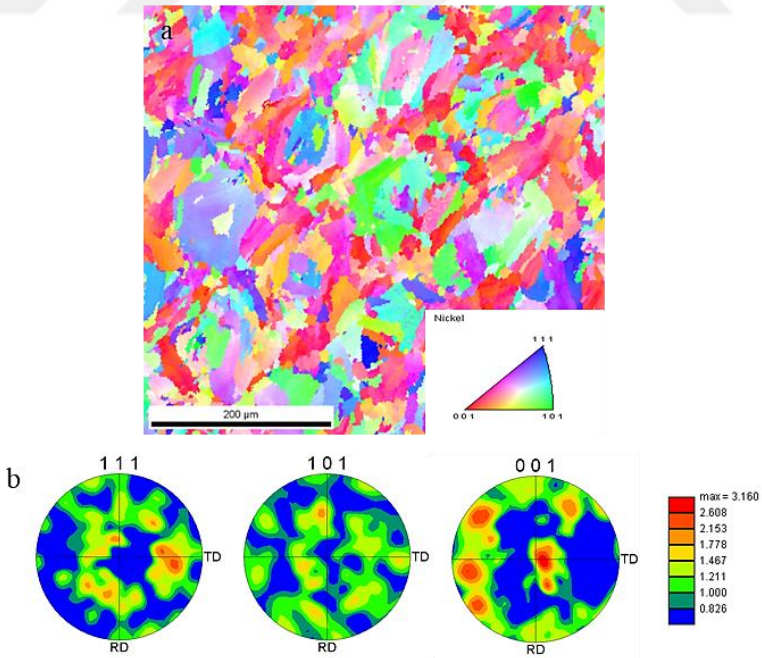

Figure 4.15. EBSD map of the vertically built as-fabricated Inconel 718 alloy (a) IPF color mapping of columnar grains (b) pole figures demonstrating alloy texture.

4.2.2 Heat Treated Inconel 718 Alloy

EBSD analysis and corresponding inverse pole figure (IPF) color mappings of the heat treated samples shown in Figures 4.16-27, where the effect of the various heat treatments on the grain structures were more clearly observed. As can be seen, the heat treatment processes did not significantly alter the texture of the samples for both building directions. While the structure in the horizontally built sample contained columnar grains elongated along the building direction, the equiaxed grains were observed in the vertical directions as similar to the texture of as-fabricated samples.

For PHT-5h condition (Figure 4.16(a) and Figure 4.17(a)), the texture in the horizontally built sample illustrated columnar grains elongated along the building direction whereas the equiaxed grains with sizes of approximately 11.9 ± 10.2 μm were observed in the vertical directions. The IPFs of the horizontally built sample demonstrated a nearly random orientation (mainly (001) and less frequently (111) planes) with the maximum intensity value of 5.115 while the vertically built samples had a dominant texture on (001) plane with the maximum intensity value of 4.396 as given in Figure 4.16(b) and Figure 4.17(b), respectively.

For PHT-8h condition, the microstructure in the horizontally built sample (Figure 4.18(a)) showed again columnar grains elongated along the building direction. The equiaxed grains with sizes of approximately 10.7 ± 9.5 μm were examined in the vertically built sample (Figure 4.19(a)) which showed a slight difference from the PHT-5h condition. According to IPFs, the texture of the horizontally built sample (Figure 4.18(b)) concentrated with the maximum intensity value of 3.803 in (001) plane. Additional textures were also observed on the (111) and (101) planes. The vertically built samples had a strong texture on (001) plane with the maximum intensity value of 3.775 as demonstrated in Figure 4.19(b).

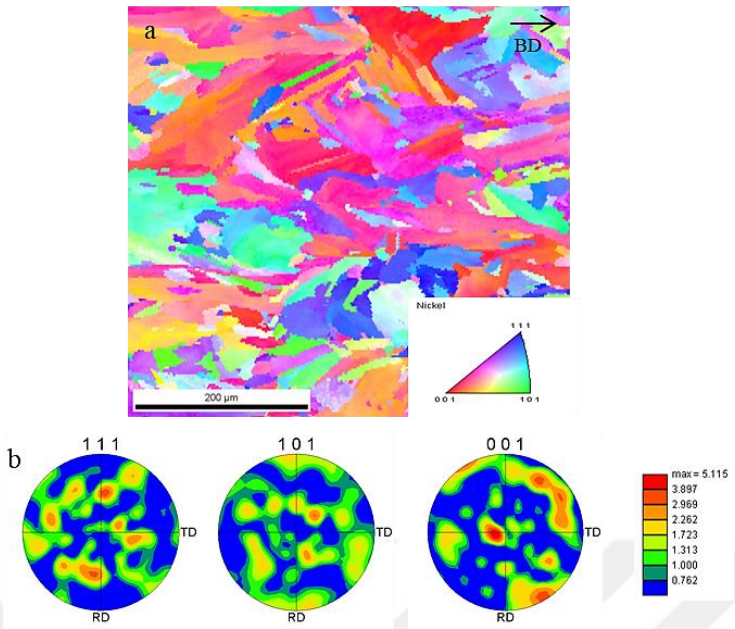

Figure 4.16. EBSD maps of the horizontally built heat treated Inconel 718 alloy in PHT-5h condition (a) IPF color mapping of columnar grains and (b) pole figures demonstrating alloy texture.

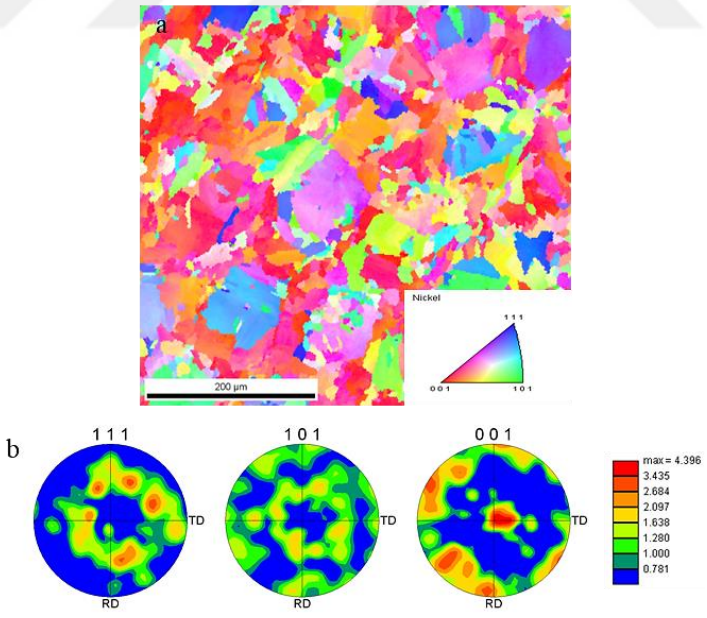

Figure 4.17. EBSD maps for the vertically built heat treated Inconel 718 alloy in PHT-5h condition (a) IPF color mapping of columnar grains and (b) pole figures demonstrating alloy texture.

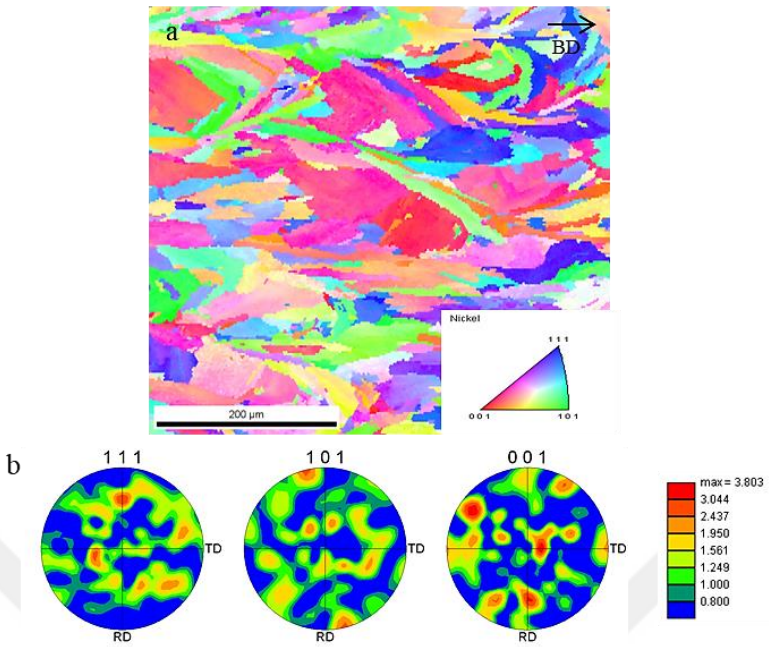

Figure 4.18. EBSD maps of the horizontally built heat treated Inconel 718 alloy in PHT-8h condition (a) IPF color mapping of columnar grains and (b) pole figures demonstrating alloy texture.

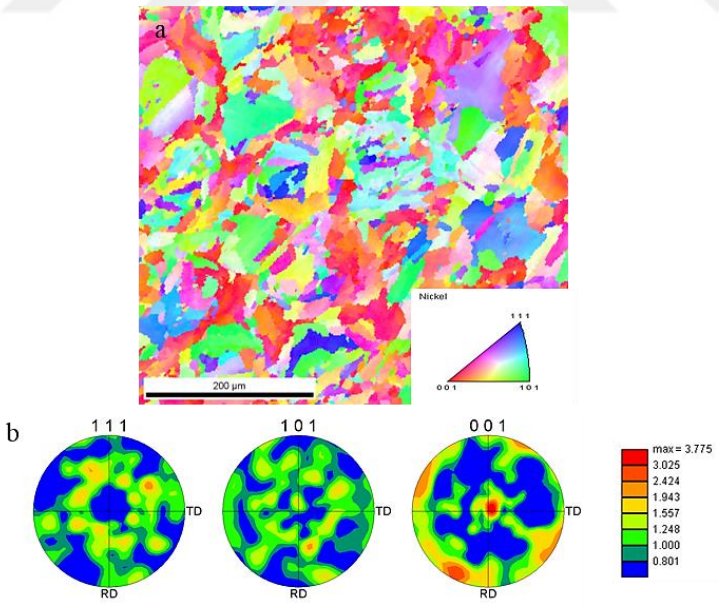

Figure 4.19. EBSD maps of the vertically built heat treated Inconel 718 alloy in PHT-8h condition (a) IPF color mapping of columnar grains and (b) pole figures demonstrating alloy texture.

Figure 4.20 (a) demonstrated that the width of the columnar grains in the horizontally built sample showed an increase when the SHT condition was performed. The size of the equiaxed grains observed in the vertically built sample (Figure 4.21 (a)) was measured by about 11.1 ± 9.8 μm. IPFs results showed that the texture of the horizontally built sample (Figure 4.20 (b)) concentrated with the maximum intensity value of 4.787 in (001). Furthermore, the columnar grains seem to possess a slight tendency to align along to (111) plane. The texture of the vertically built sample as shown in Figure 4.21 (b) concentrated with the maximum intensity value of 3.393 in (001).

For PHT-16h condition, the coarser columnar structure in the horizontally built sample can be seen clearly in the EBSD maps (Figure 4.22(a)). The equiaxed grains with sizes of about 12.1 ± 10.4 μm were observed in the vertically built sample (Figure 4.23(a)). The IPFs of the horizontally built sample demonstrated a nearly random orientation with the maximum intensity value of 6.528 (Figure 4.22(b)). It means that the texture has a tendency to align along to (001), (101) and (111) planes. In contrast, the texture of the vertically built sample (Figure 4.23(b)) concentrated with the maximum intensity value of 5.101 in (001) plane.

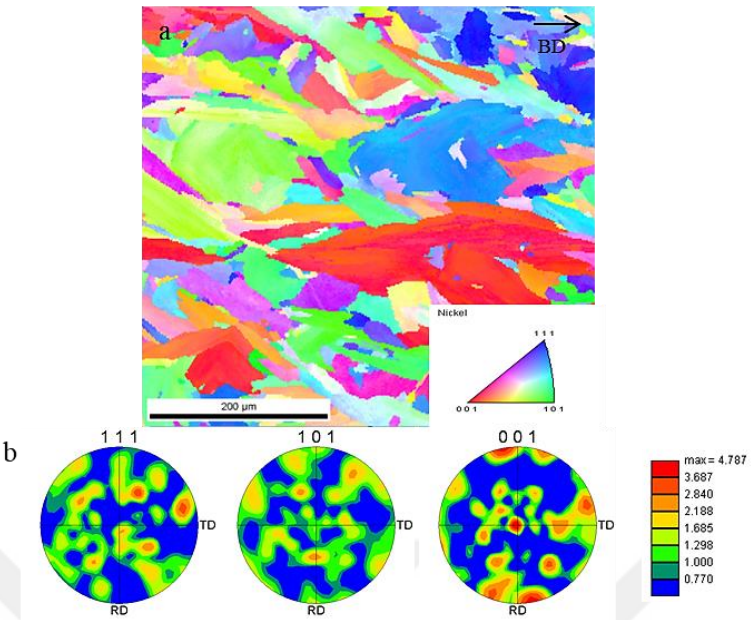

Figure 4.20. EBSD maps of the horizontally built heat treated Inconel 718 alloy in SHT condition (a) IPF color mapping of columnar grains and (b) pole figures demonstrating alloy texture.

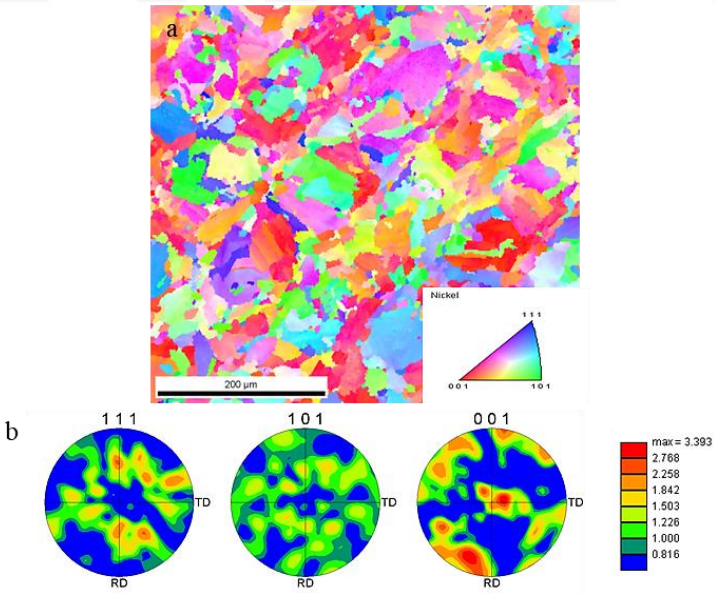

Figure 4.21. EBSD maps of the vertically built heat treated Inconel 718 alloy in SHT condition (a) IPF color mapping of columnar grains and (b) pole figures demonstrating alloy texture.

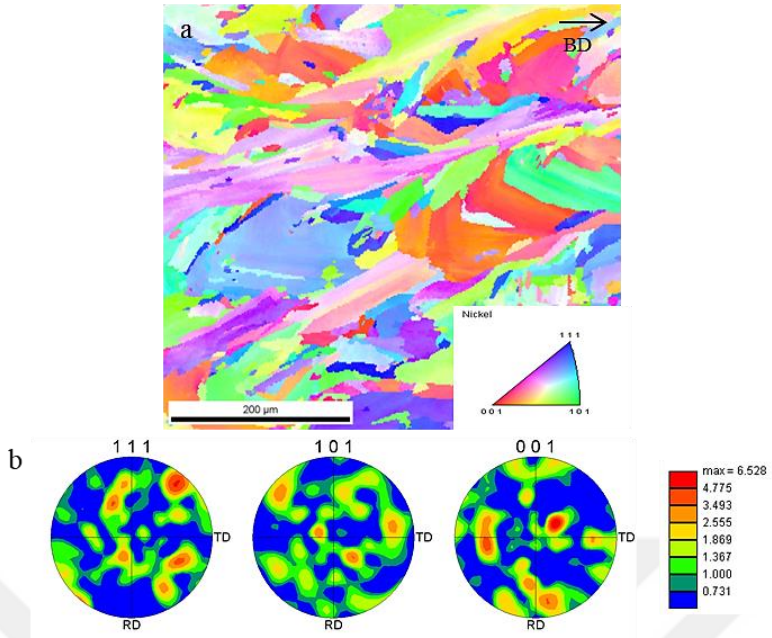

Figure 4.22. EBSD maps of the horizontally built heat treated Inconel 718 alloy in PHT-16h condition (a) IPF color mapping of columnar grains and (b) pole figures demonstrating alloy texture.

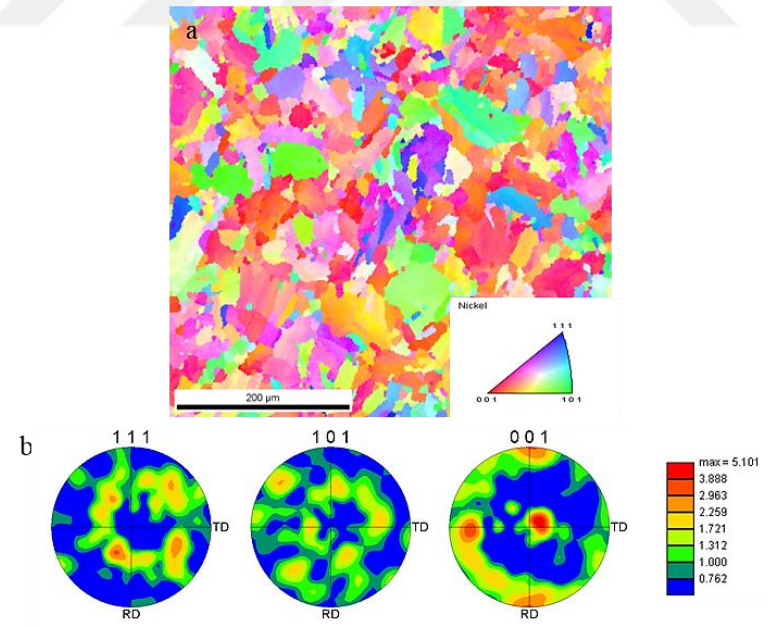

Figure 4.23. EBSD maps of the vertically built heat treated Inconel 718 alloy in PHT-16h condition (a) IPF color mapping of columnar grains and (b) pole figures demonstrating alloy texture.

As can be observed in Figure 4.24 (a), the coarser columnar grains in the horizontally built sample can be seen clearly for PHT-28h condition. The size of the equiaxed structures in the vertically built sample (Figure 4.25 (a)) was measured approximately 11.4 ± 10.2 μm. When IPFs of the horizontally built sample (Figure 4.24 (b)) were investigated, it was observed that the texture concentrated with the maximum intensity value of 7.216 in (001). Additional textures were also observed on the (111) plane. Otherwise, the texture of the vertically built sample as shown in Figure 4.25 (b) concentrated with the maximum intensity value of 3.306 in (001).

For PHT-34h condition, the structure in the horizontally built sample (Figure 4.26(a)) illustrated again coarse columnar grains elongated along the building direction. The equiaxed grains with sizes of approximately 11.2 ± 9.9 μm were observed in the vertically built sample (Figure 4.27 (a)) which showed a slight difference from the other heat treatment conditions. According to IPFs, the texture of the horizontally built sample (Figure 4.26(b)) concentrated with the maximum intensity value of 3.495 in (001) plane. Additional textures were also observed on the (111) and (101) planes. The vertically built samples had an intense texture on (001) plane with the maximum intensity value of 3.246 (Figure 4.27(b)).

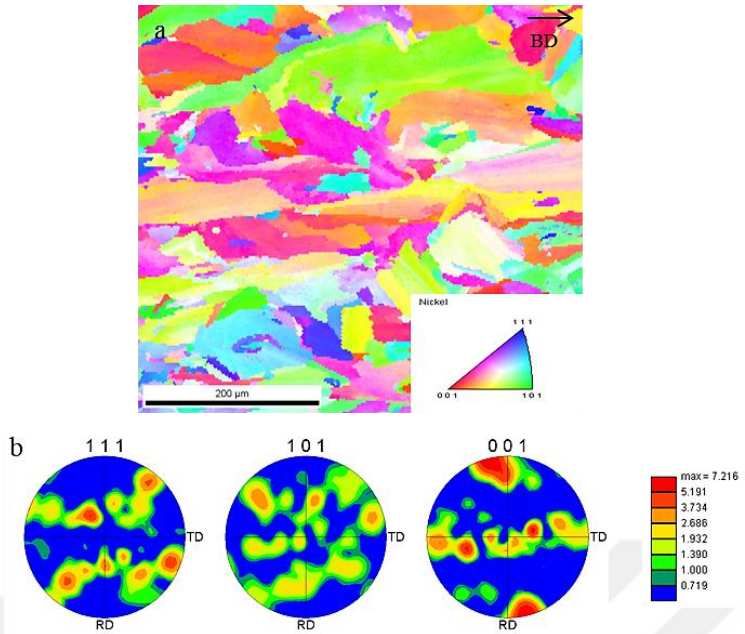

Figure 4.24. EBSD maps of the horizontally built heat treated Inconel 718 alloy in PHT-28h condition (a) IPF color mapping of columnar grains and (b) pole figures demonstrating alloy texture.

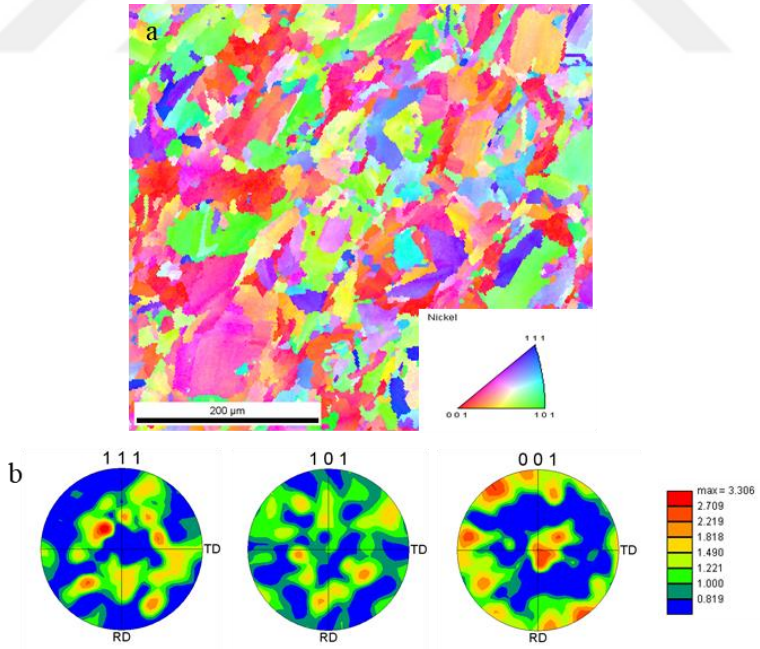

Figure 4.25. EBSD maps of the vertically built heat treated Inconel 718 alloy in PHT-28h condition (a) IPF color mapping of columnar grains and (b) pole figures demonstrating alloy texture.

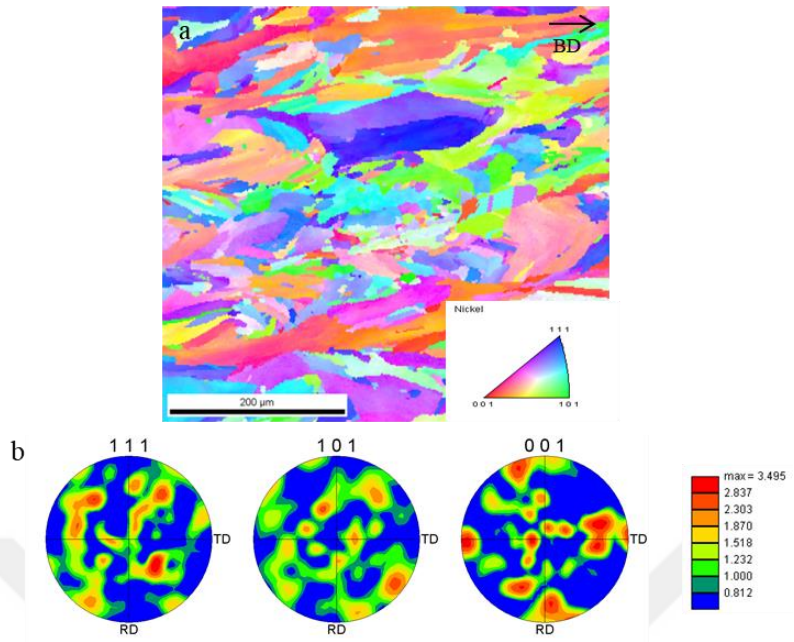

Figure 4.26. EBSD maps of the horizontally built heat treated Inconel 718 alloy in PHT-34h condition (a) IPF color mapping of columnar grains and (b) pole figures demonstrating alloy texture.

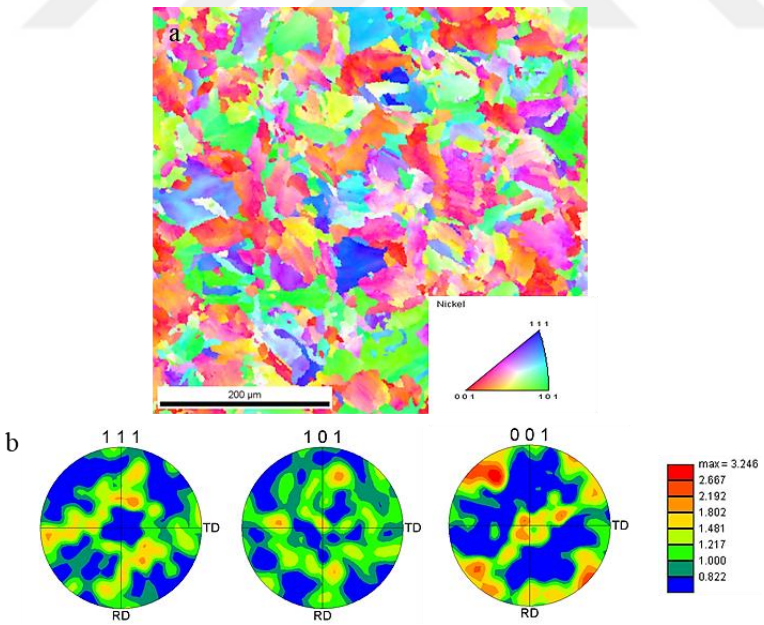

Figure 4.27. EBSD maps of the vertically built heat treated Inconel 718 alloy in PHT-34h condition (a) IPF color mapping of columnar grains and (b) pole figures demonstrating alloy texture.

As a result, the effect of various heat treatments on the texture of the samples for both building directions was discussed in the previous section. It is clearly seen that the applied heat treatments did not significantly change the texture. Only small differences correlated as the soaking time of the aging treatment were observed. The same EBSD results were also reported by D. Deng et al. for the standard heat treatment and homogenization plus double aging processes [45].

The results showed that the average grain size of all vertically built samples was close to that of the as-fabricated sample (i.e. 9.6 ± 8.8 μm), indicating that grain growth was not observed after heat treatment processes. As noted previously, a large amount of Laves particles were observed with a size between 0.2 and 1 μm dispersing in the alloy matrix after all heat treatment conditions. This can be attributed to the fact that the temperature of the solution treatment was insufficient to complete the dissolution of the Laves phases. The studies in the literature showed that the dissolution of the Laves phase increases with increasing solution treatment temperature, although some of the Laves phase remains undissolved even at the highest solutionizing temperature applied (i.e. near the melting temperature of the Laves phase). It can be concluded that the presence of remained Laves phases and carbides along the grain boundaries may contribute to the grain boundary pinning, and thus inhibit grain growth in Inconel 718 alloys.

The number fraction of LAGBs misorientation angle distribution of both horizontally and vertically building directions for all heat treatment conditions (Figure 4.28). The results showed that LAGBs are predominant for all conditions, as similar to the distribution in the as-fabricated samples. Only minor changes in the distribution were observed for different heat treatment processes.

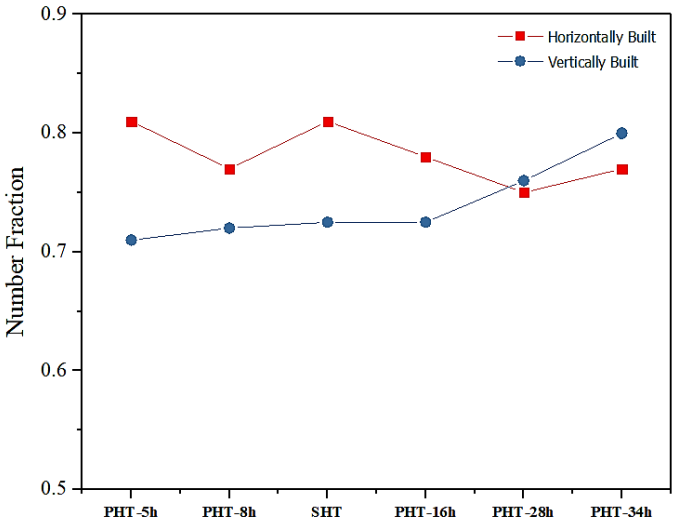

Figure 4.28. Number fraction of LAGBs misorientation angle distributions of SLM Inconel 718 alloys in various heat treated conditions (a) horizontally built and (b) vertically built.

4.3 Mechanical Property Evolution of Heat Treated Inconel 718 Alloy

4.3.1 Microhardness Measurements

Axial and lateral microhardness values of the SLM Inconel 718 samples produced both in horizontal and vertical directions in both as-fabricated and heat treated conditions are given in Figure 4.29. In both samples, there was no significant microhardness fluctuation with respect to the measurement axis where the microhardness of the samples produced by SLM showed an isotropic nature in terms of the hardness. The average microhardness of the as-fabricated sample was measured as 315 HV, which was relatively lower than that of the wrought material (340 HV - AMS 5662) [32]. On the other hand, the value was considerably higher when compared to the cast material (270 HV - AMS 5383) [32]. This may have resulted from the higher cooling rate of the SLM method, which leads to the formation of finer microstructure and particles than those produced by conventional manufacturing methods. The microhardness of the Inconel 718 samples increased significantly due to the formation of the strengthening phases in

the matrix by the application of the aging treatment. In the case of PHT-5h, the duration of the aging process was not sufficient to complete the formation of the γ″ and γ′ phases, so the microhardness of the alloys was lower when compared to other treatment conditions. Thus, the heat treatment optimization was continued by increasing the aging time to obtain complete precipitation in the matrix. For PHT-8h condition, the microhardness was reached to the peak value at 462 HV (Figure 4.29).

For SHT, PHT-16h, PHT-28h and PHT-34h conditions, the microhardness values were almost the same among the four heat treated conditions for both building directions (~450 HV). SEM analysis showed that as the aging treatment time increased, acicular-shaped δ phase particles formed along the grain boundaries and in the interior of the grains. It is believed that the formation of this phase caused a slight reduction in hardness as it leads to the dissolution of the strengthening γ″ phase.

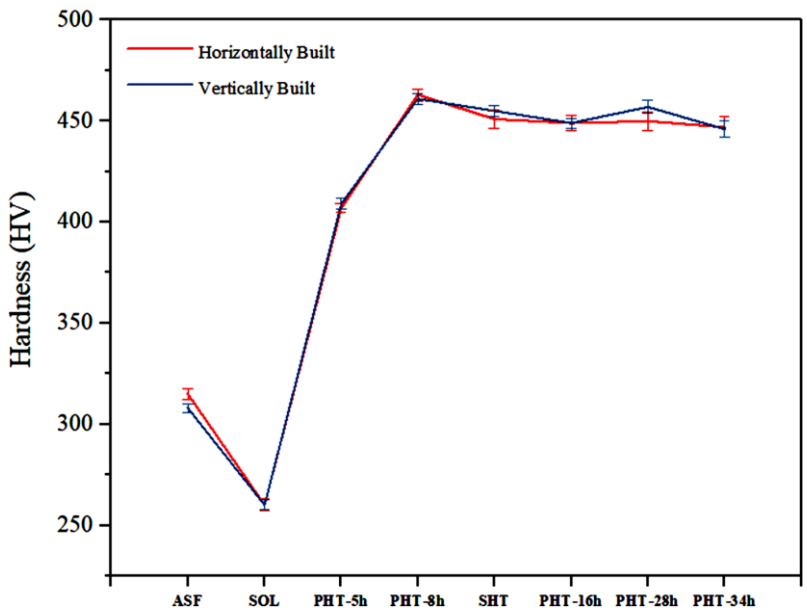

Figure 4.29. Vickers hardness of vertically and horizontally built SLM Inconel 718 samples in both as-fabricated and heat treated conditions.

4.3.2 Tensile Test

The building direction in the SLM process influences the texture formation in the produced component and leads to anisotropic mechanical properties of the materials. Therefore, tensile tests were performed at both room temperature and elevated temperatures (up to 900 ºC) to analyze the mechanical properties of as-fabricated and heat treated Inconel 718 alloys parallel and perpendicular to the building direction. Tensile tests were carried out using an Instron 5582 universal testing machine with a 100 kN load cell at a constant crosshead speed of 0.5 mm/min for both conditions. Firstly, all horizontally and vertically built samples (Figure 3.3) were machined according to ASTM E21 standard (Figure 3.4). For each test, two different samples with a gauge length of 24 mm were utilized in order to attain average values. Prior to the tensile tests, all samples were heat treated according to the PHT-8h condition (i.e. solution treatment at 1040 ºC for 2 h, subsequently aging at 700 ºC for 8 h followed by air cooling); which resulted in the highest hardness value.

Table 4.6 presents the room temperature tensile test results for as-fabricated and heat treated samples in both perpendicular to building direction (axial, HB0) and parallel to building direction (lateral, VB0) including yield strength (YS), ultimate tensile strength (UTS) and the percent elongation (% EL). The AMS specification values of casting (AMS 5383), wrought (AMS 5662) and additively manufactured (EOS-AMS 5662) Inconel 718 alloy are also given as references [32,95]. The stress-strain curves of the as-fabricated and heat treated samples also are shown in Figure 4. 30. The results showed that post-processing heat treatment significantly improved the YS and the UTS values while reducing the % EL at failure for both cases. The mechanical properties of Inconel 718 alloys produced by SLM for both axial and lateral directions were higher than those of the heat treated cast material. Furthermore, the YS (above about 16.6% for the horizontally built sample – 12.2% for the vertically built sample) and the UTS (above about 10.4% for the horizontally built sample – 4.3% for the vertically built sample) values of the PHT-

8h treated samples exceeded that of the wrought Inconel 718 alloy in both directions.

Additionally, % EL of the heat treated samples showed an increase of 63.3% and 97.5% for both lateral and axial directions, respectively, compared to wrought Inconel 718. This may be related to the unique microstructure of Inconel 718 produced by SLM, which was relatively more uniform and finer than those produced by conventional methods because of the higher cooling rate [22]. It is known that for this precipitation hardened alloy, heat treatment promotes the precipitation of finely distributed strengthening γ'' and/or γ' phases in the matrix, which act as barrier to dislocation movement, and thus improve the mechanical properties. Additionally, it promotes the dissolution of the undesirable second particles such as Laves and δ phase which alter the ductility of the Inconel 718 alloy [14,45].

When the mechanical properties of the samples are compared with respect to the building direction, the lateral YS and the UTS values of the horizontally built samples were slightly higher than those of the axial ones of the vertically built samples, whereas the % EL showed the opposite trend. The average relative density of the as-fabricated samples was measured to be ca. 99.8%. No residual porosity has been observed during the microstructural examinations as well. Therefore, the differences between the mechanical properties of the samples cannot be related to the defects caused by the SLM process. This phenomenon can be explained by the formation of textured columnar grains leading to anisotropy in the mechanical properties with respect to the building direction. Moreover, the re-melting of the previously solidified layers causes the formation of some overlapping regions in the microstructure of the samples produced with SLM that provides a strong bonding interaction between the deposited layers. In the vertically built samples, the orientation of overlappings with respect to the loading direction is such that they do not interlock the subsequently built layers making them relatively easier to separate compared to the horizontally built samples.

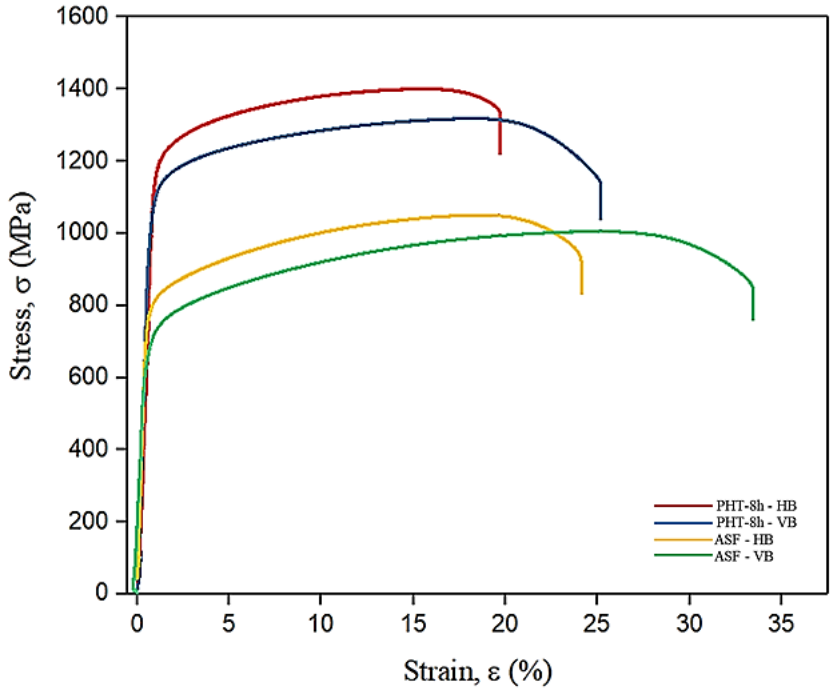

Figure 4.30. Stress-strain curves of the as-fabricated and heat treated samples tested at room temperature.

Table 4.6. A summary of the tensile properties of Inconel 718 alloys measured at room temperature for both building directions.

Condition	Yield Strength (MPa)	Ultimate Tensile Strength (MPa)	Strain at Fracture (%)
ASF-HB	785.22 ± 5.00	1066.50 ± 16.56	27.55 ± 3.38
ASF-VB	702.70 ± 2.72	998.40 ± 6.94	32.22 ± 1.24
PHT-8h – HB0	1206.64 ± 8.26	1408.46 ± 7.32	19.60 ± 0.12
PHT-8h – VB0	1160.30 ± 10.34	1330.42 ± 11.50	23.74 ± 1.42
EOS - AMS5662	1130.00 ± 100.00	1241.00 ± 100.00	15.00 ± 3.00
Cast - AMS5383	758	862	5
Wrought - AMS5662	1034	1276	12

In order to understand the effect of heat treatment on the failure mechanism, fracture surfaces of samples were examined after tensile tests at room temperature. As seen in Figure 4.31, the fracture surfaces of both horizontally and vertically built samples had similar characteristics with a fine dimpled surfaces, indicating the ductile failure mode. Note that the characteristics (i.e. size and depth) of the dimples provide information about the ductility of the material. The results indicated that the depth of the dimples in the fracture surface of the vertically built sample (Figure 4.31 (b)) are higher compared to that of the horizontally built sample pointing out to their higher ductility which was also verified by the mechanical test results (Table 4.6).

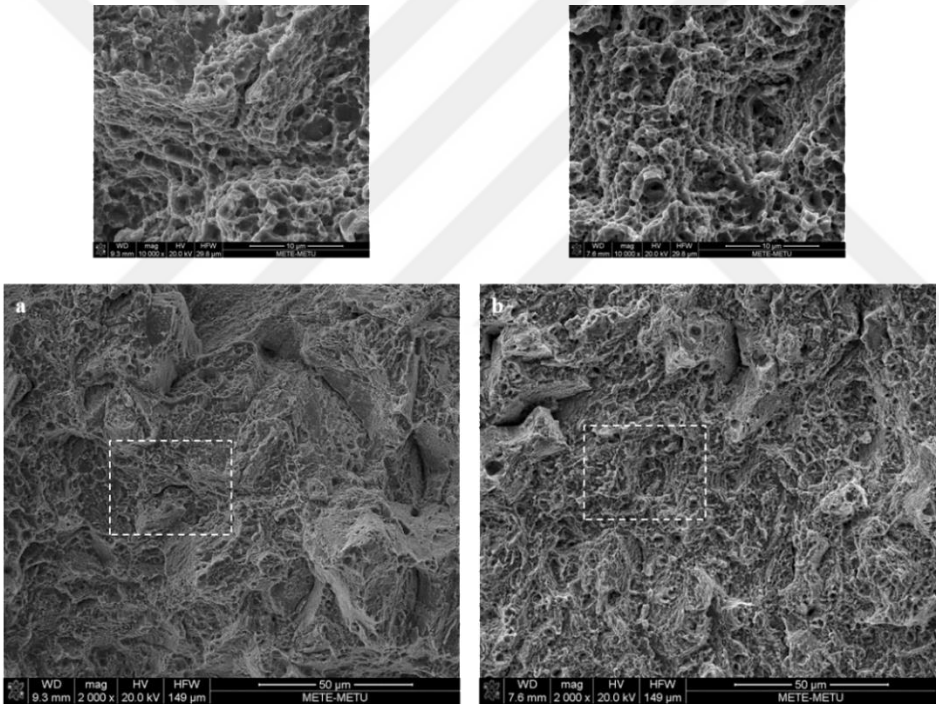

Figure 4.31. Fracture surfaces of the heat treated Inconel 718 alloys tested at room temperature (a) horizontally built sample and (b) vertically built sample.

Figure 4.32 shows the cross sections of the tested samples at room temperature for both horizontal and vertical directions. It is well known that the brittle Laves phase acts as preferred crack initiation and propagation sites along the interdendritic regions. As can be seen, the microvoids (Figure 4.32) are mostly formed around the

Laves phases resulting in premature degradation of the samples. In addition to the Laves phase, some MC type carbides, which were verified to be rich in Nb (59.56 wt.%) by the EDS analysis results, were also detected around the microvoids. A similar result for the Laves phases and MC-type carbides was also found on the fracture surfaces of the Inconel 718 alloy fabricated by direct laser deposition method [58].

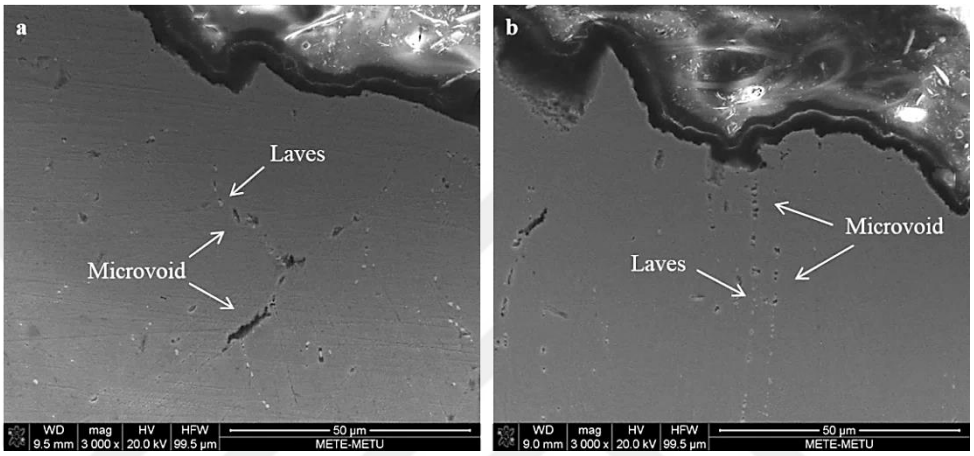

Figure 4.32. Cross sections of the fractured surfaces of the heat treated Inconel 718 alloys tested at room temperature (a) horizontally built sample and (b) vertically built sample.

Figure 4.33 reveals the detailed morphologies of the MC-type carbides in the tested Inconel 718 samples. Some primary MC-type carbides approximately 15 µm in size were detected on the fracture surfaces of the samples for both building directions. These carbides were found to be rich in Ti (80.14 wt.%) as verified by the EDS analysis. It was mentioned that the MC-type carbides have beneficial or negative effects on the mechanical properties of the nickel-based superalloys, which mainly depend on the distribution and morphology of the carbides. It can be observed that primary Ti-rich MC carbides exhibited cleavage characteristics and also acted as preferential sites for easy crack initiation.

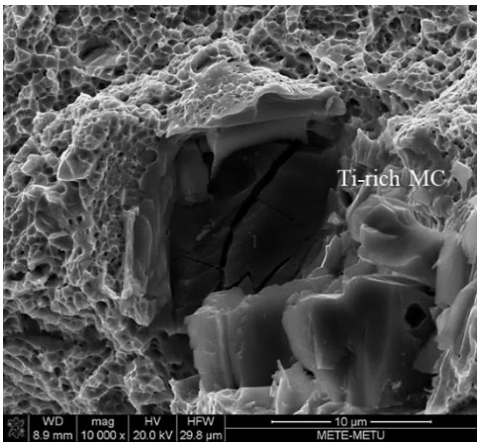

Figure 4.33. Fracture surfaces of the heat treated Inconel 718 alloys tested at room temperature showing fractured primary Ti-rich MC carbide.

Table 4.7 and Figure 4.34 give a summary of the tensile properties of Inconel 718 alloys, which were performed at high temperatures for both building directions. The results showed that the mechanical properties of Inconel 718 alloys produced by SLM for both horizontal and vertical directions tend to decrease as the temperature increases. While the mechanical properties of the horizontally built sample tested at 600 ºC met the standard values for the wrought material, those of the vertically built samples were observed to be slightly below these values. Considering the tensile test conducted at 700 ºC, the results showed that the strength values (YS and UTS) of the samples produced in both directions are still close to the standards. However, the ductility of the horizontally built samples has significantly reduced compared to test results at 600 ºC. As can be seen in Table 4.7, the ductility of the vertically built samples are approximately three times higher than that of the horizontally built samples. In the case of the tensile test conducted at 800 ºC, both YS and UTS values of the samples reduced significantly for both horizontal and vertical directions. Finally, considering the tensile test performed at 900 ºC, both YS and UTS values of the samples decreased dramatically for both building directions. The results showed that the strength of the alloys decreased to about 200 MPa level. In contrast, the ductility of the samples increased by ~33% and ~48% for both horizontal and vertical directions, respectively.

Table 4.7. A summary of the high temperature tensile properties of Inconel 718 alloys for both building directions.

Heat Treatment Condition	Temperature (°C)	Yield Strength (MPa)	Ultimate Tensile Strength (MPa)	Strain at Fracture (%)
HB1	600	1127.90 ± 2.90	1195.80 ± 5.60	18.10 ± 1.30
HB2	700	975.20 ± 2.10	1045.60 ± 8.95	6.40 ± 0.15
HB3	800	618.50 ± 1.50	618.50 ± 1.50	6.20 ± 0.25
HB4	900	210.05 ± 0.85	209.45 ± 0.45	32.6 ± 1.70
VB1	600	975.00 ± 15.00	1107.9 ± 2.05	20.25 ± 0.75
VB2	700	900.90 ± 13.90	976.40 ± 22.40	18.45 ± 0.55
VB3	800	588.50 ± 1.50	600. 25 ± 3.25	17.25 ± 1.25
VB4	900	203.40 ± 7.10	201.65 ± 7.35	47.9 ± 2.90
EOS	650	970.00 ± 50.00	1170.00 ± 50.00	16.00 ± 3.00

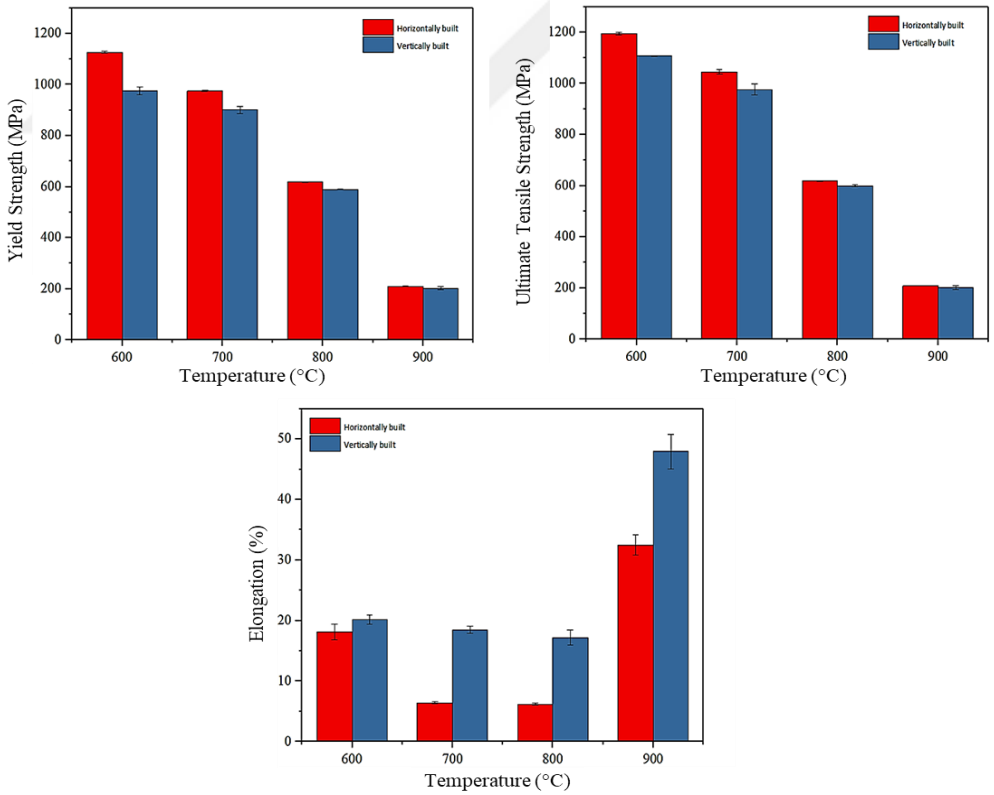

Figure 4.34. High temperature tensile properties of of Inconel 718 alloys for both building directions, (a) yield strength, (b) ultimate tensile strength and (c) elongation at failure.

The fracture surfaces of both samples tested at 600 ºC, possessed fine dimples as shown in Figure 4.35. However, the size and the depth of the dimples are smaller compared to those at the fracture surfaces of the samples tested at room temperature. It is clear that the ductility of the vertically built samples tested at 600 ºC was lower than that of the samples tested at room temperature. Figure 4.36 reveals that Laves phases and MC-type carbides still serve as nucleation sites for the formation of microvoids as in the case of results obtained from the room temperature tensile tests.

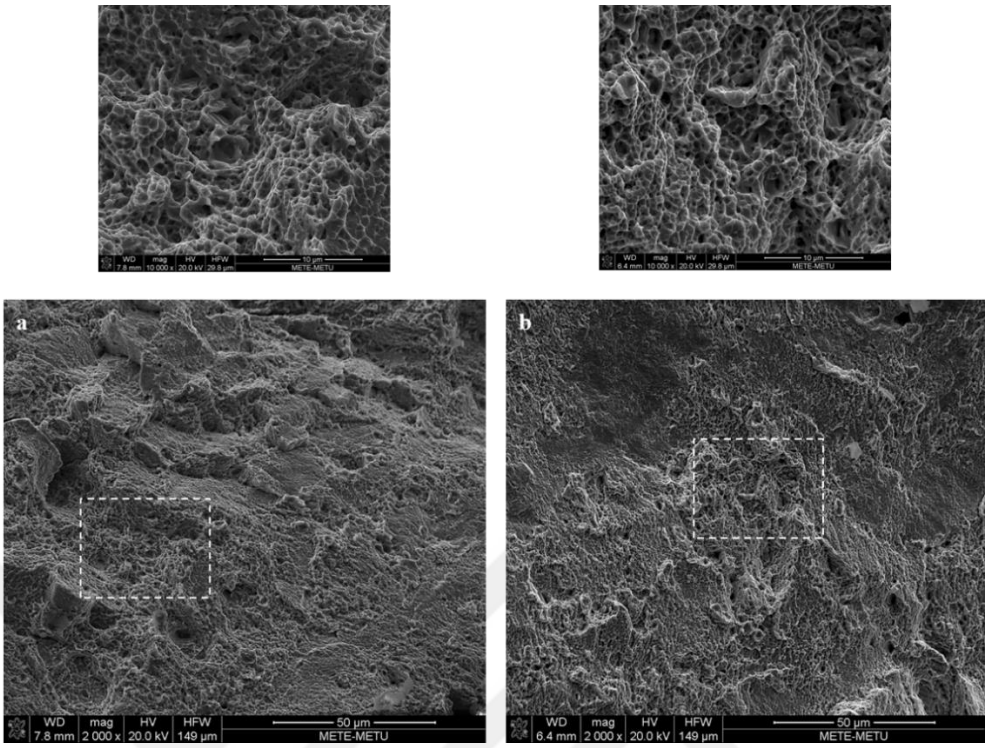

Figure 4.35. Fracture surfaces of the heat treated Inconel 718 alloys tested at 600 ºC (a) horizontally built sample and (b) vertically built sample.

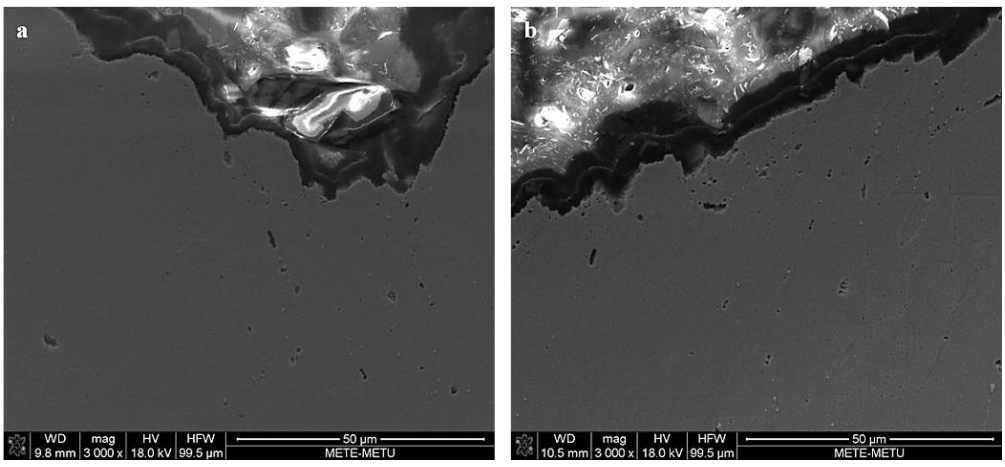

Figure 4.36. Fractured cross sections of the heat treated Inconel 718 alloys tested at 600 ºC (a) horizontally built sample and (b) vertically built sample.

Figure 4.37 and Figure 4.39 illustrate the fracture surfaces of both horizontally and vertically built samples tested at 700 and 800 ºC, respectively. Similar to other tensile test results, dimples are observed for both building directions. However, the amount of the dimples decreases with increasing test temperature, especially in the horizontally built samples. The cross section of the fractured sample surfaces (Figure 4.38 and Figure 4.40) showed that the secondary phases (i.e. Laves phase, δ phase and MC type carbides) caused the formation of cracks when the materials was exposed to the tensile load.

Figure 4.41 illustrates the fracture surfaces of both horizontally and vertically built samples tested at 900 ºC. The results showed that incipient melting has occurred in some Laves phase containing regions which has led to the sliding of the grains during the tensile tests. It is known that incipient melting negatively affects the microstructure as well as the mechanical properties of the Inconel 718 alloy. The studies in the literature showed that the incipient melting of the Laves phase in the matrix may occur when the solution temperature exceeds the eutectic temperature. Miao et al. found that the Laves phase began to melt when the solution treatment was performed at around 1180 ºC [94]. In addition, L. Chang et al. reported that the incipient melting point of the Laves phase in the cast material was between 1150 and 1160 ºC [96].

As can be seen, the high temperature combined with the applied stress caused the melting of the Laves phase at 900 ºC. This can be attributed to the increasing mobility of the solute atoms in the alloy with increasing the test temperature leading to segregation along the grain boundaries, which promotes grain sliding and crack propagation. The cross section of the fractured sample surfaces of the tested samples (Figure 4.42) illustrated that the segregation of alloying elements caused to formation of precipitation free zones (PFZs) around the grain boundaries, as shown by arrows in Figure 4.42) due to Nb depletion by grain boundary precipitation of Laves phase as well as carbides.

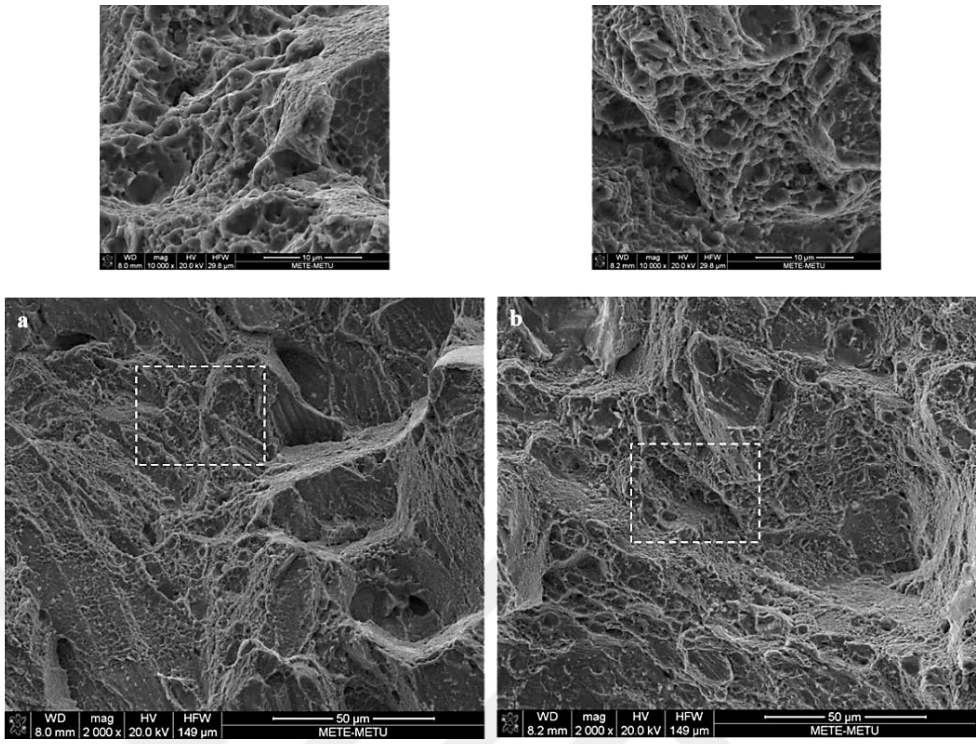

Figure 4.37. Fracture surfaces of the heat treated Inconel 718 alloys tested at 700 ºC (a) horizontally built sample and (b) vertically built sample.

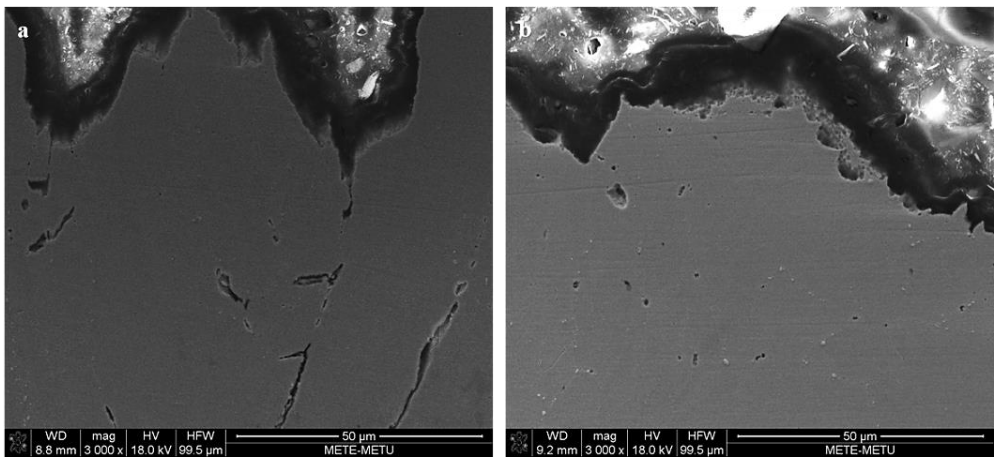

Figure 4.38. Fractured cross sections of the heat treated Inconel 718 alloys tested at 700 ºC (a) horizontally built sample and (b) vertically built sample.

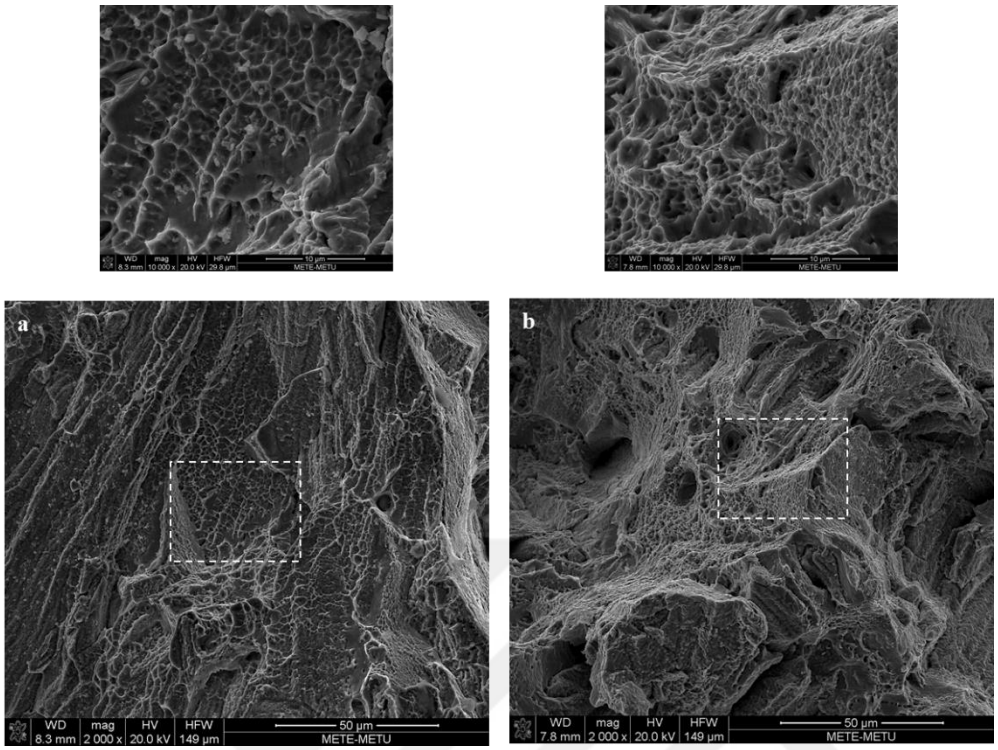

Figure 4.39. Fracture surfaces of the heat treated Inconel 718 alloys tested at 800 ºC (a) horizontally built sample and (b) vertically built sample.

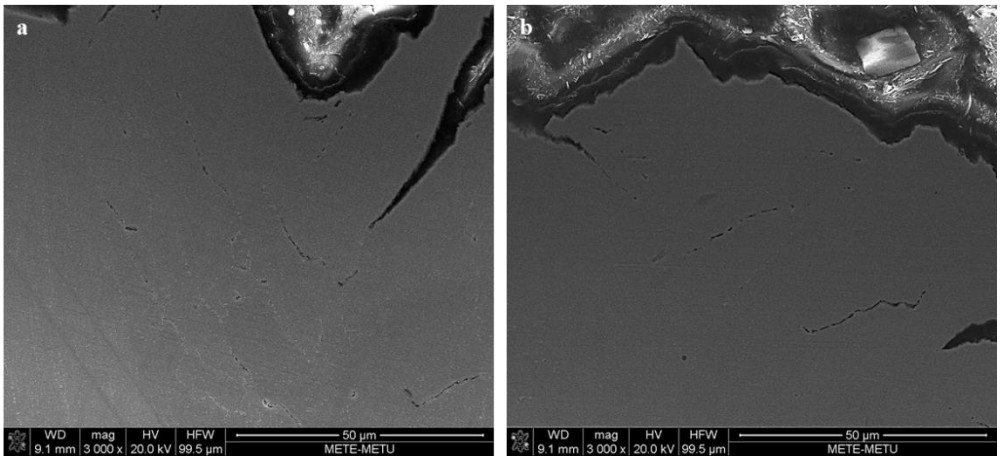

Figure 4.40. Fractured cross sections of the heat treated Inconel 718 alloys tested at 800 ºC (a) horizontally built sample and (b) vertically built sample.

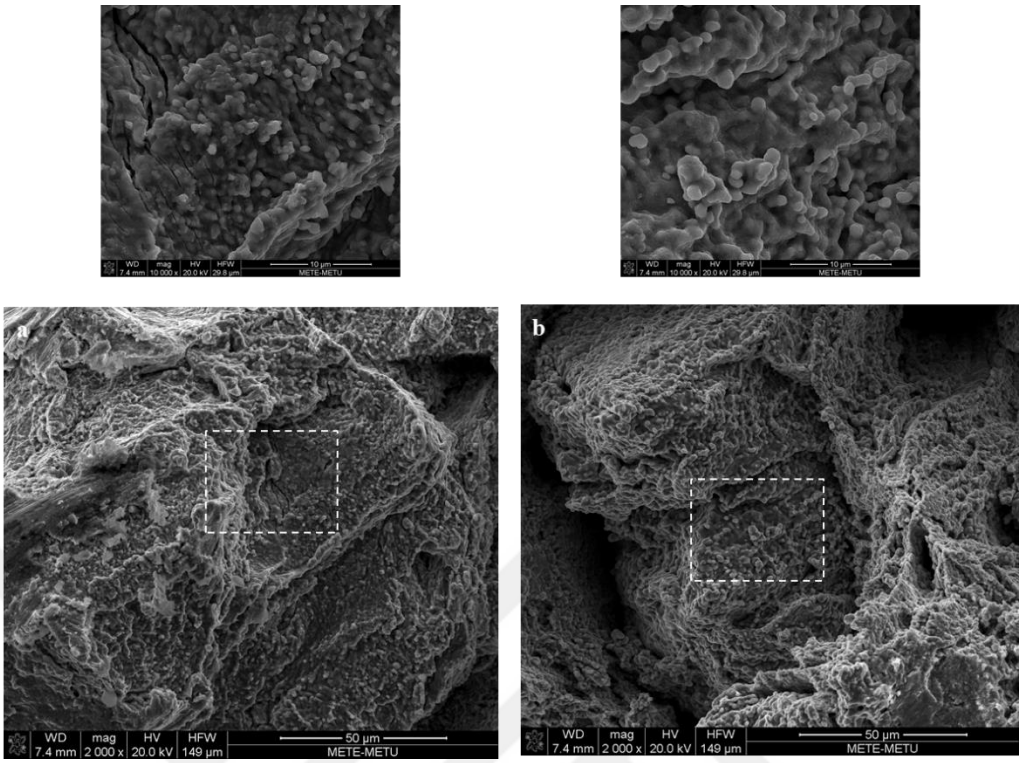

Figure 4.41. Fracture surfaces of the heat treated Inconel 718 alloys tested at 900 ºC (a) horizontally built sample and (b) vertically built sample.

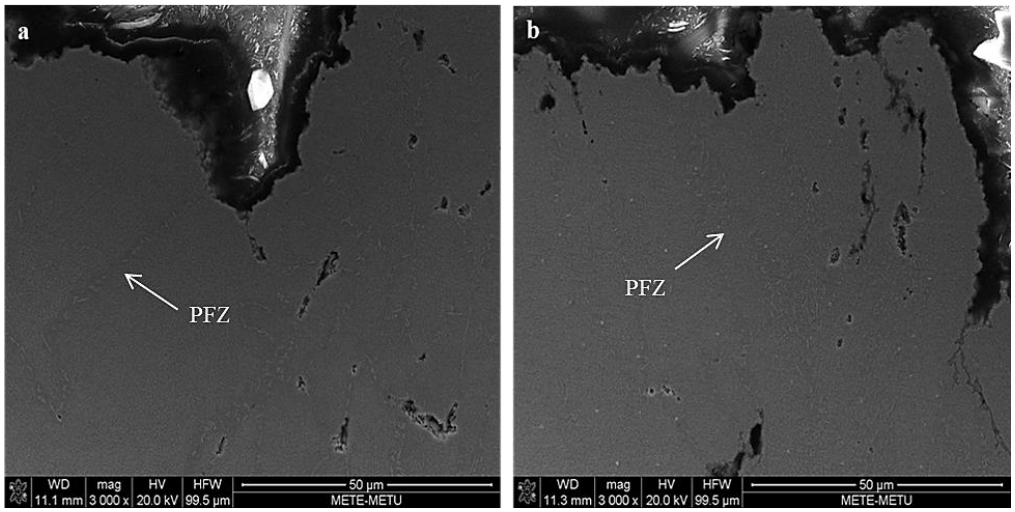

Figure 4.42. Fractured cross sections of the heat treated Inconel 718 alloys tested at 900 ºC (a) horizontally built sample and (b) vertically built sample.

As can be seen in the stress-strain curves obtained at 600 ºC (Figure 4.43), Inconel 718 alloys showed a unique behavior during the high temperature tensile test defined as dynamic strain aging (DSA). It mostly occurs within a certain temperature range, where the mobility of the solute atoms is sufficient to keep up with the moving dislocations during the plastic deformation. This mechanism can be explained by the segregation of the solute atoms around the dislocations forming a solute rich atmosphere causing a decrease in the dislocation velocity. As time progresses, the dislocation density and the number of solute atoms increases in the atmosphere. With increasing dislocation velocity, the dislocations begin to move away from this atmosphere, as the solute atoms can no longer block the accelerating dislocations. Therefore, higher stress is required to prevent the dislocation movements. The pinning and unpinning effect of the solute atoms on the dislocations results in the unstable plastic flow that causes a serration on the stress-strain curves [97,98], which is also observed in the present study as shown in Figure 4.43.

The DSA mechanism is known to be largely dependent on the operating conditions (i.e. temperature and strain rate) along with the composition and microstructure of the alloy, which affects the interactions between the solute atoms and accelerating dislocations. It is associated with the increasing diffusion rate of solute atoms during deformation as the temperature increases. Furthermore, the addition of alloying elements, substitutional or interstitial, causes the formation of secondary phases such as carbides in the matrix. In the current study, the DSA mechanism was observed only in tensile tests performed at 600 ºC. Above this temperature, the mobility of the solute atoms is fast enough to follow the dislocations without impeding their movements [99,100].

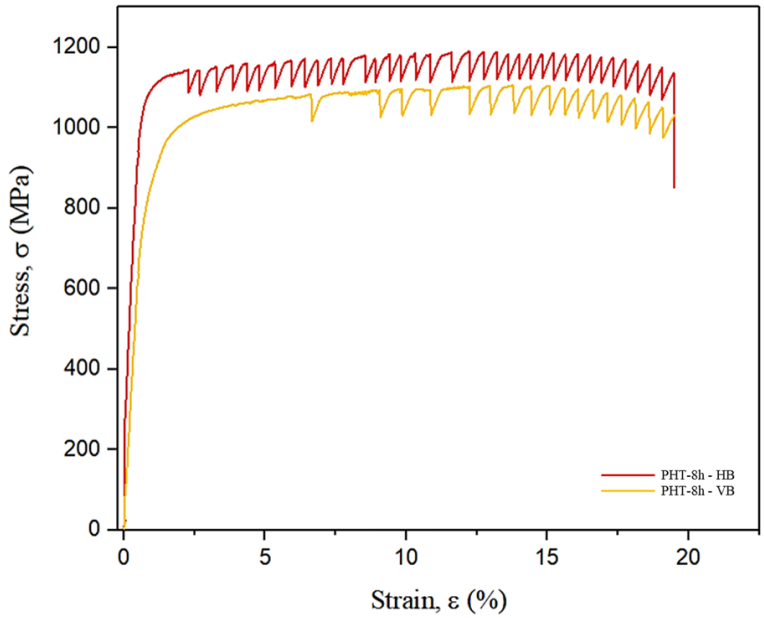

Figure 4.43. Stress-strain curves of the heat treated samples tested at 600 ºC.

As stated in Section 2.2.1, the γ″ phase is metastable and turns into a stable δ phase with acicular morphology, and its formation is greatly influenced by temperature which mostly occurs in the temperature range of 650 to 980 ºC. Moreover, the plate-like δ phase forms in the grains of the Inconel 718 alloy when the temperature approaches to 950 ºC. It is revealed that the mechanical properties of the Inconel 718 alloy are negatively affected by the formation of large amounts of δ phase in the form of plates. The formation of the δ phase consumes the Nb, which inhibits the formation of the γ″ particles [30].

Figure 4.44 reveals detailed morphologies of the phases in the Inconel 718 samples tested at elevated temperatures. The high temperature tensile tests caused formation of δ phase along the grain boundaries and in the grains of the Inconel 718 alloys, Figure 4.44(a) and (b). As can be seen, the amount of the δ phase increases, when the tensile test temperature increased to 800 ºC. In addition, the strengthening γ″ phase was completely converted to the δ phase when the tensile test is carried out at 900 ºC resulting in a dramatic decrease in the mechanical properties (Figure 4.44(c)). The deterioration in the mechanical properties can be explained by the formation of this phase, which leads to a decrease in the amount of the

strengthening γ″ phase in the matrix. Furthermore, this phase acts as nucleation site for crack formation and propagation at elevated temperatures.

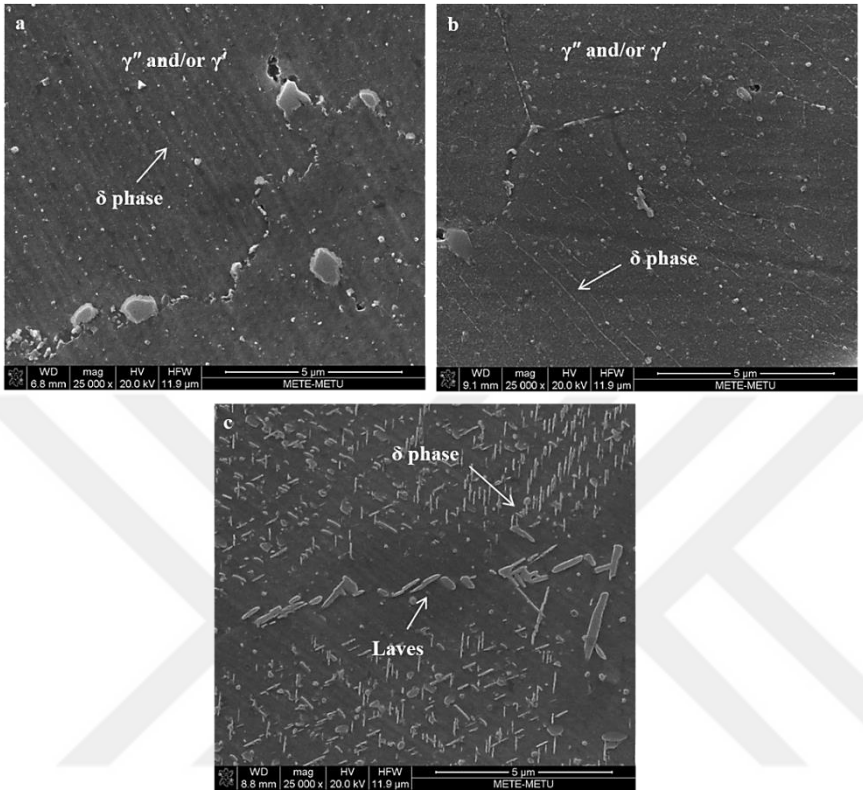

Figure 4.44. SEM images of the heat treated Inconel 718 samples tested at higher temperatures of (a) 700 ºC, (b) 800 ºC and (c) 900 ºC.

CHAPTER 5

CONCLUSIONS

The effect of building direction and post-processing heat treatments on the microstructure and mechanical properties of the Inconel 718 alloys produced by SLM were systematically investigated. Based on the results of this study following conclusions can be drawn.

1- The average relative density of SLM-produced Inconel 718 alloy components is ca. 99.8% of the bulk density, which is accepted in the standard. This can be attributed to the spherical-shaped morphology of the powders used, playing an important role in obtaining fully dense parts during the SLM process.

2- As expected, the microstructures of the Inconel 718 alloys produced by SLM were different from those of cast and wrought materials. Typical melt pool morphology with arc-shaped curves was determined in the lateral observation direction based on the Gaussian energy distribution of the laser beam. Additionally, laser beam scanning paths were seen in the axial observation direction.

3- The melt pool morphology has a very fine cellular/columnar microstructure consisting of irregularly-shaped Laves phases formed in the interdendritic regions. Also, the re-melting of the pre-solidified layers was caused by the formation of some overlapping regions in both observation directions. Besides the brittle Laves phase, Ti-rich carbides were also observed to heterogeneously distribute throughout the alloy matrix during the SLM process.

4- After all heat treatment conditions applied, the arc-shaped microstructural feature disappeared and converted into a mixture of columnar and equiaxed grains. The microstructure of the heat treated alloys consisted of a stable γ matrix

strengthened by coherent particles of the γ″ or γ′ phases and other secondary phases. Due to the low solubility of the large Nb and Mo atoms in the matrix relatively large amounts of undissolved Laves phases were also observed.

5- The results showed that nano-sized γ″ and/or γ′ precipitates were homogeneously dispersed in the matrix, except for the case of PHT-5h condition. The aging heat treatment at 700 ºC for 5 hours was not sufficient to completely precipitate the strengthening phases. It has been found that increase in the soaking time during aging heat treatment leads to an increase in the average size of the precipitates, as expected.

6- The results revealed that the disc-like γ″ phase partially dissolved in the matrix and led the formation of acicular-shaped δ phase along the grain boundaries of the alloys treated by SHT and PHT-16h conditions. Some plate-like δ phase was detected in the matrix treated by PHT-28h and PHT-34h conditions.

7- Three main peaks observed in the XRD results were correlated to the FCC-γ matrix along with the strengthening γ″ and γ′ phases for both as-fabricated and all heat treated samples. All heat treated samples showed a dominant texture in the (200) direction similar to the as-fabricated samples, except for the one treated with PHT-34h condition illustrating a strong texture in the (111) direction.

8- According to EBSD maps and the corresponding pole figures, the horizontally built as-fabricated samples demonstrated columnar grains elongated along the building direction, showing a nearly random orientation with a tendency to align along to mainly (001) and slightly (101) and (111) planes. On the other hand, the texture of the vertically built samples showed equiaxed grains of strong (001) texture. The results revealed that the post-processing heat treatments did not significantly change the texture of the samples for both building directions. Only minor differences related to the holding time of the aging treatment were examined.

9- After all heat treatment conditions applied, the average microhardness of the Inconel 718 alloy was significantly increased due to the formation of the strengthening γ″ and γ′ phases in the matrix, which serve as a barrier to dislocation movement. The microhardness was reached to the peak value of ~462 HV by the PHT-8h condition. A slight decrease in hardness was observed in heat treatments applied for more than 8 hours.

10- Tensile test results performed at room temperature revealed that post-processing heat treatment significantly increased the YS and UTS values and reduced the elongation at failure for both building directions. Fracture surfaces of the tested samples showed that the Laves phase and MC type carbides act as preferred crack initiation and propagation sites along the interdendritic regions. The results showed that both the YS and UTS of the Inconel 718 alloy decreased when the tensile test was performed at high temperatures mainly because of the dissolution of the strengthening γ″ precipitates and the formation of the δ phase in the matrix.

REFERENCES

[1] S. Ahmed. (1990). The design and fabrication of nickel-base superalloys. Jom, 42(8), 24–26.

[2] E. Bullock. (1989). Research and Development of High Temperature Materials for Industry. Springer Netherlands.

[3] S. Singh. (2016). Superalloys Report. 1-40.

[4] J. A. Lee. (2012). Hydrogen embrittlement of nickel, cobalt and iron-based superalloys. Gaseous Hydrog. Embrittlement Mater. Energy Technol. Probl, 624–667.

[5] B. Geddes, H. Leon, and X. Huang. (2010). Superalloys: Alloying and Performance. ASM International.

[6] R. C. Reed. (2006). The Superalloys. Cambridge University Press, London.

[7] J. R. Davis. (1997). ASM Specialty Handbook: Heat-Resistant Materials. ASM International.

[8] A. K. Jena and M. C. Chaturvedi. (1984). The role of alloying elements in the design of nickel-base superalloys. Journal of Materials Science, 19(10), 3121-3139.

[9] J. B. Wahl and K. Harris. (2011). Advanced Ni base superalloys for small gas turbines. Canadian Metallurgical Quarterly, 50(3), 207-214.

[10] E. A. Basuki, D. H. Prajitno, and F. Muhammad. (2017). Alloys developed for high temperature applications. AIP Conference Proceedings, 1805.

[11] Y. Tamarin. (2002). Protective Coatings for Turbine Blades. ASM International.

[12] A. P. Mouritz. (2012). Introduction to aerospace materials. Woodhead.

[13] E. Akca and A. Gürsel. (2015). A review on superalloys and IN718 nickel-based INCONEL superalloy. Periodicals of Engineering and Natural Sciences, 3(1).

[14] J. R. Davis. (2001). ASM specialty handbook: nickel, cobalt, and their alloys. ASM International.

[15] S. Bose. (2007). High Temperature Coatings. Butterworth-Heinemann.

[16] E. M. Lehockey, G. Palumbo, and P. Lin. (1998). Improving the Weldability and Service Performance of Nickel and Iron-Based Superalloys by Grain Boundary Engineering. Metallurgical and Materials Transactions A, 29(12), 3069-3079.

[17] B. M. B. Grant, E. M. Francis, J. Quinta Da Fonseca, M. R. Daymond, and M. Preuss. (2012). Deformation behaviour of an advanced nickel-based superalloy studied by neutron diffraction and electron microscopy. Acta Materialia, 60(19), 6829–6841.

[18] M. Bambach, I. Sizova, F. Silze, and M. Schnick. (2018). Hot workability and microstructure evolution of the nickel-based superalloy Inconel 718 produced by laser metal deposition. Journal of Alloys and Compounds, 740, 278-287.

[19] H. Zhang, C. Li, Q. Guo, Z. Ma, H. Li, and Y. Liu. (2019). Improving creep resistance of nickel-based superalloy Inconel 718 by tailoring gamma double prime variants. Scripta Materialia, 164, 66-70.

[20] T. M. Pollock, N. Rene, N. Rene, and N. Rene. (2006). Nickel-Based Superalloys for Advanced Turbine Engines Chemistry, Microstructure, and Properties. Journal of Propulsion and Power, 22(2), 361-374.

[21] P. E. Aba-Perea, T. Pirling, P. J. Withers, J. Kelleher, S. Kabra, and M.

Preuss. (2016). Determination of the high temperature elastic properties and diffraction elastic constants of Ni-base superalloys. Materials & Design, 89, 856-863.

[22] X. Li et al. (2018). Effect of heat treatment on microstructure evolution of Inconel 718 alloy fabricated by selective laser melting. Journal of Alloys and Compounds, 764, 639-649.

[23] G. H. Cao. et.al. (2018). Investigations of γ′ γ″ and δ precipitates in heat-treated Inconel 718 alloy fabricated by selective laser melting. Materials Characterization, 130(2018), 398-406.

[24] J. Lacaze, M. Dehmas, A. Niang, and B. Viguier. (2011). TEM study of high-temperature precipitation of delta phase in inconel 718 alloy. Advances in Materials Science and Engineering, 2011.

[25] R. Lawitzki et al. (2019). Differentiation of γ′- and γ″- precipitates in Inconel 718 by a complementary study with small-angle neutron scattering and analytical microscopy. Acta Materialia, 163, 28-39.

[26] D. H. Smith et al. (2016). Microstructure and mechanical behavior of direct metal laser sintered Inconel alloy 718. Materials Characterization, 113, 1-9.

[27] G. A. Rao, M. Srinivas, and D. S. Sarma. (2006). Influence of modified processing on structure and properties of hot isostatically pressed superalloy Inconel 718. Materials Science and Engineering: A, 418(1-2), 282-291.

[28] C. M. Kuo, Y. T. Yang, H. Y. Bor, C. N. Wei, and C. C. Tai. (2009). Aging effects on the microstructure and creep behavior of Inconel 718 superalloy. Materials Science and Engineering: A, 510-511, 289-294.

[29] H. Qin, Z. Bi, H. Yu, G. Feng, J. Du, and J. Zhang. (2018). Influence of stress on γ″ precipitation behavior in Inconel 718 during aging. Journal of Alloys and Compounds, 740, 997-1006.

[30] J. Li et al. (2019). Microstructural evolution and mechanical properties of IN718 alloy fabricated by selective laser melting following different heat treatments. Journal of Alloys and Compounds, 772, 861-870.

[31] M. Anderson, A. L. Thielin, F. Bridier, P. Bocher, and J. Savoie (2017). δ phase precipitation in Inconel 718 and associated mechanical properties," Materials Science and Engineering: A, 679, 48-55.

[32] D. Zhang, W. Niu, X. Cao, and Z. Liu. (2015). Effect of standard heat treatment on the microstructure and mechanical properties of selective laser melting manufactured Inconel 718 superalloy. Materials Science and Engineering: A, 644, 32-40.

[33] S. S. Handa. (2014). Precipitation of Carbides in a Ni-based Superalloy, University West, Sweden.

[34] A. Szczotok and K. Rodak. (2012). Microstructural studies of carbides in MAR-M247 nickel-based superalloy. IOP Conference Series: Materials Science and Engineering, 35(1).

[35] X. Z. Qin, J. T. Guo, C. Yuan, J. S. Hou, and H. Q. Ye. (2008). Precipitation and thermal instability of M23C6 carbide in cast Ni-base superalloy K452. Materials Letters, 62(2), 258-261.

[36] H. E. Collins. (2012). Relative Stability of Carbide and Intermetallic Phases in Nickel-Base Superalloys. Thompson Ramo Wooldridge Inc., Cleveland.

[37] R. Jiang, A. Mostafaei, J. Pauza, C. Kantzos, and A. D. Rollett. (2019). Varied heat treatments and properties of laser powder bed printed Inconel 718. Materials Science and Engineering: A, 755, 170-180.

[38] R. Jiang, A. Mostafaei, J. Pauza, C. Kantzos, and A. D. Rollett. (2019). Varied heat treatments and properties of laser powder bed printed Inconel 718. Materials Science and Engineering: A, 755, 170-180.

[39] X. Z. Qin, J. T. Guo, C. Yuan, J. S. Hou, and H. Q. Ye. (2008). Precipitation and thermal instability of M23C6 carbide in cast Ni-base superalloy K452. Materials Letters, 62(2), 258-261.

[40] H. Kitaguchi. (2012). Microstructure-Property Relationship in Advanced Ni-Based Superalloys. Advances in Materials and Processes.

[41] S. Sui et al. (2019). Microstructures and stress rupture properties of pulse laser repaired Inconel 718 superalloy after different heat treatments. Journal of Alloys and Compounds, 770, 125-135.

[42] Callister, W. D., Rethwisch, D. G. (2019). Fundamentals of materials science and engineering: an integrated approach. Hoboken, NJ: John Wiley & Sons, Inc.

[43] E. M. Francis et al. (2014). High-temperature deformation mechanisms in a polycrystalline nickel-base superalloy studied by neutron diffraction and electron microscopy. Acta Materialia, 74, 18-29.

[44] J. P. Choi et al. (2017). Densification and microstructural investigation of Inconel 718 parts fabricated by selective laser melting. Powder Technology, 310, 60-66.

[45] D. Deng, R. L. Peng, H. Brodin, and J. Moverare. (2018). Microstructure and mechanical properties of Inconel 718 produced by selective laser melting: Sample orientation dependence and effects of post heat treatments," Materials Science and Engineering: A, 713, 294-306.

[46] X.Y. XU et al. (2019). Characterization of residual stresses and microstructural features in an Inconel 718 forged compressor disc. Transactions of Nonferrous Metals Society of China, 29(3), 569-578.

[47] W. Huang, J. Yang, H. Yang, G. Jing, Z. Wang, and X. Zeng. (2019). Heat treatment of Inconel 718 produced by selective laser melting: Microstructure and

mechanical properties. Materials Science and Engineering: A, 750, 98-107.

[48] X. You et al. (2017). Effect of solution heat treatment on the precipitation behavior and strengthening mechanisms of electron beam smelted Inconel 718 superalloy. Materials Science and Engineering: A, 689(2), 257-268.

[49] L. Y. Wang, Z. J. Zhou, C. P. Li, G. F. Chen, and G. P. Zhang. (2019). Comparative investigation of small punch creep resistance of Inconel 718 fabricated by selective laser melting. Materials Science and Engineering: A, 745, 31-38.

[50] W. dong Song, M. lei Hu, H. sheng Zhang, and Y. xi Jin. (2018). Effects of different heat treatments on the dynamic shear response and shear localization in Inconel 718 alloy. Materials Science and Engineering: A, 725, 76-87.

[51] A. Thomas, M. El-Wahabi, J. M. Cabrera, and J. M. Prado. (2006). High temperature deformation of Inconel 718," Journal of Materials Processing Technology, 177(1-3), 469-472.

[52] S. Holland, X. Wang, J. Chen, W. Cai, F. Yan, and L. Li. (2019). Multiscale characterization of microstructures and mechanical properties of Inconel 718 fabricated by selective laser melting. Journal of Alloys and Compounds, 784, 182-194.

[53] W. M. Tucho, P. Cuvillier, A. Sjolyst-Kverneland, and V. Hansen. (2017). Microstructure and hardness studies of Inconel 718 manufactured by selective laser melting before and after solution heat treatment. Materials Science and Engineering: A, 689, 220-232.

[54] K. Kulawik, P. A. Buffat, A. Kruk, A. M. Wusatowska-Sarnek, and A. Czyrska-Filemonowicz. (2015). Imaging and characterization of γ′ and γ″ nanoparticles in Inconel 718 by EDX elemental mapping and FIB-SEM tomography. Materials Characterization, 100, 74-80.

[55] S. Yan, Q. Wang, X. Chen, C. Zhang, and G. Cui. (2019). Fabrication of highly compact Inconel 718 alloy by spark plasma sintering and solution treatment followed by aging. Vacuum, 163, 194-203.

[56] D. Deng. (2018). Additively Manufactured Inconel 718 : Microstructures and Mechanical Properties, Linköping University.

[57] M. Komarasamy, S. Shukla, S. Williams, K. Kandasamy, S. Kelly, and R. S. Mishra. (2019). Microstructure, fatigue, and impact toughness properties of additively manufactured nickel alloy 718. Additive Manufacturing, 28, 661-675.

[58] Y. N. Zhang, X. Cao, P. Wanjara, and M. Medraj. (2014). Tensile properties of laser additive manufactured Inconel 718 using filler wire. Journal of Materials Research, 29(17), 2006-2020.

[59] A. Mostafa, I. P. Rubio, V. Brailovski, M. Jahazi, and M. Medraj. (2017). Structure, texture and phases in 3D printed IN718 alloy subjected to homogenization and HIP treatments. Metals, 7(6), 1-23.

[60] Y. Zhang, W. Jarosinski, Y. Jung, and J. Zhang. (2018). Additive manufacturing processes and equipment. Materials, Processes, Quantifications and Applications, 39-51.

[61] I. Gibson, D. W. Rosen, and B. Stucker. (2010). Additive manufacturing technologies: Rapid prototyping to direct digital manufacturing. Springer.

[62] EPMA. (2013). Introduction to Additive Manufacturing Technology.

[63] M. Attaran. (2017). Additive Manufacturing: The Most Promising Technology to Alter the Supply Chain and Logistics. Journal of Service Science and Management, 10(3), 189-206.

[64] S. Liu and Y. C. Shin. (2019). Additive manufacturing of Ti6Al4V alloy: A review. Materials & Design, 164, 107552.

[65] Y. J. Kang, S. Yang, Y. K. Kim, B. AlMangour, and K. A. Lee. (2019). Effect of post-treatment on the microstructure and high-temperature oxidation behavior of additively manufactured Inconel 718 alloy. Corrosion Science, 108082.

[66] D. Tomus, Y. Tian, P. A. Rometsch, M. Heilmaier, and X. Wu. (2016). Influence of post heat treatments on anisotropy of mechanical behavior and microstructure of Hastelloy-X parts produced by selective laser melting. Materials Science and Engineering: A, 667, 42-53.

[67] L. Hitzler et al. (2018). Additive manufacturing of cobalt-based dental alloys: Analysis of microstructure and physicomechanical properties. Advances in Materials Science and Engineering, 2018.

[68] C. Qiu, N. J. E. Adkins, and M. M. Attallah. (2013). Microstructure and tensile properties of selectively laser-melted and of HIPed laser-melted Ti-6Al-4V. Materials Science and Engineering: A, 78, 230-239.

[69] X. Yu and L. Wang. (2018). T6 heat-treated AlSi10Mg alloys additive-manufactured by selective laser melting," Procedia Manufacturing, 15, 1701-1707.

[70] S. Singh, S. Ramakrishna, and R. Singh. (2017). Material issues in additive manufacturing: A review. Journal of Manufacturing Processes, 25, 185-200.

[71] M. L. Griffith et al. (1996). Free Form Fabrication of Metallic Components Using Laser Engineered Net Shaping (LENS). Sandia National Laboratories.

[72] M. Zenou and L. Grainger. (2018). Additive manufacturing of metallic materials. Materials, Processes, Quantifications and Applications, 53-103.

[73] M. Namatollahi, A. Jahadakbar, M. J. Mahtabi, and M. Elahinia. (2019). Additive manufacturing (AM), Elsevier.

[74] N. Shamsaei, A. Yadollahi, L. Bian, and S. M. Thompson. (2015). An overview of Direct Laser Deposition for additive manufacturing; Part II:

Mechanical behavior, process parameter optimization and control. Additive Manufacturing.

[75] Z. Wang, K. Guan, M. Gao, X. Li, X. Chen, and X. Zeng. (2012). The microstructure and mechanical properties of deposited-IN718 by selective laser melting. Journal of Alloys and Compounds, 513, 518-523.

[76] Campanelli L.S. et al. (2010). Capabilities and Performances of the Selective Laser Melting Process. Intech.

[77] P. K. Gokuldoss, S. Kolla, and J. Eckert. (2017). Additive Manufacturing Processes: Selective Laser Melting , Electron Beam Melting and Binder. Materials, 10(6).

[78] M. B. Bezuidenhout, D. M. Dimitrov, A. D. Van Staden, G. A. Oosthuizen, and L. M. T. Dicks. (2015). Titanium-based hip stems with drug delivery functionality through additive manufacturing. BioMed Research International, 2015.

[79] S. Raghavan et al. (2017). Effect of different heat treatments on the microstructure and mechanical properties in selective laser melted INCONEL 718 alloy. Materials and Manufacturing Processes, 32(14), 1588-1595.

[80] E. Chlebus, K. Gruber, B. Kuźnicka, J. Kurzac, and T. Kurzynowski. (2015). Effect of heat treatment on the microstructure and mechanical properties of Inconel 718 processed by selective laser melting. Materials Science and Engineering: A, 639, 647-655.

[81] V. A. Popovich, E. V. Borisov, A. A. Popovich, V. S. Sufiiarov, D. V. Masaylo, and L. Alzina. (2017). Impact of heat treatment on mechanical behaviour of Inconel 718 processed with tailored microstructure by selective laser melting. Materials & Design, 131, 12-22.

[82] M. Larsson, T. Manager, U. Lindhe, and O. Harrysson. Rapid

Manufacturing with Electron Beam Melting (EBM)-A manufacturing revolution. Carolina State University, 433-438.

[83] X. Huang, M. C. Chaturvedi, and N. L. Richards. (1996). Effect of homogenization heat treatment on the microstructure and heat-affected zone microfissuring in welded cast alloy 718. Metallurgical and Materials Transactions A, 27(3), 785-790.

[84] M. Ni, S. Liu, C. Chen, R. Li, X. Zhang, and K. Zhou. (2019). Effect of heat treatment on the microstructural evolution of a precipitation-hardened superalloy produced by selective laser melting. Materials Science & Engineering: A, 748, 275-285.

[85] A. Chamanfar, L. Sarrat, M. Jahazi, M. Asadi, A. Weck, and A. K. Koul. (2013). Microstructural characteristics of forged and heat treated Inconel-718 disks. Materials & Design, 52, 791-800.

[86] C. Kantzos, J. Pauza, R. Cunningham, S. P. Narra, J. Beuth, and A. Rollett. (2019). An Investigation of Process Parameter Modifications on Additively Manufactured Inconel 718 Parts. Journal of Materials Engineering and Performance, 28(2), 620-626.

[87] E21-17e1. (2004). Standard Test Methods for Elevated Temperature Tension Tests of Metallic Materials. ASTM B. Standard.

[88] K. N. Amato, S. M. Gaytan, L. E. Murr, E. Martinez, and P. W. Shindo. (2012). Microstructures and mechanical behavior of Inconel 718 fabricated by selective laser melting. Acta Materialia, 60(5), 2229-2239.

[89] G. Bi, C. N. Sun, H. chi Chen, F. L. Ng, and C. C. K. Ma. (2014). Microstructure and tensile properties of superalloy IN100 fabricated by micro-laser aided additive manufacturing. Materials & Design, 60, 401-408.

[90] D. Zhang, Z. Feng, C. Wang, W. Wang, Z. Liu, and W. Niu. (2018).

Comparison of microstructures and mechanical properties of Inconel 718 alloy processed by selective laser melting and casting. Materials Science & Engineering: A, 724(100), 357-367.

[91] S. Sui, J. Chen, E. Fan, H. Yang, X. Lin, and W. Huang. (2017). The influence of Laves phases on the high-cycle fatigue behavior of laser additive manufactured Inconel 718. Materials Science & Engineering: A, 695, 6-13.

[92] N. Anbarasan et al. (2018). Effect of Heat Treatment on the Microstructure and Mechanical Properties of Inconel 718. Materials Today: Proceedings, 5(2), 7716-7724.

[93] G. E. Bean, T. D. McLouth, D. B. Witkin, S. D. Sitzman, P. M. Adams, and R. J. Zaldivar. (2019). Build Orientation Effects on Texture and Mechanical Properties of Selective Laser Melting Inconel 718. Journal of Materials Engineering and Performance, 28(4), 1942-1949.

[94] Z. J. Miao, A. D. Shan, Y. B. Wu, J. Lu, W. L. Xu, and H. W. Song. (2011). Quantitative analysis of homogenization treatment of INCONEL718 superalloy. Transactions of Nonferrous Metals Society of China, 21(5), 1009-1017.

[95] F. Caiazzo, V. Alfieri, G. Corrado, and P. Argenio. (2017). Mechanical properties of Inconel 718 in additive manufacturing via selective laser melting: An investigation on possible anisotropy of tensile strength. RTSI, IEEE International Forum.

[96] L. Chang, W. Sun, Y. Cui, and R. Yang. (2014). Influences of hot-isostatic-pressing temperature on microstructure, tensile properties and tensile fracture mode of Inconel 718 powder compact. Materials Science & Engineering: A, 599, 186-195.

[97] Cunningham, S. (2001). Effect of substitutional elements on dynamic strain aging in steel. Ottawa: National Library of Canada.

[98] Rao Ch. V. et al. (2019). Dynamic strain aging, deformation and fracture behaviour of the nickel base superalloy Inconel 617. Materials Science & Engineering: A, 742(2019), 44-60.

[99] Yang S., Xue L., Lu W., Ling X. (2020) .Experimental study on the mechanical strength and dynamic strain aging of Inconel 617 using small punch test. Journal of Alloys and Compounds, 815(2020), 152447.

[100] Nagesha A. et al. (2012). Dynamic strain ageing in Inconel® Alloy 783 under tension and low cycle fatigue. Materials Science & Engineering: A, 546(2012), 34-39.